7. Temperature and Heat Flux

Thermochromic liquid crystals (TLCs) can be applied for thermographic measurements of heat transfer and temperature in fluid mechanics, delivering important quantitative full-field data for comparison with and validation of numerical simulations. Thin coatings of TLCs at surfaces are utilized to obtain detailed heat transfer data for steady or transient processes. Application of TLC tracers allows instantaneous measurement of the temperature and velocity fields for two-dimensional cross sections of flows. These methods are based on computerized true-color analysis of digital images for temperature measurements and modified particle image velocimetry, which is used to obtain the flow field velocity. In this Chapter, the advantages and limitations of liquid-crystal thermography are discussed, followed by several examples of thermal flow field measurements.

The use of infrared thermography for nonintrusive measurement of spatially resolved surface heat transfer characteristics is described for five different measurement environments, including situations where large gradients of surface temperature are present. In the first of these, measurements are made on the surface of a therapeutic biomedical patch, where the quantity of interest is the time-varying spatially resolved surface temperature. For the other situations, the measured temperature distributions are used to deduce quantities such as the surface Nusselt numbers on the surface of a swirl chamber, the effectiveness of surface adiabatic film cooling downstream of individual shaped film cooling holes, the surface heat flux reduction ratio downstream of two rows of film cooling holes placed on a model of the leading edge of an airfoil, and thermal boundary condition information for numerical predictions of the heat transfer characteristics on the surface of a passage with an array of rib turbulators. In all of these situations, in situ calibration procedures are employed in which the camera, imaging, and data-acquisition systems are all calibrated together in place within the experimental facility as the infrared measurements are obtained. This requires separate, simultaneous, and independent measurements of surface temperatures, and produces spatially resolved results from infrared images with high levels of accuracy and resolution.

7.1 Thermochromic Liquid Crystals

The description of transient temperature fields is one of the most sought after goals of experimental fluid mechanics. Unfortunately, performing accurate temperature measurements is not an easy task. Point measurements, which are the most common, usually give insufficient information if complex configurations are investigated. Full-field measurements, although not as accurate, may offer greater confidence for comparison with the numerical results. One such full-field technique is based on the use of *thermochromic liquid crystals* (TLCs). Their use to study heat transfer, flow visualization, and thermal mapping is playing an increasing role in the compilation of experimental temperature-related data in several areas of applications, competing with or replacing traditional infrared thermography [7.1].

Liquid crystals are highly anisotropic fluids that exist between the phase boundaries of the solid phase and the conventional, isotropic liquid phase [7.2]. Their temperature sensitivity is based on the property of some cholesteric, chiral-nematic liquid-crystal materials. This phase is typically composed of molecules arranged in a stack of very thin layers with the director in each layer twisted with respect to those above and below. An important characteristic of the cholesteric mesophase is the pitch, which is defined as the distance over which the director rotates a full turn in the helix structure of the nematic layers. The helical structure of the liquid-crystal material is responsible for its ability to selectively reflect light of wavelengths related to the pitch length. As the incident light passes through a TLC material, the periodic variation of the refractive index (Sect. 6.1) modulates the light polarization and causes interference within the multilayered material. According to Bragg's law, a characteristic light wavelength is singled out depending on the light scattering angle, refractive index and structure periodicity. Hence, a single color will be reflected when the molecular pitch is equal to the corresponding wavelength of light in the visible spectrum. Temperature variation or stress executed on the sample will change the director orientation in successive molecular layers, which modifies the pitch length. This makes it possible to use liquid crystals as temperature indicators, where detection of the color change in reflected light leads to quantitative information. The side effect, stress sensitivity of the liquid crystals, is successfully used in fluid mechanics to detect shear or pressure changes [7.3]. However, for temperature measurements this should be minimized to avoid ambiguity of information given by color changes.

Bulk TLC material is normally clear, or slightly milky in appearance. It shows a change of color to red in response to an increase of temperature, followed by yellow, green, blue, violet, finally turning colorless again at higher temperatures. The molecular transition responsible for the selective light reflection is limited to a narrow range of temperature variation, defined for a specific TLC material as the *color play range*. The color changes of TLCs are repeatable and reversible as long as the material is not physically or chemically damaged. This being the case, TLCs can be calibrated accurately with proper care and used as temperature indicators. They modify incident white light and display color with a wavelength that is related to temperature. Beyond its *clearing point temperature*, a TLC material is a transparent liquid, simplifying its use as an additive to paints, filters or warning labels.

Pure liquid-crystal materials are thick, viscous liquids, and are greasy and difficult to deal with under most heat transfer laboratory conditions. TLC materials are also sensitive to mechanical stress. A microencapsulation process that encloses small portions of liquid-crystal material in polymeric material has been introduced to solve problems with stress sensitivity and chemical deterioration.

In the past liquid crystals have been extensively applied in the visualization of entire, either steady-state

or transient temperature fields on solid surfaces. Since quantifying color is a difficult and somewhat ambiguous task, application of TLCs was initially largely qualitative; application of color photography or interference filters for color analysis was tedious and inaccurate. Quantitative and fast temperature measurements were only brought about with the adoption of the charge-coupled device (CCD) color camera and digital image processing. The rapid development of hardware and software image-processing techniques has made the use of inexpensive systems, real-time, transient, full-field temperature measurements using TLCs possible.

Thermochromic liquid crystals can be painted onto a surface [7.4–11] or suspended in the fluid to render the temperature distribution visible [7.12–16]. By disseminating the liquid-crystal material throughout the flow, TLCs not only become classical tracers for flow visualization, but simultaneously, minute thermometers monitoring the local fluid temperature (Fig. 7.1).

The typical diameter of TLC tracers used in flow measurements is 20–50 μm. As the density of TLCs is close to that of water, they are well conveyed in liquid flows. The response time of TLC materials is 3–10 ms, sufficiently fast for typical thermal problems in fluids. Application of TLCs as tracers facilitates instantaneous measurement of temperature and velocity fields [particle image velocimetry (PIV); Sect. 5.3.2] in a two-dimensional cross section of the flow. It is a unique method of combining full-field temperature and velocity measurements [7.17–20]. In the following we give some details on application of TLCs for fluid mechanics measurements, mostly gained through our own experience *playing with colors* during the last 20 years.

7.1.1 Materials

Generally there are three different forms of TLCs available: unsealed pure cholesteric material, slurries of encapsulated TLCs, and mechanically protected thin liquid-crystal films. TLCs can be purchased in one of these forms with the chemical composition matched to the temperature variation of the problem. Typically they have a color play range of about 0.5–40 °C, associated with clearing point temperatures of −30 °C to above 120 °C. The proper choice of material depends on the application. Its working temperature (clearing point) should match the expected temperature range. Selection of narrow-band TLCs offers accurate resolution of temperature but only over a very narrow interval. This is convenient in detecting transient changes of temperature, where the passage of a single, well-defined isotherm through the investigated media can easily be detected. Broadband TLCs give rather qualitative information, discriminating hot and cold regions with very little accuracy of measured temperature values. It is worth noting that most TLC producers define the temperature response of their products using a null angle between illumination and observation. These must be modified according to Bragg's law for other configurations, which results in a shift of the clearing point and shrinkage of the bandwidth of the TLC's color response. Table 7.1 shows the basic properties of a few TLC sam-

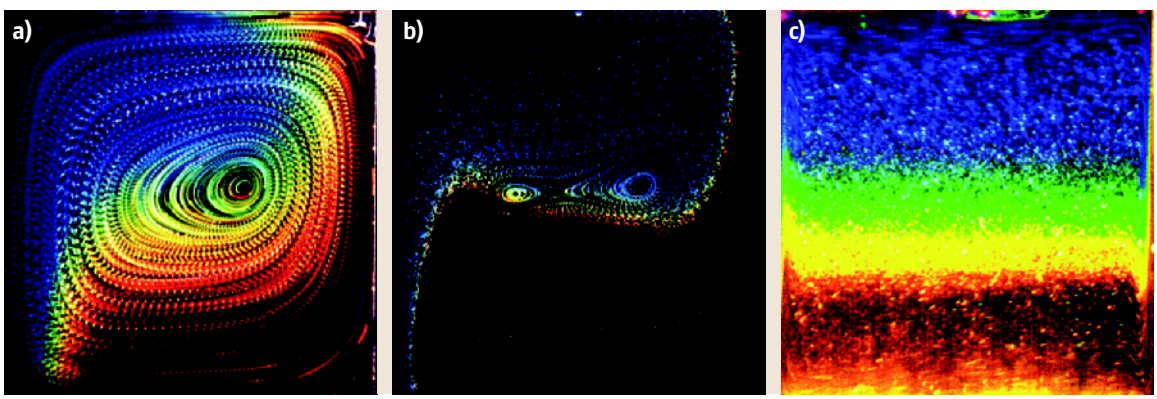

Fig. 7.1a–c Natural convection in a differentially heated box. Three different flow regimes are visualized using unencapsulated liquid-crystal tracers: **(a)** Low Rayleigh number (10^4): temperature difference between walls 4 °C, TLC material TM107, box size 38 mm; **(b)** Intermediate Rayleigh number (8×10^4): temperature difference 16 °C, TLC material TM445, box size 38 mm; **(c)** High Rayleigh number (1.3×10^8): temperature difference 34 °C, TLC material TM317, box size 80 mm. Images **(a)** and **(b)** were obtained from color slides exposed 20 times every 15 s; image **(c)** was created from 20 digital images taken every 200 ms and added in a computer memory

Table 7.1 Thermochromic liquid crystals applied to flow measurements. Nominal red clearing point T_{start} and temperature range ΔT according to catalogue data

Company	Symbol	T_{start} (°C)	ΔT (°C)	Form	Comments
Hallcrest	BM 250/R0C 10W /S33	0	10	Encapsulated	$\Delta T \approx 5$ °C, heavy tracers
Hallcrest	BM 100/R90F 2W /S33	32.5	2	Encapsulated	
Hallcrest	BM 100/R90F10W /S33	32.5	10	Encapsulated	
Hallcrest	BM R29C 4W /S33	29	4	Encapsulated	
Hallcrest	BM 100/R20C10W /S33	20	10	Encapsulated	
Hallcrest	BM 100/R6C12W /S33	6	12	Encapsulated	
Hallcrest	BM 100/R29C4W /S33	29	4	Encapsulated	
Hallcrest	BM /R96C6W	96	6	Liquid	
Hallcrest	BM /R60C6W	59.8	6	Encapsulated	
Hallcrest	BN /R70C6W	69.5	6	Liquid	
BDH	TM 445 (R17 C6W)	17	6	Liquid	Strong colors, $\Delta T \approx 4$ °C
BDH	TM 446 (R37 C6W)	37	6	Liquid	Strong colors, $\Delta T \approx 4$ °C
BDH	TM 317	21	20	Liquid	Strong colors, $\Delta T \approx 4$ °C
BDH	TM 107 (R27 C6W)	27	8	Liquid	Strong colors, $\Delta T \approx 3$ °C
Merck	TM 912	−2	10	Liquid	Strong colors
Merck	TCC 1001 (27C-31C)	27	4	Encapsulated	Very stable suspension

ples used as tracers with some practical remarks about their usage.

Liquid-crystal organic compounds degrade very easily when exposed to chemical contamination and to ultraviolet light. Slight chemical contamination may shift the color play range over several degrees Celsius or even completely remove the TLC temperature sensitivity. In our experience, apparently negligible sources of contamination such as the use of polyvinyl tubes for providing the suspension of liquid crystals appear to produce surprisingly strong effects on the TLC response characteristics. As the effect of chemical deterioration is usually difficult to predict, it is recommended to use unsealed TLCs only in water and its solutions with glycerol. For all other flow configurations protection through encapsulation is necessary. Despite this inconvenience in most of our experiments pure, unsealed TLCs material was used to produce TLC tracers. There are two main reasons for this. Pure material offers a very good signal-to-noise ratio for color evaluation. For large enough tracers and for glycerol or water as a carrier liquid, the intensity of light scattered by unsealed TLCs (Mie scattering band) beyond their clearing point is negligibly small. Hence, tracers are practically invisible for temperatures outside their color play range. This practically cancels any secondary light scattering, improves color evaluation, and allows for deeper optical penetration in the flow. The second reason for using pure TLCs material, which is very important in our experience, is their flexibility in matching the color play range. In experiments where phase changes takes place (freezing, boiling) the color play of TLCs must exactly match the desired temperature range. Usually it is not possible or very expensive to obtain TLCs manufactured exactly to that range, and even then experimental conditions may shift the resulting color response, making new, expensive matching of the ordered TLCs necessary. The same result can be achieved simply in the laboratory using unsealed material by mixing two samples of TLCs with clearing points above and below the desired working temperature. The mixture obtained will exhibit temperature sensitivity in the range proportional to its composition.

Pure TLC material is commercially available as a thick, viscous liquid. It can be dissolved in several organic solvents (e.g., diethylether) and sprayed onto the solid surface or directly into the fluid to be investigated. It is also possible to emulsify them into the liquid by strong mixing with the carrier fluid. When applying unsealed TLCs as tracers, it is important to achieve a homogeneous, very dilute suspension of small droplets. The size of the tracers should be minimized to avoid buoyancy effects and guarantee that tracers follow the flow pattern. However, they should be large enough to be detectable and, what is even more important in the case of TLCs thermography, to guarantee a strong enough signal-to-noise ratio of reflected light for color evaluation.

Several techniques have been investigated to achieve this target. Mixing diethylether solutions of TLCs with a hot carrier liquid is a relatively simple and efficient method. First, a thin layer of the solution is left at the liquid surface until the ether has completely evaporated. Then, by mechanical stirring, a tiny microlayer of pure TLC is broken into a suspension of microdroplets. However, the resulting droplets vary quite substantially in size and an additional selection procedure (sedimentation) is necessary to remove the large ones. The method was improved using piezoceramic droplet generator to disperse the ether TLC solution in a 2 m-high fall tower [7.21]. The ether solvent in droplets with a diameter of 0.4 mm completely evaporates during their flight, and pure TLC material can be collected in the carrier liquid. The apparatus allows a suspension of almost perfectly monodisperse TLC droplets with a diameter of 50 μm to be obtained, evidently improving the quality of tracer images (Fig. 7.1a,b). A less tedious but in most cases satisfactory method of dispersing pure TLC materials in liquids is turbulent mixing of a preheated carrier liquid doped with a small amount of hot TLC material. Using this method, the TLC droplet size is 10–50 μm, forming a uniform colorful mist when observed by a CCD camera.

Perhaps the most common method employed for flow visualization experiments is the application of encapsulated TLCs, which are commercially available as slurries of polymer capsules in water. Each microcapsule, of size 50–150 μm, contains approximately 40% (by weight) of enclosed TLC material. These are custom formulated for the required color change properties. It is possible to control the buoyancy (apparent specific gravity) characteristics of the microcapsules within limits by varying the composition of the TLC mixture, and the microcapsule diameter and wall properties. The TLC slurry can be added directly to the carrier fluid. Theoretically, it should be possible to use such microcapsules in any liquid that is not aggressive to the encapsulation material. Since the slurry carrier is water, in practice it seems that they can only be mixed with aqueous solutions of glycerol, ethylene glycol, and other similar low-molecular-weight polyhydric alcohols. Seeding with dry particles is not possible. Polymeric shells enclosing TLC materials are very fragile. Any attempt to remove the TLC particles from the slurry by drying or filtering leads to their damage and loss of their content. Perhaps the only nonaqueous carrier liquid successfully used with encapsulated TLCs is silicon oil. Usually encapsulated TLCs produce less-saturated colors. Light diffused by the capsule creates an additional white background in addition to the selective reflection by the liquid crystals, decreasing the saturation of the analyzed colors and the overall transparency of the carrier liquid. Therefore the potential advantages of using encapsulated TLCs, the chemical and mechanical protection of the TLC material, is diminished by the reduced flexibility in matching size and composition, their worse optical properties, and the much higher unit price.

For surface temperature measurements, the unencapsulated material (unsealed liquid) is applied to a clear plastic sheet and sealed with a black backing coat to form a prepackaged assembly. Commercially temperature-indicating devices using a thin film of liquid crystal sandwiched between a transparent polyester sheet and a black absorbing background are available. If chemical or mechanical protection is not a serious problem, it is possible to deposit pure material directly onto the black surface. Evaporation of an ether solution of TLCs has been successfully used to cover interrogated surfaces with a very uniform, thin microlayer of thermochromic material.

Application of TLCs sheets and films is limited to measurements of the heat transfer coefficient and temperature distribution over areas that are difficult to access with other complementary techniques such as infrared (IR) thermography. TLC films have an advantage over IR techniques in all configurations where direct monitoring of long-wavelength infrared radiation is obstructed, for example by a water film falling over the surface in question. However, obtaining quantitative measurements with TLC films is not simple and in many cases impossible due to artefacts produced by nonuniform illumination of the interrogated object. Additional sources of uncertainty are heat flux resistance occurring between the surface and the thermochromic foil or unknown variations of the effective thickness of the thermosensitive paints sprayed over the surface.

7.1.2 Illumination

TLCs show colors by selectively reflecting incident white light. The observed color depends on the TLC temperature and also on the reflection angle, measured relative to the incident light direction. The effects are different in thin films and paints compared to tracers suspended in liquids. In both cases two basic rules apply:

1. the light source should have smooth and stable spectral characteristics, and

2. the angle between the observer (camera) and the direction of incident light should be kept fixed across the whole monitored area.

To fulfil the first condition, collimated light from strong halogen lamps or xenon flash tubes is practically the only choice. For flow illumination, strong and relatively easily fabricated light sources are assembled using linear 1000 W halogen lamps with a tungsten filament spanning a 150 mm tube. Lamps are switched on for only a short time (0.5–5 s) to avoid excessive heating and to extend the lifetime of the filaments. A filament preheating circuit is used to speed up switching of the lamp to full power. High-energy xenon discharge lamps are employed for short illumination times. Such lamps consist of a 150 mm-long tube connected to a battery of condensers and can deliver as much as 1 kJ of energy during a 1 ms pulse. Repetition of the light pulses is relatively slow (several seconds). The total thermal load and condenser charging time are both factors limiting the repetition rate. In practice, two sets of condensers with an electronic switch can be used to allow two light pulses to be emitted from the same tube within approximately 200 ms. Such a configuration is useful when applying TLC tracers for simultaneous temperature and velocity measurements (particle image thermometry (PIT) and velocimetry (PIV); for the latter see Sect. 5.3.2).

For surface temperature measurements special care is necessary to avoid specular light reflections form the surface covered by the TLCs. Sometimes polarization filters may help to minimize this effect. Application of diffuse light, often preferred for the illumination of complex surface geometries, introduces uncertainty in the color–temperature relation and limits the accuracy of measurements due to variation of the illumination/observation angle over the investigated area. To avoid additional heating by irradiating light, infrared filters and short light pulses should be applied. Use of fluorescent tubes is not advised as the illumination they produce is pulsating in time and spectrally discontinuous.

Incident light should be collimated to achieve well-defined conditions for Bragg reflection of a single wavelength. This is especially important for tracers, where reflected light is observed directly. For TLCs sealed between multilayered films, internal light reflections partially diminish their sensitivity to the observation angle variation. In some surface temperature studies, variation of the lighting/viewing angle by up to 30° is often accepted as a compromise between illumination uniformity and good color resolution [7.4]. However, for quantitative measurements such a compromise is not acceptable and, as pointed out by *Sabatino* et al. [7.10], only a calibration over the full viewing area can help to remove viewing angle bias from surface temperature measurements. In practice this requires a calibration curve for each point (image pixel) of the analyzed surface. Such a technique, which is easy to perform when using digital recording, takes into account most sources of uncertainty in the perceived hue, including reflections, nonuniformity of the color response characteristics of the CCD pixels, lenses, and optical windows.

Good collimation of panchromatic (white) light, which is necessary for quantitative temperature measurements, is not an easy task. Optical passages including multiple slits, parabolic mirror and cylindrical lenses are used to extract a 2 mm-thick 100 mm-wide sheet of light from a halogen or flash tube, with the sheet collimation preserved over a distance of about 10 cm. The cost of this is strong attenuation of the light intensity, leaving little left from a 1000 W light source. To resolve the difficulties of light collimation it is possible to apply a bundle of three monochromatic light sources, such as lasers or laser diodes operating at blue, green and red colors. However, an additional problem arises with equalizing the color balance at every illuminated point. Hence, in practice lasers (HeNe) are applied for the illumination of TLCs only to extract single isotherms for calibration purposes.

A procedure has been developed to resolve the question of the single-wavelength accuracy of the method and its sensitivity to variations in lighting and viewing angle [7.22]. A suspension of unsealed TLCs (TM317) in glycerol was produced using the aforementioned ether-solvent-based dispersing method. Calibration of the suspension was performed in a small cubic container (38 mm internal size) made of Plexiglas, with top and bottom walls made of black, oxidized metal. Both metal walls were kept at a constant temperatures, 28.7 °C for the top and 26.6 °C for the bottom, ensuring stably stratified thermal field in the liquid. The temperature in the cavity varied linearly with height, with small deviations in the vicinity of the Plexiglas side walls. The liquid was illuminated by a chopped 0.5 mm-diameter laser beam from a 5 mW HeNe laser, passing through the center cross section of the cavity (Fig. 7.2a). The scattered light was observed in the perpendicular direction ($\phi = 90°$) with an optical system equipped with a focusing lens and a photodiode. Scattered light was collected from a region approximately 1 mm in size, selected in the middle

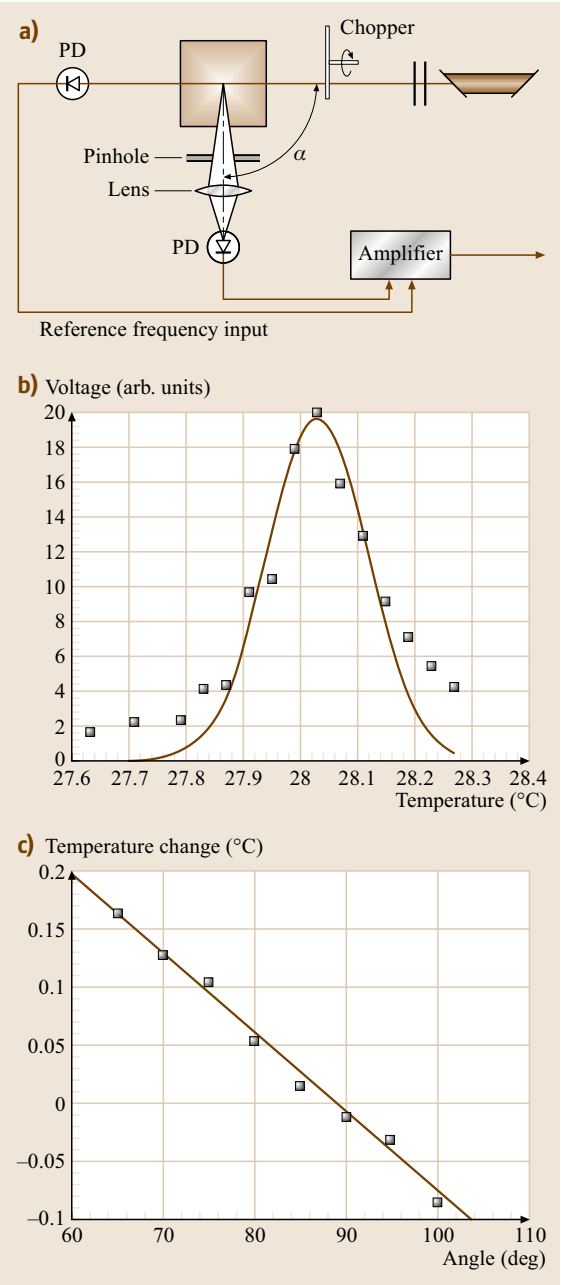

Fig. 7.2a–c Intensity of HeNe laser light scattered by suspension of unencapsulated TLC tracers (TM317) kept in a stable vertical temperature gradient in a 38 mm Plexiglas box: **(a)** schematic of the apparatus, **(b)** effect of temperature variation, **(c)** effect of the angle of observation on the measured temperature shift

of the beam. The scattered light intensity was monitored using a differential, phase-locked voltmeter. Moving the cell up and down with a micrometer screw, liquid layers with linearly varying temperature were interrogated. The intensity of the scattered light (reflected by the TLCs) remained almost constant until the temperature-matched red-band sensitivity of TLCs. A strong peak in the signal was observed (Fig. 7.2b) when the condition for matching the laser wavelength with the TLCs characteristic pitch was reached. The near-Gaussian shape of the signal, with a half-amplitude width corresponding to a 0.2 °C temperature change, indicates the nominal sensitivity of the TLC sample. This value corresponds to the ideal conditions of 633 nm-wavelength evaluation of isotherms, and for the given experimental configuration defines the minimum error of quantitative temperature measurements in the red part of the color play range of the TLC sample. The dependence of the reflecting angle on the temperature shift was evaluated by varying the position of the detector on the arc centered at the interrogated point of liquid. Figure 7.2c illustrates the linear decrease of the detected light intensity, with a slope corresponding to a change of 0.07 °C in the recorded temperature for each 10° change in the viewing angle. This test underlines the importance of preserving a fixed angle between the illuminated plane (light sheet plane) and the camera, and keeping the viewing angle of the lens small. For example, observing a 5 cm-wide area with a CCD camera in the perpendicular direction, the observation distance should be about 400 mm to keep the viewing angle below 4°.

7.1.3 Acquisition and Calibration

The calibration procedure is the most tedious and delicate element of TLCs thermography. Due to the unstable properties of TLCs and the large sensitivity of their color response to experimental conditions, the same illumination and recording system should be used for calibration and measurements. This guarantees that color bias due to external optical effects is taken into account. A typical experimental setup used for quantitative thermography consists of an illumination set, a three-chip CCD color camera and a 24 bit frame grabber. A commercially available standard three-CCD camera can be used, but its color response should be verified and properly balanced. The electronically generated color bars are useful to balance the gain and contrast of each of three color channels. Features that compensate for the nonlinear color response of the human eye, automatic gain, and white

balance, usually set by default in standard cameras, should be deactivated.

For flow measurements, the investigated cavity is illuminated with a thin sheet of white light from the aforementioned halogen lamp or xenon flash tube and observed in the perpendicular direction. The color images, typically of 768×564 pixels, can be easily acquired using a color frame grabber installed in a personal computer equipped with a peripheral component interconnect (PCI) or Firewire (IEEE 1394) interface. The setup (Fig. 7.3) additionally consists of a computer-controlled system of three stepper motors, which allow the automated acquisition of several horizontal and vertical planes across the flow within one or two minutes. Hence, for slowly varying flow structures, a transient recording of three-dimensional flow features is possible. Recording of the transient flow patterns and temperature fields is performed periodically. Typically every 10–300 s, a short series of images is acquired and stored on the hard disk of the computer for later evaluation. In the case of TLC tracers their displacement can be analyzed using the PIV technique (Sect. 5.3.2, and full flow velocity fields are obtained [7.18].

Temperature measurements using TLCs are based on color analysis of the images and needs appropriate calibration. This is eased by using preprocessed color information from a three-CCD camera, which splits light into three basic components: red, green and blue (RGB). This process is known as trichromic decomposition. Each of the three color components is usually recorded as a separate 8 bit intensity image. Numerous methods of subtracting color information from a trichromic RGB signal exist [7.6]. The most straightforward is to convert the RGB trichromic decomposition to another trichromic decomposition based on *hue* (color value), *saturation*, and *intensity* (HSI). Such a decomposition is common in image analysis and also serves as a natural means of converting color images to their black-and-white representation. Classical conversion of an RGB color space to an HSI decomposition is based on three simple relations. Light intensity I (or brightness) is defined as the sum of its three primary components:

$$I = \frac{\sqrt{(R^2+G^2+B^2)}}{\sqrt{3}} \tag{7.1}$$

with R, G and B being the intensities of the red, green and blue components, respectively.

Using an 8 bit representation, the maximum intensity is equal to 255. The saturation S represents color purity, i. e., the relative value of the reminder after subtracting the amount of colorless (white) light:

$$S = 255\left(1 - \frac{\min(R, G, B)}{I}\right) . \tag{7.2}$$

In our representation pure colors have saturation equal to 255. The hue H relates to the dominant color and is usually obtained from the algebraic or trigonometric relation between the two dominant primary colors. To make use of the 8 bit signal dynamics and limiting ourselves to the spectral colors [7.18], the following formula is used to calculate the hue value:

$$H = \begin{cases} 63 + [(G' - R')63]/(G' + R') & \text{for } B' = 0\,, \\ 189 + [(B' - G')63]/(G' + B') & \text{for } R' = 0\,, \end{cases} \tag{7.3}$$

where $R' = R - \min(R, G, B)$, $G' = G - \min(R, G, B)$, and $B' = B - \min(R, G, B)$.

Temperature is determined by relating hue to a temperature calibration function. This is the most critical stage of TLC-based thermography. Light refracted by TLCs is not monochromatic, even if the observed sample has a uniform temperature. Color depends on observation angle, the scattering properties of the TLCs material, the color and refractive index of the carrier liquid, and may also vary with the size of the particles. Additional factors, such as the color of the light source, the color transmission properties of the acquisition system, as well as reflected and ambient light modify the resulting color information. The observed color may also depend on light intensity. Very careful calibration is therefore necessary to obtain quantitative information. It is advised to generate a separate calibration curve for each small area of the investigated surface and use these to normalize the measured color information.

For the best effects the calibration procedure should be performed with an identical experimental arrangement to that used for measurements. To perform the

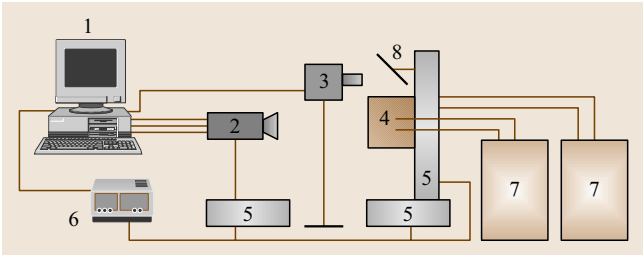

Fig. 7.3 Schematic of the experimental system. PC (1) with the acquisition card controlling the color camera (2), halogen lamp (3) and three stepping motors (5) using a driver (6). The temperature in the cavity (4) is controlled by two thermostats (7); the mirror (8) used to direct the light sheet

calibration, an interrogated surface or liquid in a cavity with a suspension of TLC tracers must be kept at a constant and uniform temperature. Temperature stability and uniformity better than 0.1 °C is required for TLCs with narrow color bands. For measurements of temperature fields in liquids this is achieved by keeping the walls of the experimental cavity at a constant temperature and continuously mixing the liquid with a magnetic stirrer. Data for calibration are obtained by adjusting the liquid temperature in small increments (usually 0.3 °C steps) and acquiring several sequences of images for future processing. Compared to surface thermography, the use of TLCs suspension for flow investigations yields additional problems. The color images of the flow are discrete, i. e., they represent a noncontinuous cloud of points and their color usually varies from point to point. This is not only caused by slight variations in the TLC temperature responses but also indicates local fluctuations in the fluid temperature present due to the limited thermal diffusivity of liquids. To minimize this effect, calibration is usually performed for small areas of about 30×30 pixels, extracted in the vicinity of the temperature sensors from each image and averaged for several subsequent images.

Hue evaluation is performed for each pixel of the resulting averaged image, under constraints of minimum and maximum pixel intensity and minimum saturation. Only good pixels, i. e., those having an intensity and saturation above a given threshold level, are used to build a hue matrix, which is smoothed using a 5×5 median filter followed by a low-pass filter. An average hue value is then calculated for each image and used as a reference point for the calibration procedure. The procedure can be repeated for several parts of the image to create a position-dependent temperature–hue relation. For the full color range of TLCs about 20–30 calibration points are collected at gradually increasing liquid temperatures. A smooth and unique hue–temperature relation is established by fitting a polynomial of degree 6–10. After removing outliers, a final fit is performed to obtain a smooth temperature–hue function (Fig. 7.4). The accuracy of the measured temperature depends on the color (hue) value as a direct consequence of the nonlinearity of the curve. The relative error is 3–10%, and is based on the temperature range defined by the TLC color play limits. It is estimated by calculating the uncertainty

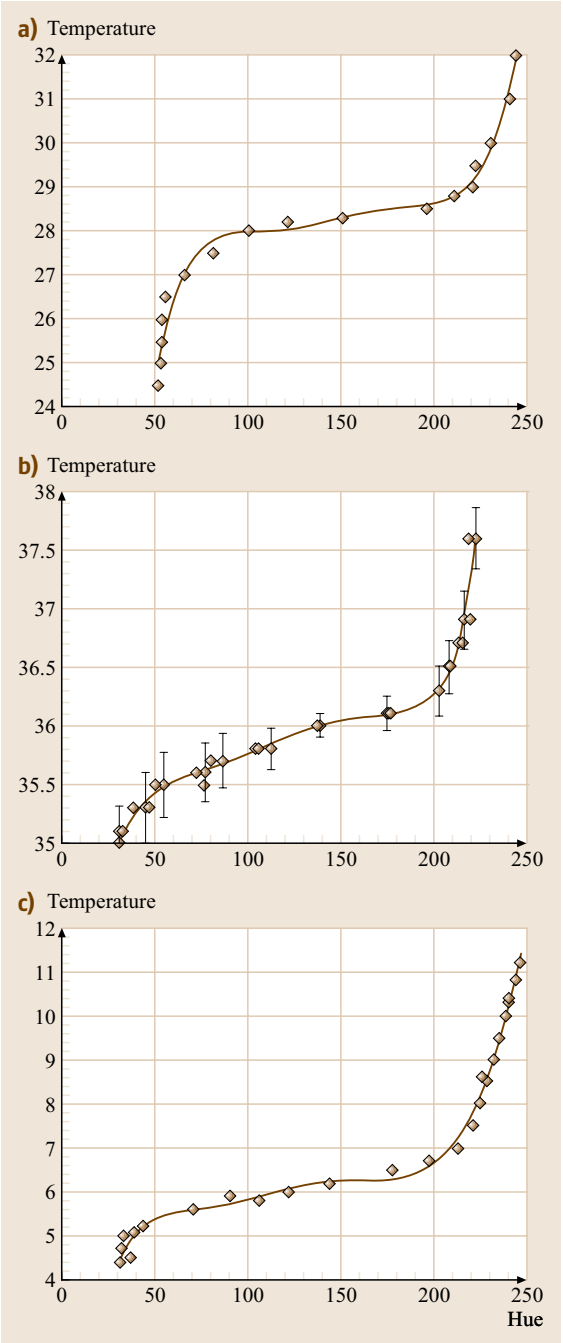

Fig. 7.4a–c Temperature versus hue calibration points and high-order polynomial fits for three different TLCs dispersed as tracers in a flow. **(a)** Encapsulated tracers TCC1001 in water; **(b)** Suspension of unencapsulated TLCs TM446 in water, error bars indicate estimated accuracy; **(c)** Mixture of two TLC types (TM445 and TM912) used to produce a suspension of liquid crystals matching the desired temperature range

of single-point measurements from several images of the same flow. For the TLCs used to obtain the curve in Fig. 7.4b (TM446), an absolute accuracy of 0.15 °C results for low temperatures (red–green color range) and 0.5 °C for high temperatures (blue color range). The most sensitive color region is the transition from red to green, which occurs over a temperature change of less than 1 °C. Additional, quantitative information beyond the calibration curve can be obtained by careful analysis of the remaining two components of the color decomposition. These can be used to analyze the temperature in areas of the TLC clearing point, which exhibits a gradual fall in pixel intensity and the saturation of colors. Quantitative evaluation of these areas is difficult but possible, for example using neural networks to include complete image information in the color analysis [7.23].

Obtaining full calibration curves prior to each experimental run is not only tedious but also limits rapid repetition of different experimental configurations. Such repetitions are often necessary, for example when different TLCs are used to shift the analyzed temperature range. Observing the shape of different calibration curves taken under similar conditions we may find large similarities. Therefore in some cases it is possible to assume the existence of a general calibration curve, independent of the active range. A calibration procedure based on such a *master* curve would require only a few measurements to produce a useful calibration over an entire active range. Using a nondimensional representation of temperature *Hay* and *Hollingsworth* [7.6] obtained repeatability of their regression curves with an acceptable accuracy for TLCs painted onto a heated surface. Similarities are also observed for the regression curves obtained for TLC tracers (Fig. 7.4). For reproducible experimental conditions simple stretch and shift operations may be used to transform one of them to another. Such a procedure can be applied to account for small changes of TLC response, either due to aging or when a new mixture is prepared.

7.1.4 Examples

In the following we illustrate several applications of TLC tracers to study the natural convection of liquids in closed cavities, and also with a phase change (freezing of water). In conjunction with the experimental program, numerical simulations of the problem were performed using finite-difference models of the Navier–Stokes and energy equations [7.13, 18, 24, 25]. The significance of the full-field temperature and flow measurements for the verification of the numerical results becomes evident by a direct comparison of the evaluated and predicted fields.

The first experiment deals with natural convection in a cubic cavity with two vertical, isothermal walls kept at different temperatures. This flow configuration resembles a popular benchmark, an idealized case of the flow in a cubical cavity used to test numerical solutions of the Navier–Stokes equations [7.26]. The characteristic recirculating flow is generated in the cavity by the temperature gradients between the two opposite metal walls of the cube. In addition to its theoretical interest, this type of convective flow has numerous potential applications, among which probably the most popular

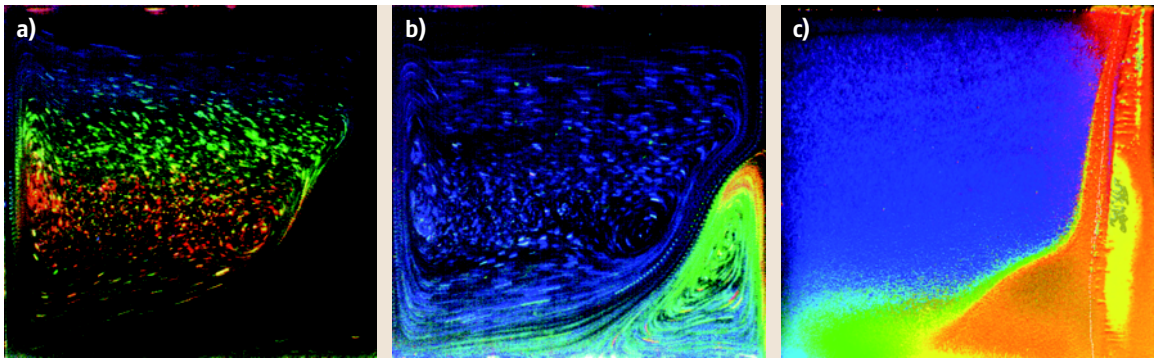

Fig. 7.5a–c Visualization of natural convection in water close to the freezing point, using a hot (left) wall at a temperature of 10 °C and a right wall at a temperature of 0 °C for **(a)** and **(b)**, −10 °C for **(c)**. Three types of liquid-crystal tracers were used to indicate the temperature variation: **(a)** encapsulated TLCs BM100/R6C12W showing details of flow and temperature for *normal* circulation (on the left); sum of 10 images taken every 1 s; **(b)** TLC mixture (TM445 and TM912) active at lower temperatures, visualizing the complex structure of *abnormal* circulation; sum of 20 images; **(c)** TLC mixture with a composition matched to the freezing point

is that of double glazing. Initially our interest was directed towards understanding the flow in the vertical central plane of the cavity. For this purpose, the observations of flow patterns and temperature fields were performed for several systems with increasing Rayleigh number [7.13, 14]. The flow structure in the differentially heated cavity strongly depends on the Rayleigh number. At small Rayleigh number ($Ra < 10^3$) the flow is dominated by conduction, which is seen in the form of vertical isotherms across the cavity. In the parameter range analyzed ($Ra = 2\times10^4 - 10^5$), both convection and conduction are important. At the lower end of the range, heat transfer due to convection begins to play a significant role, generating a vertical temperature gradient in the center of the cavity. The horizontal temperature gradient is positive everywhere. The streamlines correspond to a single roll located at the center of the cavity. This can be well observed in the multiply exposed photographs of liquid-crystal tracers conveyed by the flow of glycerol (Fig. 7.1a). At higher Rayleigh numbers ($Ra > 6\times10^4$), the horizontal temperature gradient becomes locally negative in some regions. This causes horizontal elongation of the streamlines and the development of a second roll in the core (Fig. 7.1b). By further increase of the Rayleigh number, a new flow regime is observed (Fig. 7.1c), with a strongly stratified temperature distribution in the center and thin thermal boundary layers at both isothermal side walls. This regime after increasing Rayleigh number above 10^8 leads to a transition to turbulence. Such a transition, easily identified using full-field temperature visualization and quantification, can be directly compared with numerical simulations of the corresponding cases.

Flow visualization via liquid crystals allows the observation of the flow structure and identification of variation of the temperature field. Even without quantitative data, the general shape of the isotherms can be deduced from the color photographs. However, despite the undoubted beauty of multiply exposed color photographs of liquid-crystal tracers, they have little value for quantitative image analysis. The lack of visible particles in large regions of the flow and their individual modulation of color are the main obstacles to computerized analysis. Hence, digital images of flow taken to implement particle image velocimetry and thermometry analysis exhibit a rather dense, uniform crowd of small, singly exposed colorful dots, representing a fine dispersion of the liquid-crystalline material in the flow. The human eye may still easily analyze the color distribution of such images (Fig. 7.5c), but particle displacements can be detected only by computational means.

The behavior of natural convection of water in the vicinity of the freezing point shows an interesting feature in the typical configuration with differentially heated walls. It is mainly due to the strongly nonlinear temperature dependence of the density function, which has an extremum at 4 °C. The competing effects of positive and negative buoyancy force result in a flow with two distinct circulations. There is a *normal* clockwise circulation, where the water density decreases with temperature (upper-left cavity region) and an *abnormal* convection with the opposite density variation and counterclockwise rotation (lower-right region). As mentioned, TLCs allow

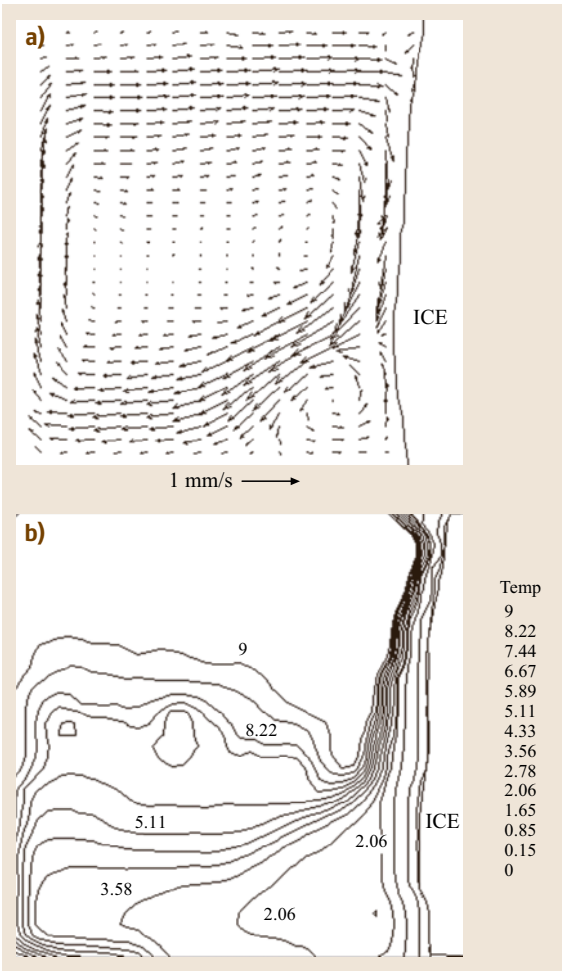

Fig. 7.6a,b Particle image velocimetry **(a)** and thermometry **(b)** applied to measure the velocity and temperature fields for natural convection in water freezing in a differentially heated cavity. Temperatures applied: 10 °C (on the left wall) and −10 °C (on the right wall)

the detection of temperature over a limited range of their color play regime. In some cases it is necessary to obtain precise information over a wider range of temperature variation, a task that is impossible to achieve with high precision for a single brand of TLCs. For steady or reproducible flow configurations it is possible to repeat the same experiment using different types of TLCs, as illustrated in Fig. 7.5. Regions of low temperature are visualized in Fig. 7.5a using TLCs operating in the temperature range 0–4 °C, and the same experiment is repeated in Fig. 7.5b to elucidate the temperature pattern in the left part of the cavity, using other types of TLCs.

To investigate natural convection with a phase change, one of the isothermal walls was held at a temperature of $T_c = -10$ °C. As this is below the freezing temperature of water, ice is formed at the cold wall (Fig. 7.5c). Initially uniform growth of the ice layer is quickly modified by the two colliding *normal* and *abnormal* circulations. In the upper part of the cavity, convective heat transfer from the hot wall is limited by the abnormal circulation, separating it from the freezing front. Figure 7.6 demonstrate the ability of TLCs to resolve simultaneously the transient variation of the velocity and temperature fields. These data, which were compared with numerical simulations performed for the freezing problem [7.24], led us to discover significant discrepancies and indicated directions to improve the model [7.27–29].

In the second solidification experiment flow in a cube with only one isothermal wall was investigated. The top isothermal wall was kept at a low temperature and the other five walls were nonadiabatic, allowing a heat flux from the fluid surrounding the cube. The temperature at the internal surfaces of the cube adjusted itself depending on both the flow and the heat flux through and along the walls. The lid-cooled cubic cavity was selected to investigate the convective flow with and without a phase change (freezing of water at the top wall). When the phase change occurs, the configuration resembles to some extent a directional solidification in a Bridgman furnace used for crystal growth (Fig. 7.7). Physically this configuration bears some similarity to the Rayleigh–Bénard problem. The symmetry of the enclosure imposes a strong downward flow along the vertical axis of symmetry. However, before a stable final flow structure is achieved, several oscillatory changes in its pattern are observed [7.30, 31]. The initial flow instabilities are seen well in the temperature and velocity fields visualized by TLCs in the box and could be confirmed in the numerical simulations. The formation of ice has been studied by decreasing the lid temperature to −10 °C. A complicated flow pattern with azimuthally varying structure was also reproduced in the star-like ice surface [7.32]. It was found that the creation of the ice layer at the lid has a stabilizing effect on the flow. This follows from the symmetry of the solid ice surface, which imposes the direction and character of the flow, eliminating the instabilities observed in the pure convective case. There is also a density inversion under the lid that decelerates the main jet and limits convective heat flux in that region [7.33].

Another example of the investigated configurations illustrates the simulation of flow characteristics accompanying the casting processes (Fig. 7.8). For this purpose

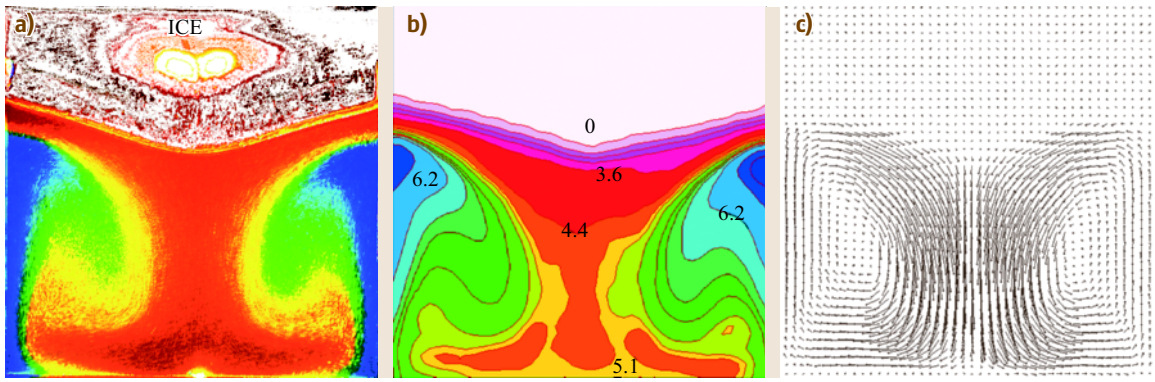

Fig. 7.7a–c Ice crystal growing from the top in a lid-cooled cavity in a Plexiglas cube immersed in an external water bath at a temperature of 20 °C. The isothermal metal lid has a temperature of −10 °C. Unencapsulated mixture of thermochromic liquid crystals (TM445 and TM912) used as tracers to evaluate both the temperature and velocity flow fields. **(a)** Superposition of five recorded images taken every 400 ms, **(b)** the evaluated temperature, and **(c)** the velocity fields

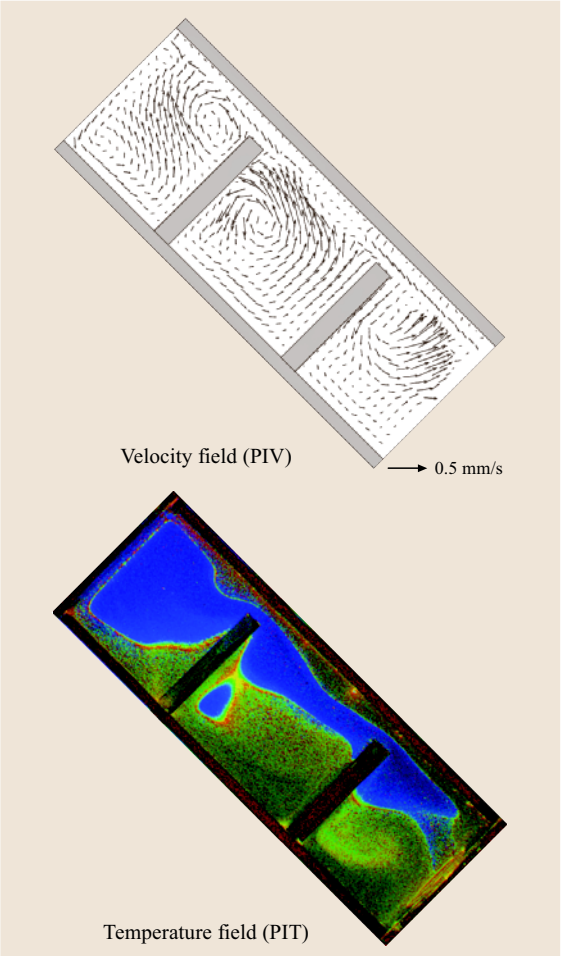

Fig. 7.8 Velocity field and temperature distribution visualized for the cavity inclined at 45°. Two cold isothermal walls (upper and lower) are responsible for sudden cooling of the fluid. This changes the color of the seeded liquid crystals (TM446) from blue (hot) to red (cold regions)

a rectangular cavity with two isothermal walls was filled with pressurized hot, viscous liquid (glycerol). The main features of the experiment, such as flow acceleration and deceleration at obstacles, a free surface flow and a sudden increase of the fluid viscosity on cooling, are typical for melt solidification in a mould. In contrast to a real casting, use of TLCs as tracers enables full-field measurement of the temperature and velocity fields. Quantitative transient data for the velocity and temperature fields were collected to verify and validate the numerical models used for typical casting problems. The main aim of the investigation was to create an experimental benchmark for the mould-filling problem [7.25, 34].

A similar rectangular, inclined box filled with water was used to simulate the up-slope, down-slope flow transition, typical for natural convection of air in valleys. Despite the differences in scales, some atmospheric phenomena, such as updraughts typical of the morning transition, down-slope front propagation during the evening transition, and nocturnal stable stratification can be visualized well in the laboratory experiment. To investigate up-slope flow phenomenon a negative temperature gradient is set up between the lower and upper wall, simulating solar heating of the ground. For transition and down-slope flow studies the temperature of the walls is reversed by switching the coolant settings. TLC tracers changing the color of refracted light with temperature indicate the onset of flow instabilities with periodically rising plumes and hot fluid ejections, analogous to those observed for diurnal circulation on long, sloping surfaces (Fig. 7.9). These periodical ejections could be identified well in the experimentally measured velocity fields and reproduced in the numerical simulation. After reversing the temperature gradient a transition front was observed both in the temperature field and the velocity field. The front builds up about 1 min after the reversal of temperature of the walls at a distance of 2 cm from the lower edge of the slope, and disappears about 5 min later, when regular nocturnal stratification of the temperature and the flow pattern develops [7.35].

7.1.5 Conclusions

Application of TLC tracers to laboratory studies of thermally driven flows appears to be, in most cases, the only option for acquiring full-field information about the temperature and velocity fields in liquids. The noninvasive character of the method and its relative simplicity enables a valuable tool for the full-field verification and validation of numerical results for small-scale laboratory configurations. We found that a large improvement in the quality and reliability of numerical simulations could be obtained by validating and tuning methodologies using information obtained from the full-field flow measurements described [7.36].

However, despite its apparent simplicity, TLC thermography requires tedious and frequently repeated calibrations to offer high-quality quantitative measurements. This is especially true for applications involving flow field measurements. Further investigations both in improving TLC stability and the robustness of color evaluation procedures are necessary.

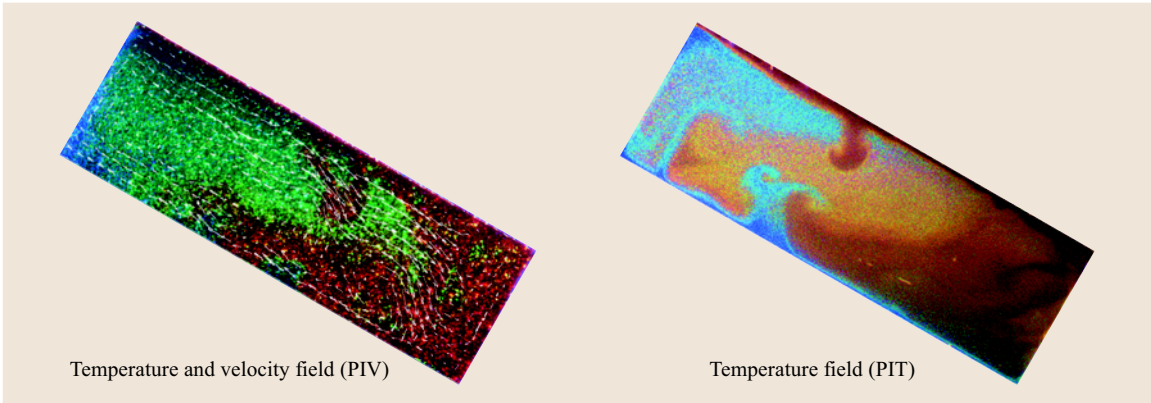

Fig. 7.9 Laboratory simulation of a diurnal up-slope flow, temperature and velocity measured with TLCs suspended in water. *Left*: unencapsulated tracers TM107 used to evaluate temperature and velocity fields in the cavity inclined at 30°; *right*: encapsulated tracers (TCC1001) visualizing the temperature field in the cavity inclined at 20°

7.2 Measurements of Surface Heat Transfer Characteristics Using Infrared Imaging

7.2.1 Introduction and Background

The use of infrared thermography has increased dramatically throughout the world over the past 15 years for the measurement of surface characteristics for a variety of research investigations involving convective heat transfer phenomena. The technique is especially viable and useful because it gives spatially resolved surface temperature distributions non-intrusively, even when large gradients of surface temperature are present. This can be done with high levels of accuracy and resolution, when the infrared imaging system and acquisition procedures are properly calibrated, and the nuances of camera behavior and infrared imaging are properly taken into account. In many research situations, the surface temperature distribution itself is of interest. However, its measurement is often one step in the determination of a variety of other spatially varying quantities that may be of interest, such as surface heat transfer coefficient distributions, nondimensional quantities containing surface heat transfer coefficients, surface adiabatic effectiveness, overall thermal effectiveness distributions, and thermal boundary condition information for numerical predictions of arrangements that are measured experimentally.

One critical step in the use of infrared thermography is the calibration of the images in some way so that local surface temperatures can be determined from the different shades, gray scales, or colors within infrared images. This is possible analytically, but requires knowledge of a variety of physical characteristics such as the surface emissivity, the effective atmospheric transmittance, the temperatures of surrounding walls, the atmospheric temperature, and other quantities. Because of the complexity and limited accuracy that is possible with such an approach [7.37], most investigators use some form of in situ calibration instead. Such an in situ calibration procedure was described and used as early as 1968 by *Czysz* and *Dixon* [7.38] for surface measurements using thermographic phosphors. Details of in situ calibration procedures employed by other investigators for specific measurement apparatus and environments using infrared thermography are described by *Meyers* et al. [7.39], *Gartenberg* and *Roberts* [7.40], *Wendt* [7.41], *Westby* [7.42], *Martiny* et al. [7.43], *Sargent* et al. [7.44], *Schulz* [7.37], and others. In the *Meyers* et al. [7.39] study, film cooled combustor walls are investigated under transient conditions. During heating of the combustor, these investigators recorded data simultaneously from both the infrared camera scanner and thermocouples that were embedded in the walls of the chamber. These data were then used for a best-fit approximation of the calibration parameters of the camera. *Westby* [7.42] calibrates prior to measurements by stepping a test article through a series of indepen-

dently measured, steady-state temperatures, as infrared images of the article are recorded simultaneously. *Sargent* et al. [7.44], and *Schulz* [7.37] employ steady-state calibration procedures, by matching the measured local surface temperatures to gray scale values from black-and-white infrared images. Additional details of these calibration procedures are described later in the chapter.

When in situ calibrations are employed to obtain accurate spatially resolved surface temperature distribution data, infrared thermography is used for a variety of research problems, applications, and measurement environments with a variety of physical arrangements. For example, *Scherer* et al. [7.45], and *Scherer* and *Wittig* [7.46] describe measurements of convective heat transfer distributions on surfaces downstream of a backward-facing step, and downstream of a normal high-momentum jet, respectively. *Gartenberg* and *Roberts* [7.40] and *Wendt* [7.41] describe the use of infrared thermography for measurements in a variety of aeronautical and aerodynamic flows. *Westby* [7.42] uses related techniques for heat transfer measurements in rarefied flows.

Since the 1980s, and even more so in the 1990s, infrared thermography has been widely used for a variety of turbomachinery investigations and applications [7.37, 39, 44, 47–57]. Of these investigations, *Martiny* et al. [7.47], *Sen* et al. [7.50], *Gritsch* et al. [7.52, 53], *Yuki* et al. [7.51], *Sweeny* and *Rhodes* [7.54], *Schulz* [7.37], *Bell*, et al. [7.55], and *Furukawa* and *Ligrani* [7.56] investigate film cooling environments. *Meyers* et al. [7.39], and *Martiny* et al. [7.48] consider film and effusion cooled combustor walls. *Hedlund* et al. [7.49] and *Sargent* et al. [7.44] present measured results from the surfaces of swirl chambers used for internal cooling of turbine airfoil leading edges, and *Won* et al. [7.57] present measured results from a rib turbulator surface, used for the internal cooling of the mid-span regions of gas turbine blades and vanes.

Advances in measuring techniques and image analysis is continuing, with recent advances in these areas described by *Driggers* et al. [7.58]. These investigators also analyze some of the problems associated with laboratory measurement of sampled infrared imaging systems, and with processing the resulting images. Infrared thermography measurements made in a variety of other thermal systems, including on the surfaces of a passage with a rotating disc and within a rotating channel, are described by *Astarita* et al. [7.59], and *Cardone* et al. [7.60]. More recently, *Hindle* et al. [7.61] employed a fiber-based near-infrared absorption tomography system to measure distributions of hydrocarbons in the cylinder combustion chamber of an internal combustion engine. This technique takes advantage of the hydrocarbon absorption of 1.7 μm radiation using newly developed solid-state all-optoelectronic components.

These different investigations illustrate the variety of measurement environments where infrared thermography is employed to measure spatially resolved quantities on a surface or over a volume of interest. In every case, measured temperature distributions are used to deduce other quantities such as surface heat transfer coefficients, surface Nusselt numbers, surface film cooling effectiveness, or hydrocarbon distributions.

7.2.2 Chapter Organization

Infrared cameras are described in Sect. 7.2.3, the overall physical measurement arrangement is described in Sect. 7.2.4, and in situ calibration procedures are presented and discussed in Sect. 7.2.5. Subsections 7.2.6–7.2.10 then describe five different quantities measured and determined using infrared thermography, for five different physical situations. Specific procedures and approach details are given for measurement of these different quantities, which can be used in a variety of other physical situations and measurement environments. Included are specific examples and applications of in situ calibration of infrared thermography systems, and different approaches for capturing and processing infrared camera images to obtain useful information. A summary and conclusions are finally presented in Sect. 7.2.11.

7.2.3 Infrared Cameras

There are two general types of infrared thermography systems, scanning systems and staring systems. Scanning systems measure surface radiation point by point. Oscillating mirrors and rotating prisms are then used to transfer object points to a single infrared detector. Staring systems use infrared sensor arrays or focal-plane arrays. With this arrangement, every element of the object is transferred to a corresponding sensor element of the focal plane. Because of the considerable progress that has been achieved with infrared sensor arrays in recent years (up to 3×10^5 elements, each 24 μm by 24 μm in size), the majority of infrared cameras that are used today are staring systems.

Infrared camera systems generally operate over one of three different wavelength regions or bands of the

infrared wavelength band, as it exists as part of the electromagnetic spectrum. These three bands are:

1. the short-wavelength infrared (SWIR) or near-infrared (NIR) band, which extends from 0.4 μm to 2–3 μm,
2. the mid-wavelength infrared (MWIR) or mean-infrared band, from 2–3 μm to 5 μm, and
3. the long-wavelength infrared (LWIR) or far-infrared (FIR) band, which extends from 8 μm to 12 μm.

The wavelength band employed depends on the application and measurement requirements. For example, the NIR or SWIR wavelength band is generally employed for laser applications. The MWIR and LWIR bands are generally used for thermal imaging and temperature detection, with important differences in the technologies employed in cameras that operate over these two different wavelength bands. Mid-wavelength infrared (MWIR) band cameras generally produce higher-quality images with better resolution and better magnitudes of noise equivalent temperature difference (NETD) compared to LWIR cameras. In contrast, LWIR cameras often operate with an uncooled focal-plane array of detectors, which makes them less expensive.

The different wavelength bands and the spectral emissivity are important when determining surface temperatures from measured spectral radiation. The relations, based on Planck's laws, for infrared energy levels also apply when the number of photons is quantified. This is important because numerous infrared cameras use photon detectors as sensing elements. The detectors most often used in the SWIR band are short mercury cadmium telluride, or indium gallium arsenide (InGaAs). The detectors most often used in the MWIR band are indium antimonide (InSb), or mercury cadmium telluride. The detectors most often used in the LWIR band are microbolometers (MB), gallium arsenide (GaAs), or mercury cadmium telluride. The typical detector size for all three wavelength bands is 30×30 μm for a 320×256 focal plane array, and 25×25 μm for a 640×512 focal plane array. Each element in each focal-plane array contributes to one pixel value in the infrared image. Many commercial infrared camera systems also include elaborate and advanced software, and data-processing capabilities to process digital images. This is accomplished either with real-time or digital data-acquisition systems. Many advanced cameras also have high frame rate and windowing capabilities with 14 bit processors. The resulting dynamic range images can then be acquired using real-time video reorders, with frames rates of 25 Hz, 30 Hz, or 60 Hz.

7.2.4 Overall Physical Arrangement

A typical test setup arrangement for measuring surface temperatures is shown in Fig. 7.10 [7.37]. Here, the incident radiation onto the infrared camera I_{meas} is comprised of:

1. the radiation from the test surface $I_{T,obj}$, which is attenuated by the atmospheric transmittance τ,
2. the radiation from the surroundings $I_{T,amb}$ (i. e., the flow channel and the side walls), and
3. the radiation that has been reflected from the test surface and also attenuated by the atmospheric surroundings $I_{T,atm}$.

Note that the atmosphere itself may also be emitting radiation into the camera. The test surface emission depends upon its emissivity ε because such surfaces are not perfect black bodies. If radiation from the atmosphere itself is neglected, according to *Schulz* [7.37], the measured radiation is then given by the relation

$$I_{meas} = \tau\varepsilon I_{T,obj} + \tau(1-\varepsilon)I_{T,amb} + (1-\tau)I_{T,atm} \, .$$

The effective atmospheric transmittance consists of the transmittance of the hot gas, the infrared translucent window, and the surrounding air. In the test arrangements described in this chapter, the windows are either sapphire, sodium chloride, or zinc selenide, which are used because of their high transmittance in the appropriate wavelength range and their high temperature resistance.

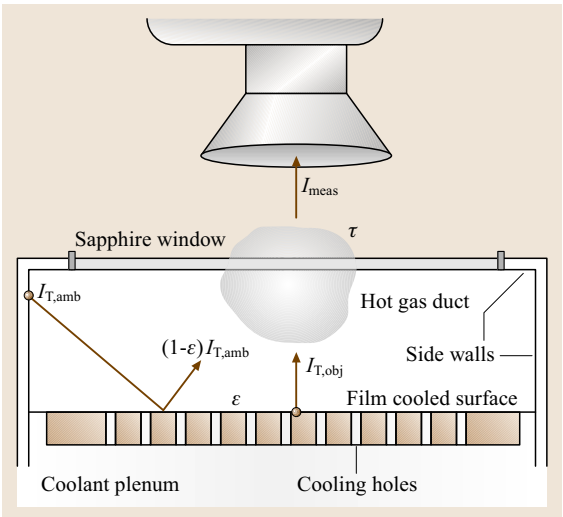

Fig. 7.10 Schematic diagram of a typical measuring situation using infrared thermography to analyze surface temperatures (after [7.37], used by permission)

Overall, the physical arrangement shown in Fig. 7.10, which includes this variety of physical phenomena described, is quite complicated. To overcome these complications and to obtain accurate measurement of surface temperature distributions, many investigators employ in situ calibration procedures, such as the ones that are briefly described in the next section.

7.2.5 In Situ Calibration

There are a variety of approaches to calibrating infrared camera systems to obtain thermal data. One of the most accurate means to calibrate infrared camera systems for measurement involves in situ calibration procedures. With this approach, the camera, imaging, and data-acquisition systems are all calibrated together in place within the experimental facility, and the calibrations are generally conducted simultaneously as the measurements are obtained.

In situ calibration procedures, like the ones described by *Sargent* et al. [7.44], are now widely used throughout the worldwide engineering community. Here, the infrared images are calibrated at the same times as the measurements are made by using thermocouples for simultaneous surface temperature measurements. Surface temperatures are thus measured at discrete locations (using thermocouples) at the same moment as each infrared image is recorded. With this approach, the relationship between infrared image gray scales and surface temperatures is determined for each infrared image. This relationship is a second- of third-order polynomial where temperature is a function of gray scale value. With this calibration polynomial, recorded digitized data, and location maps of thermocouple positions, surface temperature distributions over the entire test surfaces are determined from spatially resolved distributions of gray scale values recorded with the infrared camera. Magnitudes of spatially resolved convective heat transfer coefficients, Nusselt numbers, or surface effectiveness values are then determined from these and other measurements.

Similar calibration procedures are used for all five of the situations described in this chapter. In every case, some camera output parameter, such as the infrared image gray scale value, is correlated to temperature. These temperature values are determined from some other, independent means to measure local temperatures on the same surface from which the infrared images are obtained. In most cases, thermocouples are used for these local temperature measurements, which are recorded simultaneously as the infrared images of the surfaces are recorded.

Questions regarding a thermocouple's accuracy arise when applying thermocouple-based correction procedures to infrared thermography. A thermocouple always only senses the temperature of its junction. One error that may then result is the ability of a thermocouple junction to accurately measure the surrounding temperature of the material within which it is embedded, as well as the temperatures of nearby surfaces (from which an infrared image is obtained). This ability depends upon the thermocouple size, location, mounting arrangement, position, materials, wire lead arrangement and orientation, hole depth, relative temperatures, and materials and the material within which it is mounted. When transient measurements are undertaken, this task is further complicated by the thermal inertial influences of the thermocouple as well as the surrounding mounting substrate.

According to *Schulz* [7.37], the accuracy of a thermocouple reading also depends upon its calibration curve, and upon its exact position in the surface and its orientation with respect to temperature gradients. The latter is especially important when high surface temperature gradients are present. Even very small discrepancies between the thermocouple position and the location of the according pixel of the infrared image can lead to pronounced temperature differences. For the calibrations used in investigations by *Schulz* [7.37], *Gritsch* et al. [7.52, 53], *Furukawa* and *Ligrani* [7.56], *Won* et al. [7.57], and others, only those thermocouples located in approximately uniform temperature areas are employed, while thermocouples located in regions of large temperature gradient are excluded from the calibration procedure.

In some cases, additional refinements and alterations to in situ calibration procedures are employed [7.37]. These include extensive numerical analysis of infrared data to reduce the root-mean-square error values of temperature measurement differences and errors. For the investigations described by *Schulz* [7.37], these are based on the relationship between the measured radiation and surface temperature, as produced by the AGEMA Thermovision 900 camera and software.

7.2.6 Measurement of Surface Nusselt Numbers

Here, the use of infrared thermography to measure spatially resolved distributions of surface heat transfer coefficients, and surface Nusselt numbers on the interior surface of a swirl chamber is described. Swirl chambers are used in a wide variety of applications because of

the heat and mass transfer increases they provide. For example, swirl chambers are employed in heat exchangers, automobile engines, furnaces, biomedical devices, and devices used for heating and cooling of metal ingots. They are also used to fractionate solid particulates suspended and transported in liquids and gases, to enhance mixing processes in combustion chambers, and for spray-drying applications used with atomizers.

In the investigation of *Hedlund* et al. [7.49], the heat transfer coefficient h is given by

$$h = \frac{\dot{q}''}{(T_w - T_i)} ,$$

where $\dot{q}''$ is the surface heat flux, T_w is the local surface temperature, and T_i is the mixed mean air temperature at the inlet of the swirl chamber. The surface Nusselt number is then determined using $\mathrm{Nu} = hD/k$, where k is the air thermal conductivity, and D is the inner diameter of the main cylinder of the swirl chamber. For the results that are presented from *Hedlund* et al. [7.49], a constant surface heat flux boundary condition is applied to the test surfaces, and the inlet mixed mean air temperature T_i is also invariant as each experimental data set is obtained. Thus, variations of h and Nu are linked to spatial variations of surface temperature T_w, which are measured with infrared thermography.

Swirl Chamber for Heat Transfer Measurements

A schematic of the swirl chamber used for heat transfer measurements is shown in Fig. 7.11, including the coordinate system. The acrylic cylinder of the swirl chamber contains 30 copper–constantan thermocouples, and its inner surface is adjacent to the airstream. Each of these thermocouples is located 0.051 cm below this surface to provide measurements of local surface temperatures, after correction for thermal contact resistance and the temperature drop through the 0.051 cm thickness of acrylic. Acrylic is chosen because of its low thermal conductivity ($k = 0.16\,\mathrm{W/mK}$ at 20 °C) to minimize axial and circumferential conduction along the test section, and thus minimize smearing of spatially varying temperature gradients along the test surface. Acrylic also works well for infrared imaging because of its surface emissivity value.

Surface Nusselt Number Measurement Procedures

Infrared imaging is used to measure spatially resolved surface temperature variations along the inner surface of the swirl chamber. To do this, the infrared radiation emitted by the heated interior surface of the swirl chamber is captured using a VideoTherm 340 infrared imaging camera [7.62], which operates at infrared wavelengths of 8–14 μm. Temperatures, measured using the 30 calibrated copper–constantan thermocouples distributed along the swirl chamber surface adjacent to the flow, are used to perform the in situ calibrations simultaneously as the radiation contours from surface temperature variations are recorded.

This is accomplished as the camera views the test surface through a custom-made, cylindrical zinc selenide window, which transmits infrared wavelengths

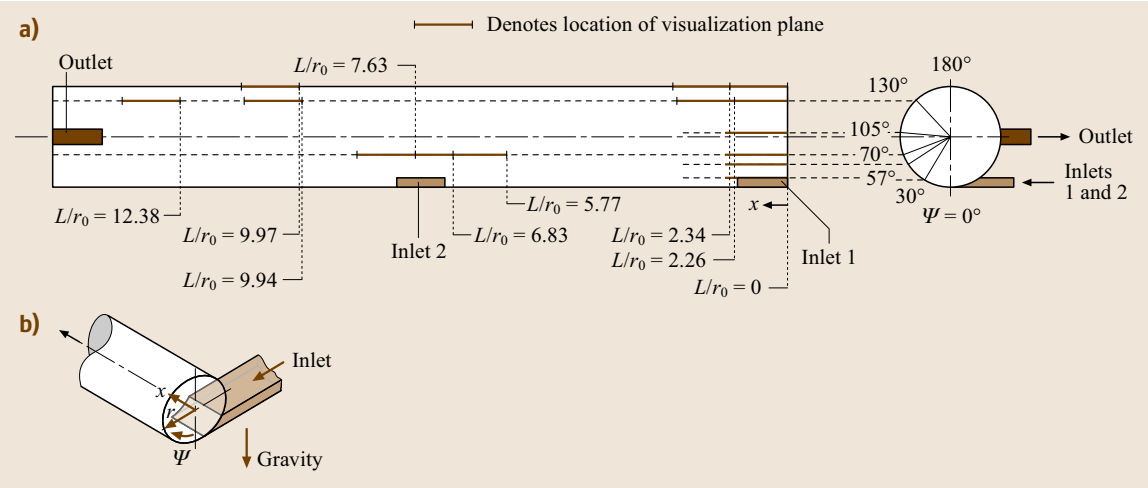

Fig. 7.11a,b Schematic diagrams of the swirl chamber used for heat transfer measurements including the coordinate system **(b)** and arrangement of inlet and outlet ducts **(a)** [7.49]

between 6 and 17 μm. Reflection and radiation from surrounding laboratory sources are minimized using an opaque shield that covers the camera lens and the zinc selenide window. Frost build-up on the outside of the window (due to the fact that the air inside the swirl chamber is cooled to less than 1 °C) is eliminated using a small heated airstream from a hair dryer. The window is located on a segment of the swirl chamber that is either rotated or relocated axially so that the camera can view different portions of the interior surface of the swirl chamber. At least two, and as many as five, thermocouple junction locations are present in any field viewed by the camera. The exact spatial locations and pixel locations of these thermocouple junctions and the coordinates of a 12.7 × 12.7 cm field of view are known from calibration maps obtained prior to measurements. During this procedure, the camera is focused, and rigidly mounted and oriented relative to the test surface in the same way as when radiation contours are recorded.

With these data, grey scale values at pixel locations within videotaped images from the infrared imaging camera are readily converted to temperatures. Examples of such calibration data are shown in Fig. 7.12 for three different window camera views of the swirl chamber test surface. Because such calibration data depend strongly on camera adjustment, the same brightness, contrast, and aperture camera settings are used for all three data sets. Each calibration data set shown in Fig. 7.12 is curve-fit to a second- or third-order polynomial equation. The slight difference between the three calibration data sets is because the transmissivity of the zinc selenide window and the emissivity of the swirl chamber test surface

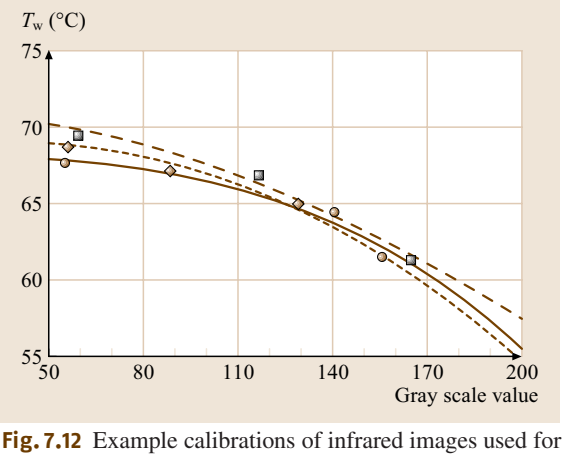

Fig. 7.12 Example calibrations of infrared images used for different window orientations and different camera views into the swirl chamber [7.49]

both exhibit small variations as the camera angle, camera and test surface orientation, surface temperatures, or experimental conditions are changed. The in situ calibration approach rigorously and accurately accounts for these variations.

For these measurements, the images from the infrared camera are recorded as 8 bit gray scale images on commercial videotape using a video recorder. Images are then digitized using software, operated on a desktop personal computer (PC). Subsequently, software is used to perform coordinate transformations to correct for nonrectangular, stretched, or distorted recorded images because of camera perspective or because the camera lens orientation is not normal to the curved target surface. This software also converts each of the 256 possible gray scale values to temperature at each pixel location using calibration data, and determines values of local Nusselt numbers. Contour plots of local surface temperature and Nusselt number (in *unrolled* planar, Cartesian coordinates) are prepared using graphics software. Each individual image covers a 250 × 250 pixel area.

Local Surface Nusselt Number Results

The surface Nusselt number distribution measured just downstream of the second inlet of the swirl chamber is shown in Fig. 7.13b. Included is the enhanced infrared image used to determine this distribution, presented in Fig. 7.13a. These data are given for $\mathrm{Re} = 19\,400$ ($\mathrm{Re_D} = 7205$) and $T_i/T_w = 0.85$. The location of the data, based on the coordinate system shown in Fig. 7.11, is $x/r_0 = 7.0–8.0$ and $\psi = 0–50°$. Here, Re is the Reynolds number based on the inlet duct characteristics, $\mathrm{Re_D}$ is the Reynolds number based on the swirl chamber main cylinder characteristics, T_i is the air mixed-mean temperature at the swirl chamber inlet, T_w is the local surface temperature, x is the axial distance measured from the swirl chamber end face, r_0 is the radius of the large cylinder comprising the swirl chamber, and ψ is the circumferential angle measured from the swirl chamber vertical plane. The surface Nusselt number variations in Fig. 7.13b show clear evidence of an array of Görtler vortex pairs, which develop in the chamber as the flow exits the second inlet passage of the chamber. In Fig. 7.13a, these are indicated by the collection of light and dark stripes, which correspond to vortex pair trajectories along the concave inner surface of the chamber. This image is as recorded directly from the camera with some enhancement, but with no corrections for camera angle and perspective. The surface temperature increases in Fig. 7.13a as image regions become lighter and whiter. Lower surface temperatures then coincide

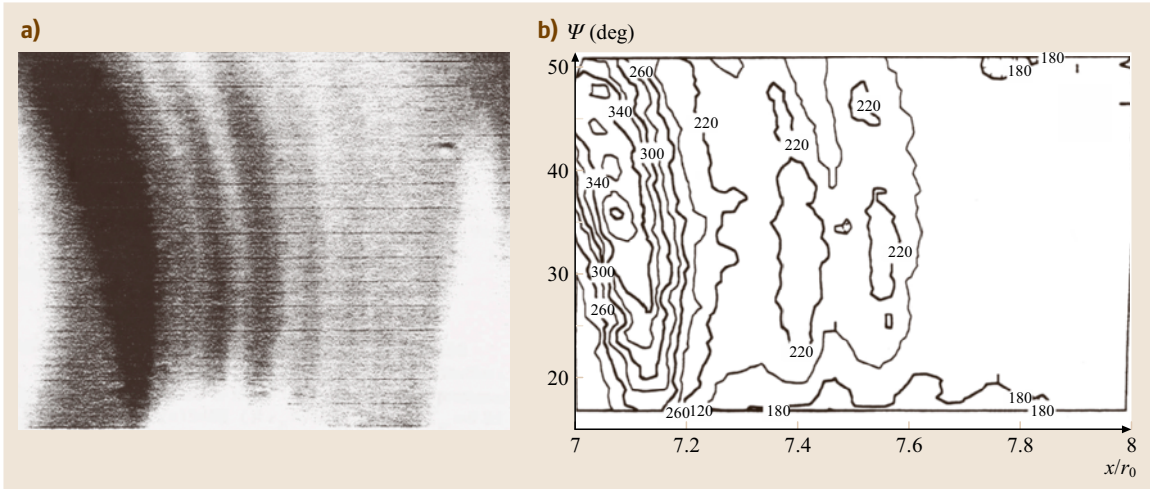

Fig. 7.13a,b Surface Nusselt number variations due to Görtler vortex pairs in the swirl chamber for Re = 19 400 (Re_D = 7205) and $T_i/T_w = 0.85$ at $x/r_0 = 7.0–8.0$ and $\psi = 0–50°$ just downstream of the second inlet [7.49]: **(a)** enhanced infrared image, **(b)** Nusselt number contours

with higher local Nusselt numbers, and higher surface temperatures coincide with lower local surface Nusselt numbers [7.49].

The spatially resolved surface Nusselt numbers determined from this infrared image are shown in Fig. 7.13b. In spite of the relatively high Reynolds number of this flow, important Nusselt number variations due to the Görtler vortex pairs are evident, where higher and lower local Nusselt numbers correspond to vortex pair downwash and upwash regions, respectively [7.49]. The high Nusselt number region located at $x/r_0 = 7.0–7.2$ in Fig. 7.13 is due to the shear layer near the edge of the inlet jet. This shear layer contains vortex structures that also contribute to surface Nusselt number enhancements. Such results illustrate the excellent accuracy and spatial resolution obtained with the infrared imaging and measurement techniques employed in this particular investigation [7.49].

7.2.7 Measurement of Surface Adiabatic Film Cooling Effectiveness

In this section, the use of infrared thermography to measure another quantity of interest to heat transfer researchers, the surface adiabatic film cooling effectiveness, is described. Such data are useful in film cooling investigations, and are needed to determine the performance and protection provided by different film cooling hole configurations. Effective performance of the films produced by these configurations is important for cooling blades and vanes in the turbines of gas turbine engines. Such cooling maintains acceptable metal temperatures, and in doing so, maintains blade and vane durability, reliability, and lifetimes for safe and efficient gas turbine engine operation. In efforts to design film cooling holes with improved performance, recently attention has been devoted to contouring the holes employed [7.52, 53, 55, 56].

Surface adiabatic film cooling effectiveness distributions from holes with diffuser-shaped expansions are described here because these are believed to improve film cooling performance relative to holes that are cylindrical [7.55, 56]. This is accomplished as the increased cross-sectional area reduces the exit velocity and thus the momentum flux of the film as it exits the holes. The penetration of the film jet into the main flow is then reduced, which gives higher overall film cooling effectiveness. The lateral expansion of such holes also causes improved lateral spreading of the film concentrations which leads to more-uniform coverage of the test surfaces with protective film cooling air [7.55, 56].

One parameter that quantifies film cooling performance is the adiabatic film cooling effectiveness, η [7.56]. For high-speed flows, where compressibility and viscous dissipation are non-negligible, this quantity is given by

$$\eta = \frac{(T_{aw} - T_{r\infty})}{(T_{oc} - T_{r\infty})} ,$$

where T_{aw} is the surface adiabatic temperature, $T_{r\infty}$ is the free-stream recovery temperature, and T_{oc} is the coolant stagnation temperature [7.56]. As such, the adiabatic effectiveness η is the ratio of actual surface temperature reduction due to the cooling film, and the maximum possible temperature reduction given by the temperatures of the coolant and mainstream gas. In the investigations of *Gritsch* et al. [7.52, 53], *Bell* et al. [7.55], and *Furukawa* and *Ligrani* [7.56], $T_{r\infty}$ and T_{oc} are maintained constant during a given test, and the spatial variation of surface adiabatic temperature T_{aw} is measured using infrared thermography. In most test arrangements, a material with low thermal conductivity is employed to produce an adiabatic test surface where T_{aw} is measured. In the results from *Gritsch* et al. [7.52,53], which are presented to illustrate adiabatic effectiveness determination using infrared thermography here, data for three different hole configurations are presented, each for three different film cooling blowing ratios. The blowing ratio M is the ratio of mass flux provided by the coolant at the inlet of the cooling holes, and the mass flux in the free stream of the mainstream gas.

Experimental Arrangements and Apparatus for Surface Effectiveness Measurements

The single film cooling hole arrangements employed by *Gritsch* et al. [7.52,53] are shown in Fig. 7.14. The three configurations are: cylindrical, fan-shaped, and laid-back fan-shaped. The exit-to-entry ratio for the fan-shaped, and laid-back fan-shaped holes are 3.0 and 3.1, respectively. For the infrared thermography measurements downstream, the bottom test wall is equipped with thermocouples to measure local surface temperatures, which are also employed for in situ calibration of the infrared images. The surface is also painted with a black color with a high, temperature-independent emissivity to ensure good radiative properties. The camera observes this test surface through a sapphire window located in the top wall of the test section channel. All results are obtained under steady-state thermal-equilibrium conditions.

The infrared camera employed to obtain these data is an AGEMA Thermovision 900 device with two indium antimonide (InSb) detectors [7.63]. The detector within this scanner operates in the 2–5.6 μm spectral range. To insure low-noise operation, the detector is cooled to approximately 80 K using a Stirling motor. In contrast to liquid-nitrogen-cooled scanners, the Stirling-cooled infrared scanner allows for arbitrary observations in multiple directions and unlimited operation, which is useful when infrared thermography is employed in laboratory

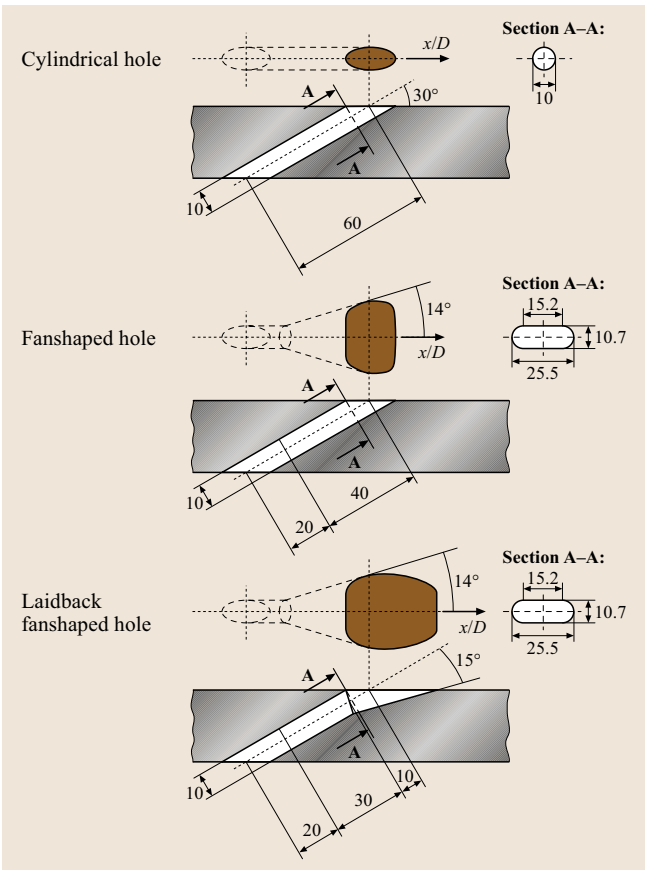

Fig. 7.14 Single shaped film cooling hole arrangements with expanded exits employed in the investigations by *Gritsch* et al. (after [7.37, 52, 53], used by permission)

conditions. Each infrared image produced consists of 136 lines, with each line consisting of 272 samples. The corresponding image acquisition frequency is 15 Hz, which can be doubled by using half the number of scan lines.

Local Surface Adiabatic Film Cooling Effectiveness Results

Figure 7.15 shows adiabatic surface film cooling effectiveness distributions for the cylindrical, fan-shaped, and laid-back fan-shaped holes for blowing ratios M of 0.5, 1.0, and 1.5, where x represents the streamwise distance along the test surface, z represents the spanwise distance along the test surface, and D is the entrance diameter of the film cooling holes. In this multi-part figure, the film produced by the cylindrical hole detaches from the surface at a blowing ratio M of 1.5, result-

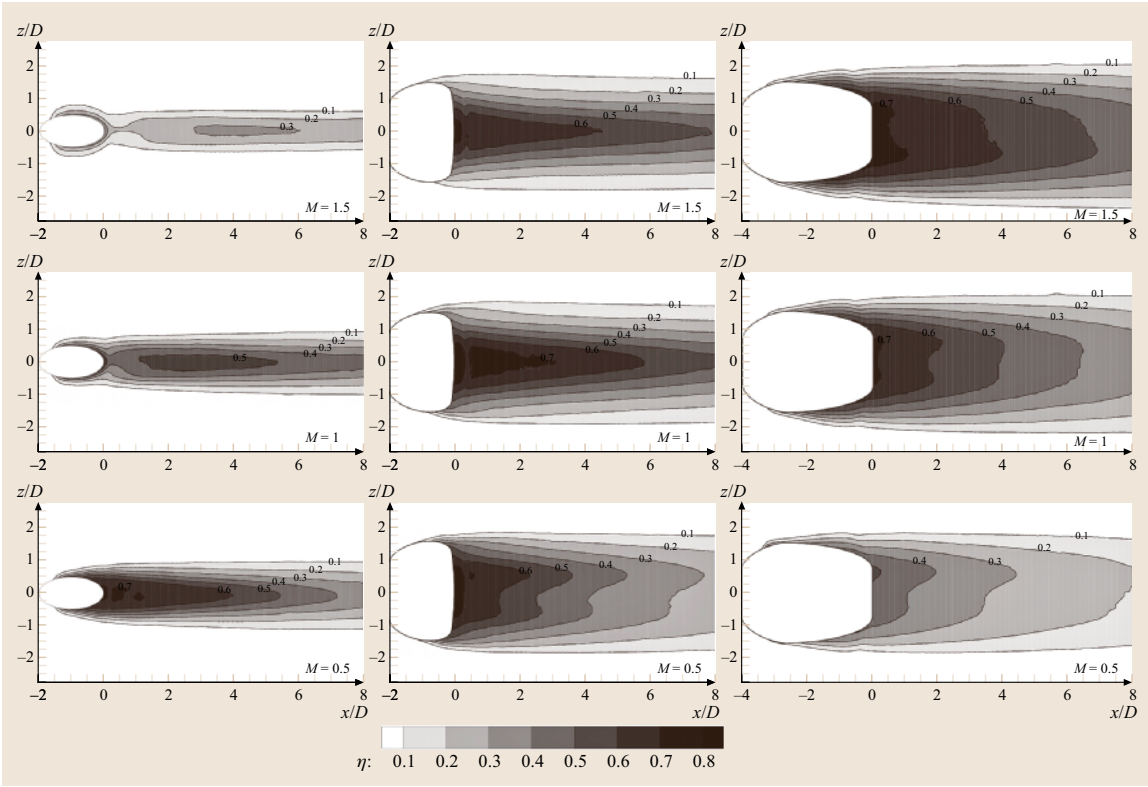

Fig. 7.15 Surface adiabatic film cooling effectiveness distributions obtained using the hole arrangements shown in Fig. 7.14 from investigations by *Gritsch* et al. [7.37, 52, 53]. Surface distributions are given for different hole arrangements and different film cooling blowing ratios (used by permission)

ing in relatively low values of adiabatic effectiveness. Decreasing the blowing ratio increases the local effectiveness magnitudes downstream of the cylindrical holes because the penetration of the jet into the main flow is reduced [7.37, 52, 53]. For all three blowing ratios, lateral spreading of the film downstream of the cylindrical hole is very poor. Significantly higher magnitudes of adiabatic surface effectiveness are present downstream of the fan-shaped, and laid-back fan-shaped holes in Fig. 7.15. Lateral spreading of the film on the test surface is also improved for these hole configurations compared to the cylindrical hole, however, most of the coolant is still ejected along the centerline, resulting in pronounced lateral effectiveness gradients, especially at the higher blowing ratios. Note that a small separation region is present just downstream of the fan-shaped holes for higher blowing ratios, which is indicated by a local decrease in adiabatic film effectiveness. The centerline effectiveness magnitude for the laid-back fan-shaped hole is somewhat reduced compared to the distribution produced by the fan-shaped hole, although the lateral spreading is improved [7.52, 53].

7.2.8 Measurement of Surface Heat Flux Reduction Ratio

Increases in heat transfer coefficients due to film cooling injection can be combined with adiabatic effectiveness values (like those described in the previous section) to determine the heat transfer rates, and consequently, the net heat flux reduction Δq_r produced by film cooling. From *Sen* et al. [7.50], Δq_r is defined as

$$\Delta q_r = 1 - \frac{h_f(T_{aw} - T_w)}{h_0(T_{r\infty} - T_w)} .$$

Here, the subscript '0' denotes no film cooling, and the subscript 'f' denotes with film cooling. A nondimensional surface temperature can be defined using:

$$\theta = \frac{(T_{r\infty} - T_w)}{(T_{r\infty} - T_{oc})} .$$

Combining these equations with the defining equation for adiabatic film cooling effectiveness η then gives

$$\Delta q_r = 1 - \left(\frac{h_f}{h_0}\right)\left(1 - \frac{\eta}{\theta}\right) .$$

From this equation, it is evident that the net heat flux reduction can be determined from measurements of adiabatic film cooling effectiveness and the heat transfer coefficient ratio, h_f/h_0. The net heat flux reduction Δq_r is positive if film cooling gives a reduction in the heat transfer rate along the test surface. However, in some cases, injecting the coolant film into the flow along a surface increases the heat transfer coefficient, $h_f/h_0 > 1$, and negative values of Δq_r. In order to produce a net decrease in heat flux to the surface, the adiabatic effectiveness must be large enough to compensate for increases in the heat transfer coefficient ratio h_f/h_0 [7.50,51].

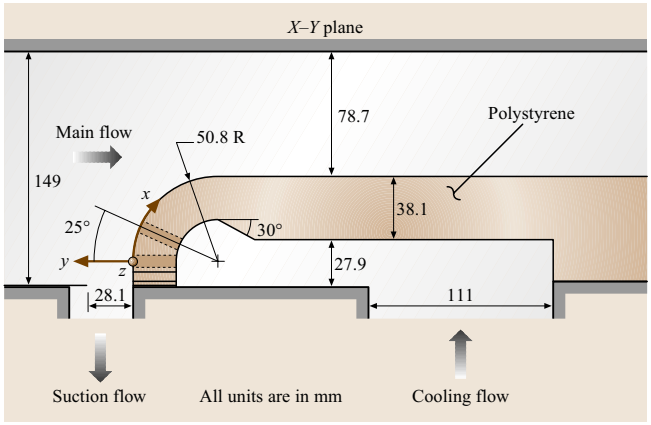

Fig. 7.16 Schematic diagram of a leading-edge test facility for heat flux reduction measurements using infrared imaging from *Yuki* et al. (after [7.51], used by permission)

Experimental Facility for Surface Heat Flux Reduction Measurements

Figure 7.16 shows a schematic diagram of the leading-edge test facility employed for heat flux reduction measurements using infrared imaging, from *Yuki* et al. [7.51]. This leading edge matches configurations for vane airfoil leading edges like those used in industrial gas turbine engines. The arrangement is a half-section leading edge. The test section is placed in the wind tunnel with a suction slot immediately in front of the leading edge to control the location of the stagnation line. The constant-radius leading edge contains two rows of holes, which are angled laterally at 90° with respect to the bulk flow direction. The two rows of holes are positioned 0° and 25° relative to the horizontal, at x/d locations of 0 and 3.5. Within the plane of each row of holes, the holes are angled 20° with respect to the test surface. The diameter of all holes is 6.35 mm. Each row contains nine holes with a spanwise hole spacing of 7.64 hole diameters. The rows are arranged so that holes in adjacent rows are staggered with respect to each other. The leading-edge thickness is 25 mm giving hole length-to-diameter ratios of 12. To minimize conduction error along the surface, the leading edge is made of extruded polystyrene foam with a thermal conductivity of 0.027 W/mK. The width of the suction slot and the amount of suction are adjusted so that the stagnation line is located at $x/d = 0$, and the stagnation streamline is parallel to the approaching mainstream direction. During heat transfer measurements, the mainstream velocity is set at 10 m/s, giving a Reynolds number based on the effective leading-edge diameter of 65 000 [7.51].

Infrared Imaging Procedures

Surface temperature data are collected using an Inframetrics 600L infrared camera [7.64] mounted 45° relative to the horizontal direction, and pointed towards the center of curvature of the leading edge. A window made of sodium chloride is used to allow maximum transmission of radiation emitted from the surface to the camera. The camera is calibrated by comparing camera-detected temperatures to values measured with type E ribbon thermocouples mounted at several positions along the test surface. According to *Yuki* et al. [7.51], the uncertainty magnitude of surface temperature measurements, determined from the curve-fit error for the linear calibration equation, is ±0.2 °C. The spatial resolution of the infrared measured surface temperatures is 0.5 times one film cooling hole diameter, where discrete pixel levels are based on integrated averages over a 3 × 3 mm surface area. This resolution is adequate to resolve measured temperature gradients except within one-half of one diameter of the film cooling holes because of the steep gradients of surface temperature at these locations. Mainstream and plenum temperatures are measured using type E thermocouples with an experimental uncertainty of ±0.1 °C.

To measure surface heat transfer coefficients, a sheet of 25 µm-thick stainless steel is attached to the leading edge to provide a constant heat flux surface. The 597 × 102 mm sheet covers the entire curved portion of the leading edge plus approximately 10 mm extra upstream and downstream to avoid end effects. Electrical current is directed through the plate using copper busbars attached on either end. Elliptically shaped holes,

1.2 mm wider than the film cooling holes, are cut into the steel sheet at the injection hole locations. To determine power input, the voltage across the stainless-steel plate and the current is determined from voltage measurements across a 3.33 m Ω shunt resistor connected in series with the heat flux plate. The total heat rate from the test plate is determined by subtracting the analytically determined radiative heat flux from the total heat flux. Conduction losses are estimated to be negligible. Local heat transfer coefficients are then determined from the convective heat flux, local surface temperature, and mainstream temperature. During testing the nominal plate temperature is 45 °C and the nominal mainstream temperature is 27 °C [7.51].

Net Heat Flux Reduction Results

The measured heat flux reduction distribution on the leading-edge test section is shown in Fig. 7.17 [7.51]. These data are given for a nondimensional temperature θ of 0.6, a density ratio of 1.0, and a momentum flux ratio of 3.5. For these data, the stagnation line is located at $x/d = 0$, where x represents the streamwise distance along the test surface, z represents the spanwise distance along the test surface, and d is the entrance diameter of the film cooling holes. Figure 7.17 shows that $\Delta q_r > 0$ over most of the surface, indicating improved performance relative to operation with no film cooling. Net heat flux reduction magnitudes are maximum at locations directly beneath the largest coolant concentrations, where adiabatic effectiveness magnitudes are maximum. However, downstream of the second row of holes, there is an elongated region where the net heat flux reduction is negative with values as low as $\Delta q_r = -0.4$. This region corresponds to locations along the test surface where heat transfer coefficients are augmented from local mixing near the edge of the coolant jets. Such data further illustrate the ability of infrared imaging to provide detailed, spatially resolved data on critical components in cooling applications subject to high-temperature gas environments.

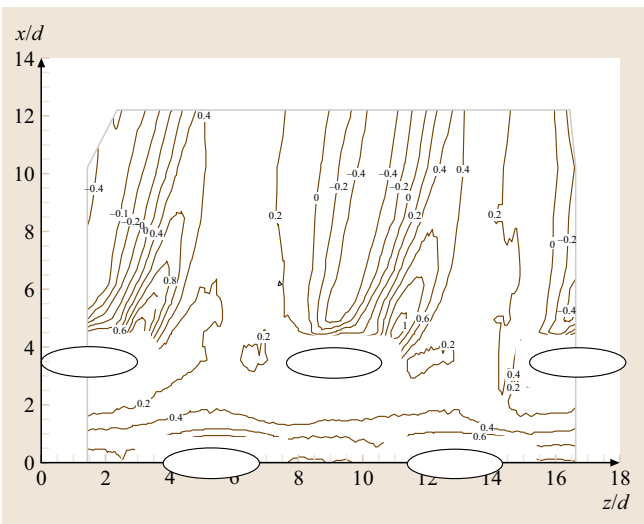

Fig. 7.17 Heat flux reduction distribution on the leading-edge test section from *Yuki* et al. [7.51] for $\theta = 0.6$, density ratio of 1.0, and momentum flux ratio of 3.5. The stagnation line is located at $x/d = 0$ (used by permission)

7.2.9 Transient Surface Temperature Measurements

Here, the use of infrared imaging to acquire transient, spatially resolved surface temperature distributions at different times is described. The technique is applied to biomedical therapeutic patch testing.

Infrared Imaging and Data Acquisition Procedures

Spatially resolved temperature distributions along a patch test surface are determined using infrared imaging in conjunction with thermocouples, digital image processing, and in situ calibration procedures. To accomplish this, the infrared radiation emitted by the heated patch surfaces is captured using a VideoTherm 340 infrared imaging camera [7.62], which operates at infrared wavelengths from 8 μm to 14 μm. Each patch, as it is tested, is mounted on a flat sheet of acrylic. Temperatures, measured using calibrated, miniature copper–constantan thermocouples distributed along the patch surface being measured, which is adjacent to still air, are used to perform the in situ calibrations simultaneously as the radiation contours from surface temperature variations are recorded. Because the patches are exposed to natural convection induced by laboratory air, no window to transmit infrared energy is required. Six thermocouple junction locations are present in the infrared field viewed by the camera. The exact spatial locations and pixel locations of these thermocouple junctions and the coordinates of a 1.3 × 1.3 cm field of view are known from calibration maps obtained prior to the measurements. During this procedure, the camera is focused, and rigidly mounted and oriented relative to the test surface in the same way as when radiation contours are recorded. Voltages from the thermocouples are acquired using a Hewlett Packard 44422T data-acquisition card installed in a Hewlett Packard 3497A data-acquisition

control unit, which is controlled by a Hewlett Packard A4190A series computer.

With these data, gray scale values at pixel locations within videotaped images from the infrared imaging camera are readily converted to local surface temperature values. Because such calibration data depend strongly on camera adjustment, the same brightness, contrast, and aperture camera settings are used to obtain the experimental data. The in situ calibration approach rigorously and accurately accounts for these variations.

Images from the infrared camera are recorded as 8 bit gray scale directly into the memory of a PC using a frame-grabber video card, and associated software. Three sets of 60 frames are recorded at a rate of one frame per second. All 180 resulting images are then ensemble-averaged to obtain the final gray scale data image. This final data set is then imported into software to convert each of the 256 possible gray scale values into the local Nusselt number at each pixel location using calibration data. Each individual image covers a 300 × 300 pixel area.

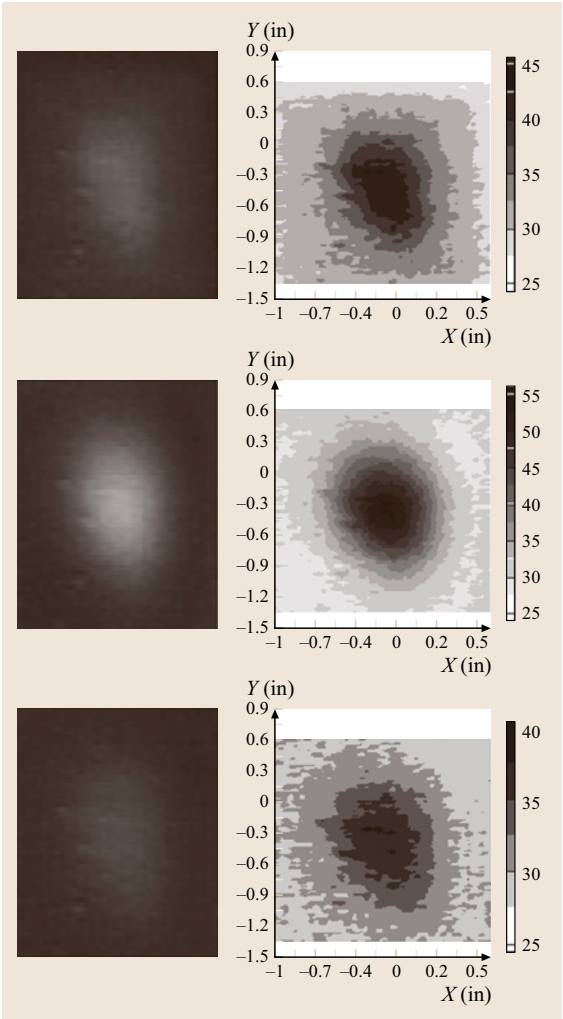

Fig. 7.18 Images acquired 1, 6, and 60 min from the beginning of testing of a biomedical therapeutic patch acquired to determine spatial and temporal surface temperature variations. Infrared camera images are shown in the left-hand column, with associated surface temperature contours presented in the right-hand column

Transient Surface Temperature Results

Figure 7.18 shows infrared images acquired 1, 6, and 60 min from the beginning of testing of one biomedical therapeutic patch. Here, X and Y represent the coordinates in two directions along the patch surface. Infrared camera images are shown in the left-hand column, with associated surface temperature contours presented in the right-hand column. Notice that the highest temperatures are located near the center of the patch for the 1 and 6 min data sets. As time proceeds, temperature levels drop near the center of the patch, and the outer portions of the patch heat up as energy is conducted away from the patch center. The time variations of the maximum temperature and spatially averaged patch temperature are shown in Fig. 7.19. The interesting feature of these data is the time of the maximum temperature,

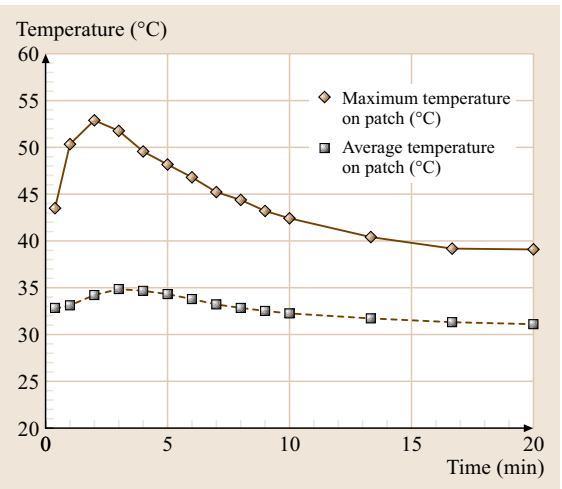

Fig. 7.19 Time variations of maximum temperature and average temperature from tests of the biomedical therapeutic patch

which is about 2 min after the test begins. Overall, such data illustrate the ability of infrared imaging, in situ calibration procedures, and digital image processing to provide spatially resolved, time-varying data for specific applications.

7.2.10 Boundary-Condition Information for Numerical Predictions

In this section, the use of infrared thermography to provide thermal boundary-condition information for numerical predictions is described. The test surface that is analyzed contains a collection of rib turbulators that are angled with respect to the flow stream. Overall, the vortices and the accompanying secondary flows produced by these rib turbulators aid convective processes for heat transfer augmentation by:

1. increasing secondary advection of fluid between the central parts of the channel and regions near the wall, and
2. producing regions with high three-dimensional shear and high magnitudes of turbulence production over much of the channel cross section, thereby substantially increasing turbulence transport levels in all three coordinate directions [7.65].

In many cases, remarkable enhancements of local and spatially averaged surface heat transfer rates are possible with rib turbulators, in spite of the lower local Nusselt numbers at certain locations along the ribbed surfaces. This is aided by the wide collection of secondary flow phenomena produced by the rib turbulators, which include flow recirculation zones both upstream and downstream of individual ribs, shear layer reattachment, pairs of counter-rotating flow cells, and different collections of small- and large-scale vortex pairs [7.65].

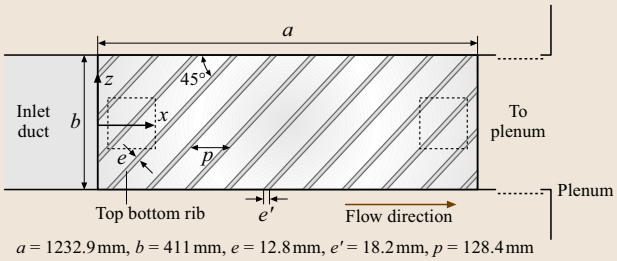

Fig. 7.20 Schematic diagrams of the rib turbulator test surfaces, including coordinate system [7.57]

In the discussion that follows, the Nusselt number Nu is given by

$$\mathrm{Nu} = h\frac{D_\mathrm{h}}{k} ,$$

where h is the heat transfer coefficient, D_h is the channel hydraulic diameter, and k is the molecular thermal conductivity of air. The heat transfer coefficient is then based on the flat projected area and is determined using

$$h = \frac{\dot{q}''}{(T_\mathrm{w} - T_\mathrm{m})}$$

where $\dot{q}''$ is the local surface heat flux, T_w is the local wall temperature, and T_m is the time-averaged, local mixed mean temperature. Nu_0 is then the baseline Nusselt number in a smooth channel with no rib turbulators.

Experimental Facility and Test Surface for Heat Transfer Measurements

Figure 7.20 shows the geometric details of the rib turbulator test surface, including the rib turbulator geometry. Prior to this ribbed turbulator test section is a 411 × 103 mm inlet duct that is 1219 mm in length. This is equivalent to 7.4 hydraulic diameters (where the hydraulic diameter is 164.7 mm). Two trips are employed on the top and bottom surfaces of the inlet duct, just upstream of the test section, which follows with the same cross section dimensions. The duct exits to another duct, and then to a 0.60 m square plenum. Figure 7.20 shows that a total of 13 ribs or rib segments are used on the top wall and on the bottom wall of the rib turbulator test section. As mentioned, these are arranged with 45° angles with respect to the streamwise flow direction, such that the ribs on opposite walls of the channel are parallel and aligned with respect to each other. Each rib is 12.8 mm high and has a square cross section. The ratio of the rib height to the hydraulic diameter is 0.78, the rib pitch-to-height ratio is 10, and the blockage provided by the ribs is 25% of the channel cross-sectional area [7.57, 65]. The top wall of the test section also has two cut-out regions (one at the upstream end and one at the downstream end) where a zinc selenide window can be installed to allow the infrared camera to view a portion of the test surface on the bottom wall. When this window is not in use, inserts with ribs (which exactly match the adjacent rib turbulators on the top wall) are used in its place. Also identified in Fig. 7.20 is the test section coordinate system employed for the study. Note that the Y coordinate is directed normal to the bottom wall [7.57].

All exterior surfaces of the facility are insulated with Styrofoam ($k = 0.024\,\mathrm{W/mK}$), or two to three layers

of 2.54 cm-thick, Elastomer Products black neoprene foam insulation ($k = 0.038$ W/mK) to minimize heat losses. Calibrated copper–constantan thermocouples are located between the three layers of insulation located all around the test section to determine conduction losses. Between the first layer and the 3.2 mm-thick acrylic test surfaces are custom-made Electrofilm etched-foil heaters (each encapsulated between two thin layers of Kapton) to provide a constant heat flux boundary condition on the flat horizontal, bottom surface of the ribbed test plate. The acrylic surfaces, which are adjacent to the airstream, contain 35 copper–constantan thermocouples, which are placed within the ribs as well as within flat portions of the test surfaces between the ribs. Each of these thermocouples is located 0.051 cm below the surface to provide measurements of local surface temperatures, after correction for thermal contact resistance and the temperature drop through the 0.051 cm thickness of acrylic. Acrylic is chosen because of its low thermal conductivity ($k = 0.16$ W/mK at 20 °C) to minimize streamwise and spanwise conduction along the test surfaces, and thus minimize smearing of spatially varying temperature gradients along the test surfaces. Energy balances performed on the heated test surfaces then allow the determination of the local magnitudes of the convective heat flux.

The mixed-mean stagnation temperature of the air entering the test section is measured using five calibrated copper–constantan thermocouples spread across its cross section. To determine this temperature, thermocouple-measured temperatures are corrected for thermocouple wire conduction losses, channel velocity variations, as well as for the differences between the stagnation and recovery temperatures. All measurements are obtained when the test facility is in a steady state.

Local Nusselt Number Measurement

To determine the surface heat flux (used to calculate heat transfer coefficients and local Nusselt numbers), the convective power levels provided by the etched foil heaters are divided by flat test surface areas. Spatially resolved temperature distributions along the bottom rib turbulator test surface are determined using infrared imaging in conjunction with thermocouples, energy balances, and in situ calibration procedures [7.44, 57]. To accomplish this, the infrared radiation emitted by the heated interior surface of the channel is captured using a VideoTherm 340 infrared imaging camera [7.62], which operates at infrared wavelengths from 8 μm to 14 μm. Temperatures, measured using the calibrated, copper–constantan thermocouples distributed along the test surface adjacent to the flow, are used to perform the in situ calibrations simultaneously as the radiation contours from surface temperature variations are recorded.

This is accomplished as the camera views the test surface through a custom-made zinc selenide window, which transmits infrared wavelengths between 6 and 17 μm, located on the top wall of the test section. Eleven to 13 thermocouple junction locations are usually present in the field viewed by the infrared camera. The exact spatial locations and pixel locations of these thermocouple junctions and the coordinates of a 12.7 × 12.7 cm field of view are known from calibration maps obtained prior to the measurements [7.57].

Images from the infrared camera are recorded as 8 bit gray scale directly into the memory of a PC computer using a frame-grabber video card, and associated software. Three sets of 60 frames are recorded at a rate of one frame per second. This is done after the rib turbulator flows are established to obtain data when the test surface is in a steady-state condition. All of the 180 resulting images are then ensemble-averaged to obtain the final gray scale data image. This final data set is then imported into software to convert each of the 256 possible gray scale values to local Nusselt number values at each pixel location using calibration data. Each resulting image then covers a 300 × 300 pixel area. Thermal conductivity in the Nusselt number is based on the average of the local wall temperature and the temperature of the air at the upstream inlet [7.57].

Conduction Analyses Within the Test Surface

Three-dimensional conduction along and within the test surface is determined using version 6.0 of the ANSYS numerical code. To accomplish this, a portion of the test surface, with one rib segment, is modeled using approximately 17 480 numeric node elements. In addition, a constant heat flux boundary condition (determined from values used in the experiments) is imposed on the back side of the 3.2 mm-thick acrylic test surface. Local surface temperatures, measured experimentally using infrared thermography, are used for the thermal boundary condition on portions of the test surface next to the airstream, including the top of the rib segment and the flat parts of the test surface around the rib. Temperatures are also imposed as the thermal boundary condition on the vertical parts of the rib segment, which are determined by interpolation of values measured at the edge of the rib top and at the corner (between each rib side and flat parts of the test surface) [7.57].

Ordinarily, without the conduction analysis applied, the same heat flux produced by the etched-foil heater is assumed to leave the test surface next to the airstream at the rib top and along the flat parts of the test surface around the rib. This means that no heat is assumed to leave the vertical side walls of the rib, and that all of the thermal power going into the test surface leaves entirely from the horizontal surfaces next to the airstream. The ANSYS version 6.0 conduction analysis is used to determine the nonuniform variations of the surface heat flux into the airstream, which are actually present, including along the vertical sides of the rib segment. As mentioned, this is accomplished using experimentally measured values as thermal boundary conditions around the domain solved by the numerical code.

Results with and Without Test Surface Conduction Analysis

The results presented in Fig. 7.21a for $Re_H = 17\,000$ (where Re_H is the Reynolds number based on the channel height) are again given in Fig. 7.21b, but with variable surface heat flux and surface conduction analysis applied. Comparison of these two figures thus provides information on the effects of three-dimensional conduction along and within the test surface. The results under these experimental conditions are chosen to illustrate these effects, because variations due to conduction are qualitatively similar to those observed at other Reynolds numbers. Note that the results in the latter figure cover smaller ranges of X/D_h and Z/D_h values, where X represents the streamwise distance along the test surface, Z represents the spanwise distance along the test surface, and D_h is the channel hydraulic diameter. A comparison of the data in Fig. 7.21a,b shows that the Nu/Nu_0 ratio changes due to three-dimensional conduction are most apparent on the top of the rib segment, and on the flat base regions immediately adjacent to the rib segment. Such three-dimensional conduction effects are limited, in part, because of the high-quality construction and performance of the heated test surface, within which conduction is one-dimensional over most of the volume [7.57].

The Nu/Nu_0 data in Fig. 7.21a are obtained by assuming that all of the heat flux into the rib segment leaves entirely from the top of the rib (with none leaving

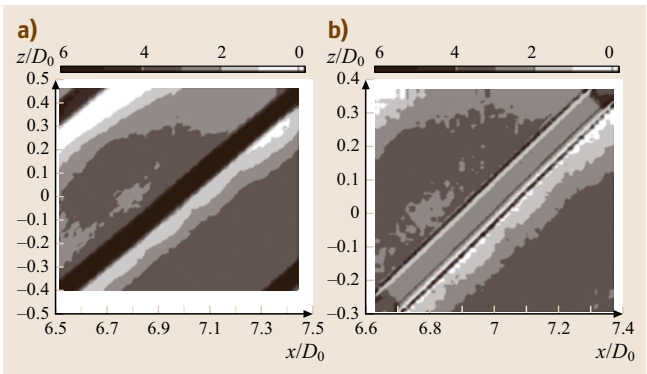

Fig. 7.21a,b Local Nusselt number ratio Nu/Nu_0 distribution along the rib turbulator test surface for $Re_H = 17\,000$ and $T_{oi}/T_w = 0.94$ [7.57]. **(a)** With constant surface heat flux and no surface conduction analysis applied. **(b)** With variable surface heat flux and surface conduction analysis applied

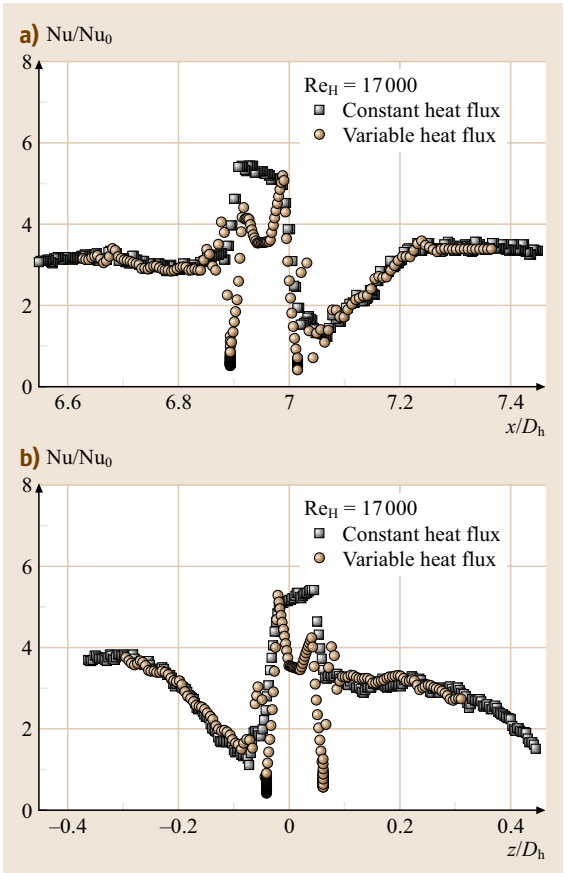

Fig. 7.22a,b Variable surface heat flux, local Nusselt number ratios Nu/Nu_0 along the rib turbulator test surface for a Reynolds number $Re_H = 17\,000$ and $T_{oi}/T_w = 0.94$. Data are given for constant surface heat flux (no surface conduction analysis) and for variable surface heat flux (with surface conduction analysis) [7.57]. **(a)** At constant $z/D_h = 0.0$ as x/D_h varies. **(b)** At constant $x/D_h = 7.0$ as z/D_h varies

from the sides). When three-dimensional conduction is present and a portion of the heat transfer leaves through the vertical sides of the rib, the surface Nu/Nu_0 distribution in Fig. 7.21b is produced. As before, the darker diagonal regions with relatively high Nu/Nu_0 ratios are again present along the tops of the ribs in this figure. Relative to constant heat flux values in Fig. 7.21a, Nusselt number ratios in Fig. 7.21b are then lower in the middle part of the rib top, with higher Nu/Nu_0 values near the upstream and downstream edges of the rib top. Nusselt number ratios on the flat surfaces just adjacent the ribs are also lowered in corners and then increased (compared to constant heat flux values) along lines that are approximately parallel to the rib segment [7.57].

The effects of three-dimensional conduction within and along the test surface are further illustrated by the results presented in Fig. 7.22a,b [7.57]. In both cases, local Nusselt number ratios Nu/Nu_0 for constant surface heat flux (no surface conduction analysis) and for variable surface heat flux (with surface conduction analysis) are presented for a Reynolds number Re_H of 17 000 and T_{oi}/T_w of 0.94. In the first of these figures, local Nu/Nu_0 data are given as they vary with X/D_h for constant $Z/D_h = 0$. In the second of these figures, Nu/Nu_0 data are given as they vary with Z/D_h for constant $X/D_h = 7.0$. Both figures show variable heat flux Nu/Nu_0 ratios that are significantly lower than the constant heat flux values in the central part of the rib. As mentioned, this is partially due to heat transfer from the sides of the ribs, which also causes local Nu/Nu_0 increases, determined with a variable heat flux thermal boundary condition, to be higher than values measured with constant heat flux, near the edges of the rib top. Other variations of importance in Figs. 7.22a and 7.22b are present on the flat surfaces near the edges of the ribs, where variable flux Nu/Nu_0 values are locally lower than constant flux Nu/Nu_0 values over very small areas [7.57]. As such, these results illustrate the usefulness of infrared thermography to obtain high-quality spatially resolved surface temperature data for use as thermal boundary-condition information in numerical prediction codes.

7.2.11 Summary and Conclusions

Results from several recent investigations [7.49, 51, 52, 57] have been presented to illustrate the variety of measurement environments where infrared thermography is employed to measure spatially resolved quantities over surfaces of interest. In one of these studies, measurements were made on the surface of a therapeutic, biomedical patch, where the quantity of interest is time-varying spatially resolved surface temperature. For the other situations, the measured temperature distributions are used to deduce other quantities such as surface Nusselt numbers on the surface of a swirl chamber [7.49], surface adiabatic film cooling effectiveness downstream of shaped film cooling holes [7.52], surface heat flux reduction ratio downstream of two rows of film cooling holes placed on an airfoil leading-edge model [7.51], or thermal boundary-condition information for numerical predictions of heat transfer characteristics on the surface of a passage with an array of rib turbulators [7.57]. The corresponding results illustrate the excellent accuracy and spatial resolution obtained with infrared imaging, and the other measurement techniques employed in each particular investigation.

To achieve high accuracy, in situ calibration procedures are required. In situ calibration procedures, like those described by *Sargent* et al. [7.44], are now widely used throughout the worldwide engineering community. With this approach, the camera, imaging, and data acquisition systems are all calibrated together in place within the experimental facility as the infrared measurements are obtained, using simultaneous, separate and independent means to measure surface temperatures. Infrared thermography then gives spatially resolved surface temperature distributions non-intrusively, even when large gradients of surface temperature are present. This can be done with high levels of accuracy and resolution, provided the infrared imaging system and acquisition procedures are properly calibrated, and the nuances of camera behavior and infrared imaging are properly included within the measurement procedures.

7.3 Temperature Measurement via Absorption, Light Scattering and Laser-Induced Fluorescence

Temperature distributions are of major interest in the description of reactive and nonreactive gaseous flow systems, where they play a crucial role in chemistry (reaction rates, equilibrium state) and physics (heat transfer, fluid dynamics, droplet evaporation). Since the first development of lasers in the 1960s, laser spectroscopy has become an important tool in fundamental and applied research in natural sciences such as physics,

chemistry, biology and medicine. The unique properties of laser light enable selective and quantitative probing of many physical and chemical parameters with high temporal and spatial resolution, and the optical nature of laser techniques allows access to enclosed systems with minimum perturbation of the system under study. Laser techniques have therefore found broad application in fluid mechanics research. Here, they allow the remote measurement of physical (pressure, temperature), chemical (species composition) and gas dynamical (flow velocities, turbulence structures) properties. A number of fundamentally different laser-based techniques have been developed and applied for temperature measurements in gas-phase flows. Detailed discussions can be found in the review articles of *Stricker* [7.66] and *Laurendeau* [7.67]. Thermometry principally relies either on the temperature dependence of the total number density (e.g., Rayleigh scattering, spontaneous Raman scattering) or the temperature dependence of the population of different rotational, vibrational, or electronic states of atomic or molecular probes [e.g., spontaneous Raman scattering, laser-induced fluorescence (LIF), or coherent anti-Stokes Raman scattering (CARS)]. However, there is to date no versatile, accurate, and robust technique that can be applied to a wide range of experimental conditions. The selection of a specific method depends on the actual problem. The following paragraphs will therefore present different approaches to laser-based temperature measurements.

7.3.1 Overview

CARS thermometry typically provides the highest accuracy, but it allows pointwise measurements only. It will be briefly explained in Sect. 7.3.4. The other techniques can in principle be used for imaging. Rayleigh scattering (Sect. 7.3.2) provides relatively strong signals that can be used to determine temperature as long as the local gas composition, and hence the local effective Rayleigh scattering cross-section, is known [7.68]. In many practical situations, however, Rayleigh thermometry suffers from strong elastic scattering off surfaces and particles; under these conditions filtered Rayleigh scattering [7.69–71] has been successfully used to separate surface scattering from the Doppler-broadened gas-phase signal. This requires stable narrow-band lasers that coincide with narrow molecular or atomic absorption lines used as notch filters. Spontaneous Raman scattering (Sect. 7.3.2) is frequently used for temperature evaluation in one-dimensional, resolved multispecies measurements [7.72]. It is typically too weak for two-dimensional imaging. It has, however, been demonstrated for instantaneous concentration imaging with long-pulse flash-lamp-pulsed dye lasers as high-energy light sources [7.73]. Laser-induced fluorescence (Sect. 7.3.3) provides strong signals and has frequently been used for pointwise and imaging thermometry either with species that naturally occur within the gas mixture or tracers added to the flow. While point measurements are based on probing several ground states (*multi-line* thermometry), instantaneous imaging measurements typically rely on quasi-simultaneous excitation at two wavelengths for temperature evaluation (*two-line* or *two-color* thermometry). In special cases where the concentration of the fluorescing species is invariant in space and time the fluorescence intensity can be used directly for temperature measurements (*single-line* thermometry). Absorption spectroscopy (Sect. 7.3.3) has been widely applied for temperature measurements using tunable diode lasers in the infrared wavelength region. While all these techniques access local temperatures, absorption techniques necessarily accumulate information along the line of sight of the laser path through the measurement volume. In homogeneous media signal interpretation from two or multiple lines or the evaluation of line-shapes is straight forward. In systems with strong concentration and temperature inhomogeneities within the interaction path results must be critically interpreted. Spatially resolved measurements are possible via multipath absorption tomography.

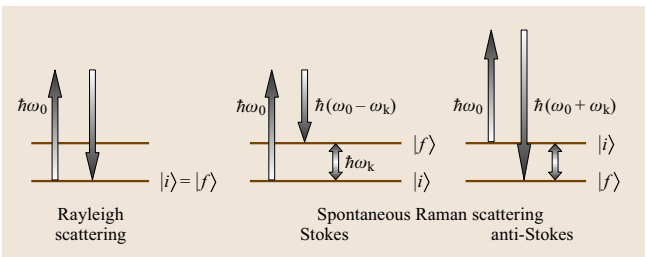

Fig. 7.23 Energy-level diagram of Rayleigh and spontaneous Raman scattering

7.3.2 Non-Resonant Techniques

Physical Background of Rayleigh and Spontaneous Raman Scattering

If a photon of energy $\hbar\omega_0$ that is non-resonant with any allowed single- or multiphoton transition interacts with a molecule with a certain probability, elastic or inelastic light scattering occurs. This process is sketched in Fig. 7.23. The more probable elastic scattering process

is termed *Rayleigh* scattering whereas the much weaker inelastic process is called spontaneous *Raman* scattering. After a Rayleigh scattering process the molecule returns to its original quantum state. In contrast, Raman scattering is associated with a net energy exchange between photon and molecule. The energy transfer might have increased or decreased the rotational (denoted by J) and/or vibrational quantum state (denoted by v) of the molecule. Due to energy conservation scattered Raman photons contain correspondingly decreased or increased energy $\hbar(\omega_0 \mp \omega_k)$ with $\hbar\omega_k$ being the energy difference between the initial $|i\rangle$ and final $|f\rangle$ quantum states involved in the process ($|i\rangle$ and $|f\rangle$ denote wavefunctions and are solutions of the corresponding Schrödinger equation). In analogy to the postulate of *Stokes* [7.74] that fluorescence is shifted towards longer wavelengths relative to the exciting wavelength, red-shifted Raman scattered photons $\hbar(\omega_0 - \omega_k)$ are termed *Stokes* lines and blue-shifted photons $\hbar(\omega_0 + \omega_k)$ *anti-Stokes* lines.

In a semiclassical view where only molecules but not the incident light are treated as quantum objects, Rayleigh and Raman scattering result from a dipole moment induced by the incident electromagnetic field. When a molecule is exposed to an alternating monochromatic electric field the resulting forces push electrons and nuclei back and forth. As a consequence the molecular system behaves analogously to an oscillating dipole. The frequency ω_0 of the alternating electric field and the oscillating dipole frequency are equal and in phase. According to the laws of electrodynamics, the molecule emits light of frequency ω_0, giving rise to Rayleigh scattering.

The flexibility of this forced intramolecular motion depends on the chemical species, temperature and quantum state. It is expressed by the polarizability tensor $\boldsymbol{\alpha}$, which is second rank. The internal degrees of freedom such as rotation or vibration modulate the polarizability. As a consequence, the induced dipole moment oscillates additionally on side bands $\omega = \omega_0 \mp \omega_k$ but with an arbitrary phase difference to the incident radiation. Herein, ω_k denotes a discrete frequency characterizing the internal motion.

For a monochromatic electromagnetic field, as provided by a laser beam, $\boldsymbol{E} = \boldsymbol{E}_0 \cos\omega_0 t$, the linear induced dipole moment can be expressed by

$$\boldsymbol{p}^{(1)} = \boldsymbol{\alpha} \cdot \boldsymbol{E} \,. \tag{7.4}$$

The aforementioned variation of the polarizability tensor $\boldsymbol{\alpha}$ with internal motions such as discrete molecular vibrations can be expanded in a Taylor series. For the example of a normal vibration k with its coordinate Q_k and in the limit of the electrical harmonic approximation that neglects powers higher than the first, the polarizability tensor may be expressed by

$$\boldsymbol{\alpha}_k = \boldsymbol{\alpha}_0 + \boldsymbol{\alpha}'_k Q_k \,. \tag{7.5}$$

The components of the new tensor $\boldsymbol{\alpha}'_k$ consist of the derivatives of the tensor components $(\alpha_{ij})_0$ with respect to the normal coordinate Q_k : $(\alpha'_{ij})_k = \left(\partial\alpha_{ij}/\partial Q_k\right)_0$. For harmonic motion the normal coordinate can be expressed by $Q_k(t) = Q_{k_0} \cos\omega_k t$, where Q_{k_0} denotes the normal coordinates amplitude. By inserting $Q_k(t)$ into (7.5) the time-dependent polarizability tensor reads

$$\boldsymbol{\alpha}_k = \boldsymbol{\alpha}_0 + \boldsymbol{\alpha}'_k Q_{k_0} \cos(\omega_k t) \,. \tag{7.6}$$

Equation (7.4) can be reformulated by using (7.6) and one finally obtains

$$\boldsymbol{p}^{(1)} = \boldsymbol{\alpha}_0 \boldsymbol{E}_0 \cos\omega_0 t + \frac{1}{2}\boldsymbol{\alpha}'_k \boldsymbol{E}_0 Q_{k_0} \cos(\omega_0 - \omega_k)t + \frac{1}{2}\boldsymbol{\alpha}'_k \boldsymbol{E}_0 Q_{k_0} \cos(\omega_0 + \omega_k)t \,. \tag{7.7}$$

The first term in (7.7) defines Rayleigh scattering. The condition to observe Rayleigh scattering is that the polarizability tensor $\boldsymbol{\alpha}_0$ is nonzero. In practice this is fulfilled for any molecule. The second and third term in (7.7) define Stokes and anti-Stokes Raman scattering, respectively. For Raman activity the derivative of the polarizability with respect to the normal coordinate $\boldsymbol{\alpha}'_k$ must be nonzero at the equilibrium position.

To derive an expression for the individual intensities of Rayleigh, Stokes, and anti-Stokes Raman scattering, the quantum-mechanical transition moments $\Phi(\alpha)$ must be calculated for a specific experimental arrangement. These transition moments replace $\boldsymbol{\alpha}$ in (7.4). In the following cartesian coordinates are applied and it is assumed that the incident monochromatic electromagnetic radiation is linearly polarized along the z-axis ($E_{0,x} = 0$, $E_{0,y} = 0$, $E_{0,z} \neq 0$) and is propagating along

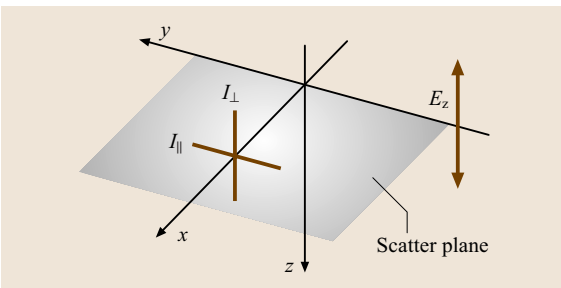

Fig. 7.24 Specific geometrical arrangement for Raman and Rayleigh scattering

Table 7.2 Space-averaged components of the transition moments for Rayleigh and ro-vibronic Raman scattering. The factor K_v is given by either $K_v = (v+1)\frac{h}{4\pi(\omega_0-\omega_k)}$ for Stokes transitions or by $K_v = v\frac{h}{4\pi(\omega_0+\omega_k)}$ for anti-Stokes transitions with v being the vibrational quantum number. The Placzek–Teller coefficients b_{J_f,J_i} are listed in [7.75]

Process	Branch	ΔV	ΔJ	$\overline{\langle f\|\alpha_{zz}\|i\rangle^2} + \overline{\langle f\|\alpha_{yz}\|i\rangle^2}$
Rayleigh		0	0	$(a)_0^2 + \frac{7}{45}b_{J,J}(\gamma)_0^2$
Rot.–vib. Raman	O	±1	−2	$K_v\frac{7}{45}b_{J-2,J}(\gamma')_0^2$
Rot.–vib. Raman	Q	±1	0	$K_v\left[(a')_0^2 + \frac{7}{45}b_{J,J}(\gamma')_0^2\right]$
Rot.–vib. Raman	S	±1	+2	$K_v\frac{7}{45}b_{J,J+2}(\gamma')_0^2$

the y-axis (Fig. 7.24). Detection takes place along the x-axis perpendicularly to the excitation light propagation ($\theta = \frac{\pi}{2}$). In this specific arrangement the scatter plane is spanned by the x and y axes. In space-fixed coordinates the polarizability tensor exhibits nonzero off-trace components. Rayleigh- and Raman-scattered light following the oscillation of an induced dipole moment therefore consists of two polarization components that are aligned perpendicular and parallel to the scattering plane (*depolarization*). Consequently, only two transition moments must be considered. For Rayleigh scattering, where strictly no net energy exchange between molecule and radiation takes place, the initial and final state are equal, whereas the initial and final states are different for Raman scattering. The transition moment relevant for Rayleigh and Raman scattering in the arrangement depicted in Fig. 7.24 is expressed by

$$\Phi(\alpha) = \langle f|\alpha_{zz}|i\rangle^2 + \langle f|\alpha_{yz}|i\rangle^2 \,, \tag{7.8}$$

where α_{zz} and α_{yz} are either the tensor elements of the polarizability $\boldsymbol{\alpha}_0$ (Rayleigh) or rather the derivative of the polarizability with respect to the normal coordinate of the intermolecular motion $\boldsymbol{\alpha}'_k$ (Raman). The two components of the induced dipole moment for the transition $f \leftarrow i$ can be accordingly expressed by

$$\begin{aligned} p^{(1)}_{f\leftarrow i,y} &= \langle f|\alpha_{yz}|i\rangle E_{0,z} \,, \\ p^{(1)}_{f\leftarrow i,z} &= \langle f|\alpha_{zz}|i\rangle E_{0,z} \,. \end{aligned} \tag{7.9}$$

Following the laws of electrodynamics, the power of radiation emitted by an oscillating dipole with oscillation frequency ω can be expressed, with $T_{\perp,\parallel}$ being the polarization-dependent transmissivity of the detection optics, by:

$$I(\theta, T_{\perp,\parallel})_{f\leftarrow i} = T_{\perp,\parallel}\frac{c}{32\varepsilon_0\pi^2}\omega^4\left(p^{(1)}_{f\leftarrow i}\right)^2 \sin^2\theta \,. \tag{7.10}$$

The angle θ between exciting radiation and detection direction in the specific arrangement considered here is $\pi/2$. Consequently, $\sin^2\theta = 1$. For Rayleigh scattering the oscillation frequency is given by $\omega = \omega_0$. For Stokes and anti-Stokes Raman scattering the frequencies are correspondingly $\omega = \omega_0 \mp \omega_k$. Exploiting (7.9), the polarization-dependent scattering intensities read

$$\begin{aligned} I_\perp(\theta, T_\perp)_{f\leftarrow i} &= T_\perp\frac{c}{32\varepsilon_0\pi^2}\omega^4\langle f|\alpha_{zz}|i\rangle^2|E_{0,z}|^2 \,, \\ I_\parallel(\theta, T_\parallel)_{f\leftarrow i} &= T_\parallel\frac{c}{32\varepsilon_0\pi^2}\omega^4\langle f|\alpha_{yz}|i\rangle^2|E_{0,z}|^2 \,. \end{aligned} \tag{7.11}$$

Assuming that $T_\perp = T_\parallel = 1$, the total intensity from a single spatially fixed molecule is given by the sum of both polarization components

$$\begin{aligned} I(\theta)_{f\leftarrow i} = &\frac{c}{32\varepsilon_0\pi^2}\omega^4 \\ &\times\left(\langle f|\alpha_{zz}|i\rangle^2 + \langle f|\alpha_{yz}|i\rangle^2\right)|E_{0,z}|^2 \,. \end{aligned} \tag{7.12}$$

For an ensemble consisting of $N_{\mathrm{C,tot}}$ molecules of species C with $N_{v,J}$ being in a specific initial quantum state $|i\rangle = |v, J\rangle$, the Boltzmann fraction relates these two numbers by $f_{v,J}(T) = N_{v,J}/N_{\mathrm{C,tot}}$ with T being the temperature. Because molecule movements in a low-density gas are random, in an actual measurement space-averaged transition moments (subsequently denoted by overbars) need to be considered. The space averages of the squares of the transition moments may be expressed in terms of the invariants of the derived polarizability tensor components associated with the k-th normal mode. Commonly, space invariants are expressed by $(a)_0$ and $(\gamma)_0$ for Rayleigh scattering, and by $(a')_0$ and $(\gamma')_0$ for Raman scattering. Table 7.2 summarizes the space-averaged components of the transition moments for Rayleigh and Raman scattering.

The Rayleigh/Raman scattering intensity then reads

$$\begin{aligned} I(\theta)_{f\leftarrow i} = &\frac{c}{32\varepsilon_0\pi^2}\omega^4\left(\overline{\langle f|\alpha_{zz}|i\rangle^2} + \overline{\langle f|\alpha_{yz}|i\rangle^2}\right) \\ &\times|E_{0,z}|^2 f_{v,J}(T)N_{\mathrm{C,tot}} \,. \end{aligned} \tag{7.13}$$

This expression can be reformulated by introducing a temperature-dependent differential cross-section $\partial\sigma/\partial\Omega(T)$ by

$$\frac{\partial\sigma}{\partial\Omega}(T) = \frac{c}{32\varepsilon_0\pi^2}\omega^4 \times \left(\overline{\langle f|\alpha_{zz}|i\rangle^2} + \overline{\langle f|\alpha_{yz}|i\rangle^2}\right) f_{v,J}(T)\,. \tag{7.14}$$

An actually measured Rayleigh or Raman signal is due to the number of photons S collected from a specific probe volume. By using (7.13) and (7.14) S is given by

$$S_{\mathrm{C},f\leftarrow i}(\theta) = \frac{I(\theta)}{\hbar\omega} = \frac{1}{\hbar\omega}\frac{\partial\sigma}{\partial\Omega}|E_{0,z}|^2 N_{\mathrm{C,tot}}\Omega\eta\,. \tag{7.15}$$

where Ω is the solid angle of the collection optics and η is the overall detection efficiency (transmissivity of optics, quantum efficiency of detector). Note that both factors should be derived from calibration measurements.

For a reliable simulation of Raman signals it is imperative to calculate the transition frequency $\omega = \omega_0 \mp \omega_k$ correctly. In general, anharmonic corrections and deviations from the rigid-rotator assumption need to be applied. Depending on the molecule under consideration this can already be problematic especially for other than diatomic molecules [7.76].

The Boltzmann fraction $f_{v,J}(T)$ can be calculated as a function of the term values E_i (in wavenumbers) and degeneracy factors g_i by

$$f_{v,J}(T) = \frac{g_i \exp\left(\frac{hcE_i(v,J)}{kT}\right)}{\sum_i g_i \exp\left(\frac{hcE_i(v,J)}{kT}\right)} = \frac{g_i}{Z(T)}\exp\left(\frac{hcE_i(v,J)}{kT}\right) \tag{7.16}$$

with $Z(T)$ being the temperature-dependent partition function. This implies the use of correct term values and once again the need for anharmonic and non-rigidity corrections. The space-averaged transition moments so far have been discussed in the framework of the electrical harmonic approximation (compare (7.5)). For high temperatures, such as in chemically reacting flows, electrical anharmonicities [higher orders in (7.5)] need to be considered as well.

The temperature dependence of the measured Rayleigh and Raman intensities in (7.15) is given through the Boltzmann fraction $f_{v,J}(T)$ and the number density $N_{\mathrm{C,tot}}(T, p)$. The latter can be expressed in terms of the total molar gas number density n, the mole fraction x_c of species C and the avogadro number $N_A : N_{\mathrm{C,tot}} = x_c n N_A$. By assuming the validity of the ideal gas law, the total number density $N = nN_A$ is a function of pressure p and temperature T. In the following sections we discuss how these temperature dependencies can be exploited for thermometry. Note, that in contrast to thermometry based on fluorescence, the Rayleigh and Raman scattering processes are not disturbed by intermolecular collisions.

Thermometry by Rayleigh Scattering

Rayleigh-scattered light is in phase with the incident radiation. This can cause interference by scattering from different molecules. However, this is prevented in the gases considered here due to the random motion of the molecules. Furthermore, in Rayleigh scattering all chemical species contained in a finite-sized probe volume give rise to a measured signal. Therefore, contributions of each chemical species C as expressed in (7.15) sum up to a total Rayleigh-scattering signal, resulting in

$$S_{\mathrm{ray}}(\theta) = \frac{1}{\hbar\omega}\left(\frac{\partial\sigma}{\partial\Omega}\right)_{\mathrm{ray}}|E_{0,z}|^2 N\Omega\eta\,. \tag{7.17}$$

Here, an effective Rayleigh cross-section $(\partial\sigma/\partial\Omega)_{\mathrm{ray}} = \sum_{\mathrm{C}} x_{\mathrm{C}}\,(\partial\sigma/\partial\Omega)_{\mathrm{C,ray}}$ is used. In general, $(\partial\sigma/\partial\Omega)_{\mathrm{C,ray}}$ is approximately independent of temperature. Then, as is obvious from (7.17), Rayleigh scattering can be used to assess the total number densities N if the gas composition is known. Therefore, for spatially-homogeneous (measured) pressure, the temperature can be derived via the ideal gas law.

Rayleigh thermometry is a technique relying in many practical applications on single laser shots [7.77]. Thereby a high temporal resolution much shorter than typical Kolmogorov time scales in turbulent (reactive) flows can be accessed. With relatively little experimental effort Rayleigh scattering can be applied in an imaging setup. A sketch of a typical setup is shown in Fig. 7.25.

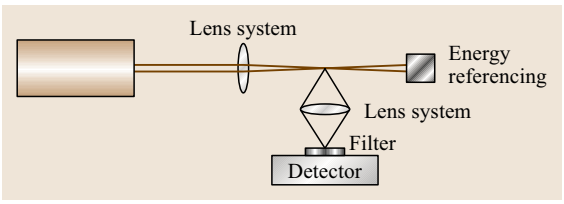

Fig. 7.25 Schematic of the experimental setup for Rayleigh scattering

Rayleigh thermometry has therefore been widely applied to turbulent systems, e.g., in turbulent flames [7.68, 78] or internal combustion engines [7.79]. Inferring number densities from scattering data, however, requires information about local effective Rayleigh cross-sections and therefore the local gas composition, which is usually unavailable in inhomogeneously mixed or reactive systems [7.80]. In combustion, special fuel blends have been proposed that provide similar total cross-sections for unburned and burned gases [7.68, 81], enabling Rayleigh thermometry even in turbulent combustion systems. Alternatively, Raman scattering can be applied simultaneously with Rayleigh scattering to measure the gas composition [7.72]. This is, however, limited spatially to one dimension [7.82].

Rayleigh thermometry suffers from problems with background scattering (e.g., off walls or windows); in the presence of particles such as soot in flames; this technique is therefore not feasible at all. Here, a filtered Rayleigh-scattering technique has been applied [7.69–71]. This approach makes use of the fact that gas-phase molecules has a wider Doppler width due to their thermal motion (≈ 0.1–$0.3\,\mathrm{cm}^{-1}$) than scattering off surfaces (walls, particles, droplets). If a single-longitudinal-mode laser is used, the signal of surface-scattered light can be rejected by narrow-band ($< 0.05\,\mathrm{cm}^{-1}$) filters (usually molecular filters like iodine or atomic vapor filters such as mercury contained in quartz cells). Increasing temperature causes a larger Doppler width of the Rayleigh-scattered light originating from the gas phase. This line broadening causes an increasing signal, bypassing the narrow-band filter. The principle of filtered Rayleigh scattering thermometry is shown in Fig. 7.26. Exact control of the laser wavelength, spectral profile, absorption profile of the molecular or atomic line filter, and knowledge of line broadening is required.

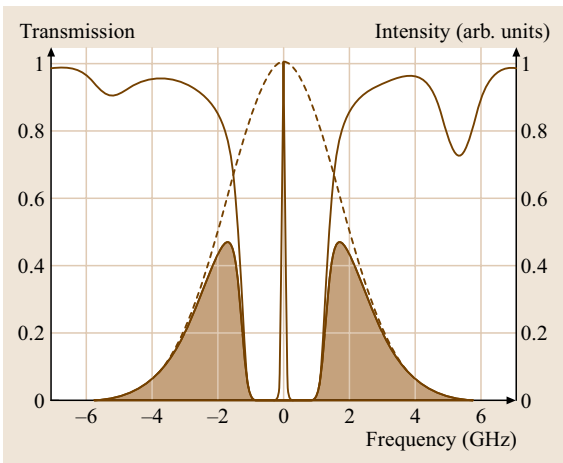

Fig. 7.26 Molecular line-shape of Rayleigh-scattered light at elevated temperature (*dashed line*), transmission profile of an atomic vapor such as mercury (*solid line*) and spectral laser emission (peak at 0 GHz). The spectral overlap of the atomic notch and Doppler-broadened Rayleigh profiles result in the spectral wings transmitted to the detector (*hatched area*) (after [7.84])

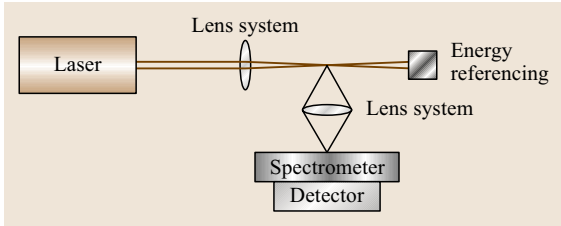

Fig. 7.27 Schematic of the experimental setup for Raman scattering

Thermometry by Raman Scattering

A sketch of a Raman spectrometer is shown in Fig. 7.27.

Each chemical species exhibits a specific red and blue shift (Stokes and anti-Stokes lines) according to the energy difference $\hbar\omega_k$ between the initial and final states involved to the process. Table 7.3 summarizes averaged relative normalized differential Raman cross-sections for Q-branches $[(\partial\sigma/\partial\Omega)_Q\,(T = 300\,\mathrm{K})]$ and Raman frequency shifts for combustion-related molecules. Averaged differential Raman cross-sections

Table 7.3 Raman shifts and averaged normalized differential Raman cross-sections for the Q-branch of some combustion-related molecules at room temperature. The absolute Raman cross-section of the Q-branch of nitrogen is $(5.05 \pm 0.1) \times 10^{-48}\,(\omega_0/2\pi c - 2331\,\mathrm{cm}^{-1})\ \mathrm{cm}^6/sr$. Data are taken from [7.83]

Molecule	Raman shift $\omega_k/2\pi c$ (cm^{-1})	$(\partial\sigma/\partial\Omega)_Q$ ($T = 300$ K)
CO_2 (ν_2)	1285.0	0.75
CO_2 (ν_1)	1388.0	1.13
O_2	1555.0	1.04
CO	2143.0	0.93
N_2	2331.0	1.0
CH_4 (ν_1)	2914.0	8.55
CH_4 (ν_2)	3017.0	5.7
H_2O	3652.0	3.51
H_2	4155.2	3.86

scale nonlinearly with temperature. For molecular hydrogen Fig. 7.28 shows the theoretical temperature dependence of the differential Q-branch cross-sections normalized to its value at 300 K. Depending on the theoretical approach [7.76], the temperature dependence, especially at temperatures exceeding 1000 K, can differ by a few percent, depending on the molecule.

In contrast to pure Rayleigh scattering, signals from different chemical species C show species-specific Raman frequency shifts and therefore must be spectrally dispersed before detection. The advantage of Raman thermometry is that dispersed Raman spectra contain all the necessary information to deduce the gas temperature. This is in contrast to Rayleigh thermometry or laser-induced fluorescence (LIF) schemes, where additional information on gas composition, and collisional energy-transfer pathways in the case of LIF, is required for a thorough analysis. Therefore, despite the rather small scattering cross-sections, which need to be overcome by high excitation laser photon fluxes and low-noise detection components, Raman thermometry can be an important alternative. Note that, in addition to temperature, the gas composition can be evaluated as well (simultaneous Raman/Rayleigh scattering [7.72,82, 85]). Raman scattering is therefore the only multiscalar diagnostic based on a single excitation frequency.

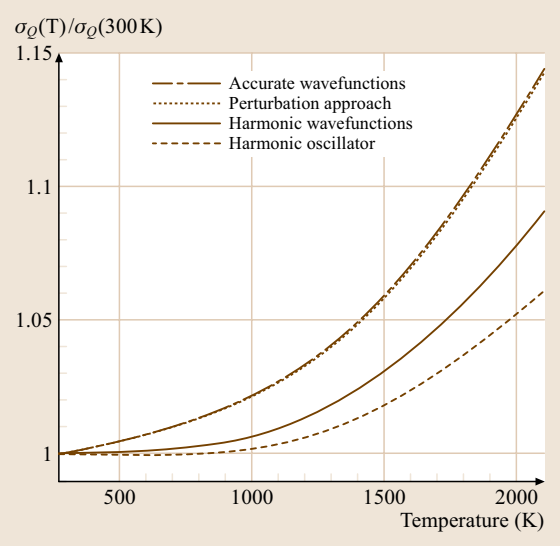

Fig. 7.28 Relative differential Raman cross-sections of molecular hydrogen as a function of temperature. Dependent on the theoretical description for temperatures exceeding 1000 K the differences between the calculated cross-sections differ by a few percent (after [7.76])

Local temperatures can be extracted from Raman spectra in different ways. For the case of high spectral dispersion, single rotational or ro-vibronic lines might be resolved. Raman spectra can be simulated and fitted to the measured spectra [7.76, 82]. However, in addition to (7.15), line widths must be considered as well. Raman lines might be pressure and Doppler broadened. In addition, the limited spectral resolution of the spectrometer broadens the measured lines. Therefore, each allowed transition needs to be convoluted with an effective line-shape and a spectrum is received from the superposition of all relevant allowed transitions. Figure 7.29 shows schematically the ro-vibronic N_2 Raman bands at various temperatures. In this example the effective line width is broad compared to the spectral separation of adjacent transitions. This leads to an overlap of ro-vibronic Raman lines, resulting in a single Raman band up to approximately 400 K and additional hot bands at temperatures above 500 K. It is obvious that Raman bands and spectral intensities are strongly temperature dependent.

A second way to extract temperatures from Raman scattering is to determine the number densities of each chemical component present in the probe volume. To do this it is assumed that the gas composition is comprised of only Raman-active species at sufficiently high concentrations to allow accurate detection and Stokes shifts into spectral regions that are actually monitored. Then the number density of all chemical components can be added to find the overall number density in the probe volume under consideration. With the validity of the ideal gas law assumed, as in Rayleigh thermometry, the total number density in connection with the (measured) pressure can be used to determine a local temperature.

The third way to determine temperatures from Raman scattering is to perform measurements of both Stokes- and anti-Stokes-shifted Raman lines (or bands). In the limit of the harmonic approximation and identical degeneracy factors for both quantum states, the measured ratio of Stokes and anti-Stokes lines is given by

$$\frac{S_{\text{Stokes}}}{S_{\text{anti-Stokes}}} = \left(\frac{\omega_0 - \omega_k}{\omega_0 + \omega_k}\right)^3 \exp\left(\frac{\hbar c \omega_k}{kT}\right) . \qquad (7.18)$$

The intensity ratio must be a value which can be measured with sufficient signal-to-noise ratio. This requires a sufficiently high population in the excited state from which anti-Stokes Raman scattering can take place. Near room temperature Raman lines shifted in the range 0–500 cm^{-1} are useful, whereas at around 1000 K spectral shifts up to 2000 cm^{-1} should be used.

Practical Considerations

In general Rayleigh scattering can be applied at single points [zero-dimensional (0-D)], along lines [one-dimensional (1-D)], or in two-dimensional (2-D) planes. By combining at least two parallel-orientated 2-D planes, quasi-three-dimensional applications are possible as well. As depicted in Fig. 7.25, for Rayleigh thermometry an exciting light source (most commonly a laser), a detector and some optical components such as a bandpass filter in front of the detector and lens systems are needed. In the case of 0-D and 1-D applications the laser might be focussed simply by a long-focal-length spherical lens, in the case of 2-D applications the laser is formed into a light sheet by appropriate spherical and cylindrical lenses.

Raman scattering experiments can also be performed in 0-D, 1-D or 2-D. Two-dimensional applications, however, are only feasible for flows containing just a few main components, as each component needs an individual detector equipped with a suitable bandpass filter. For the general case, where many components occur in the flow such as hydrocarbon/air flames, Raman scattering can be applied in practice only up to 1-D. In this case along the probe volume Raman bands stemming from the various chemical components are spectrally dispersed before detection (Fig. 7.27).

In the following some practical aspects on hardware components and issues related to calibration are discussed. However, this paragraph is far from complete and for more-detailed information the reader is referred to the literature and textbooks such as [7.72, 76, 86].

Laser System. Many fluid-mechanical problems are characterized by turbulence; hence, exposure times of single temperature measurements should be sufficiently short to monitor frozen states of the turbulent flow under investigation. The shortest time scales in turbulent flows are characterized by Kolmogorov scales [7.87]. Taking an industrial-type nozzle for combustion applications as an example [7.88], Kolmogorov time scales can be estimated assuming homogeneous isotropic turbulence. Typical Kolmogorov time scales are on the order of few microseconds. Consequently, single temperature measurements should resolve at least one microsecond. In practice, this requirement presupposes the usage of pulsed lasers in the sub-microsecond regime. Due to their high photon fluxes, reliability, and ease of operation solid-state, quality-switched lasers are increasingly used for Rayleigh or Raman thermometry, replacing flashlamp-pumped dye [7.89] or excimer lasers [7.90, 91]. Among the class of solid-state lasers, the Nd:YAG laser is currently the workhorse in many laboratories. Typical specifications are pulse widths of 10 ns, repetition rates ranging from 10 to 100 Hz, and pulse energies in the fundamental at 1064 nm up to 2.5 J. The frequency conversion up to the fourth harmonic at 266 nm is easily possible due to the high peak intensities. Generally spoken, highest pulse energies as possible are favored but in practice optical breakdown phenomena set a limit. Optical breakdown occurs by absorption processes most often at remaining dust particles that exist as trace components in many flows. During a breakdown high light intensities are emitted that can damage photodetectors such as image intensifiers or CCD devices. To lower the probability of optical breakdown, pulse stretchers are used to lower the intensity but maintain a high pulse energy [7.72].

The choice of the excitation wavelength (laser emission wavelength) depends on the specific application. In general, the Rayleigh and Raman cross-sections increase nonlinearly with decreasing excitation wavelength [compare (7.14)]. However, laser-induced fluorescence interference, especially with Raman scattering, should be avoided [7.92]. As the electronic resonances of many molecules are located in the ultraviolet (UV) region [7.93, 94], the higher scattering cross-sections in the UV can be exploited only for flows consisting of specific components that are non-resonant with the excitation wavelength. In combustion research, UV excitation has been exploited for the investigation of hydrogen/air flames [7.95]. For hydrocarbon/air flames, partially oxygenized or polycyclic hydrocarbons may be formed during the oxidation process, giving rise to signals that interfere with Raman bands [7.92]. Therefore, and at the expense of decreased cross-sections, an excitation laser wavelength in the visible spectral region needs to be used. This loss can be partly compensated by higher laser pulse energies and higher detector quantum efficiencies in the visible spectral region.

Detection. Prior to detection, the signal radiation is dispersed in the case of Raman scattering, most commonly using a Czerny–Turner spectrometer, or is filtered by a narrow-bandwidth interference filter to reject spurious light in the case of Rayleigh scattering.

Due to the small Raman cross-sections, signal intensities especially in Raman thermometry are rather low. For this reason a low-noise detector, large solid angle of detection optics and high quantum efficiency are mandatory. For 0-D applications photomultiplier tubes (PMT) have been commonly used. At the exit plane of a suitable spectrometer for each chemical component

at least one PMT monitors individual species concentrations. For 1-D Raman applications a 2-D array detector is needed (space and wavelength directions). For this reason CCD detectors are commonly used. The lowest noise level combined with the highest quantum efficiency is currently delivered by backside-illuminated CCD array detectors. If high temporal resolution is required and some background luminosity is present, as is the case in flames, an additional fast shutter assembly is needed. As exemplified in [7.96], a fast mechanical shutter with exposure times on the order of 10 µs can be built from rotating slit wheels.

In the case of Rayleigh scattering, the requirements for low-noise high-quantum-efficiency detectors are less stringent compared to Raman scattering because of the much larger cross-sections. For 0-D applications PMTs are the best solution, whereas for 1-D or 2-D applications intensified CCD array detectors (ICCD) are best suited. The intensifier allows a short-gated detector, with very efficient spurious-light suppression, to be used. The filter in front of the detector might be either an interference bandpass filter, or a notch filter (Fig. 7.26) in the case of filtered Rayleigh scattering.

Calibration. Spectroscopic methods are in general not self-calibrated. Several factors such as probe volume, the solid angle of detection, transmission through optical elements, or the detector quantum efficiency depend very specifically on the individual experimental setup and may in part vary with wavelength. For this reason calibration measurements must be performed. Taking Rayleigh thermometry as an example, a measured temperature can be expressed relative to a calibration condition on the basis of (7.17) and the ideal gas law by

$$T = \frac{S_{\mathrm{ray}}}{S_{\mathrm{ray,ref}}} \frac{(\partial\sigma/\partial\Omega)_{\mathrm{ray,ref}}}{(\partial\sigma/\partial\Omega)_{\mathrm{ray}}} \frac{|E_{0,z,\mathrm{ref}}|^2}{|E_{0,z}|^2} \frac{p_{\mathrm{ref}}}{p} T_{\mathrm{ref}} \,. \tag{7.19}$$

Resolution. The spatial resolution achieved in any optical diagnostic method depends on the laser beam diameter and imaging quality of the optical components that image the probe volume onto the detector. Beam diameters can be reduced using rather short-focal-length focussing lenses and operating the laser in the TEM_{00} mode. Depending on the specific configuration, spot sizes of 200 µm or less can easily be realized. Using well-designed lenses, imaging of 50 µm spots on the detection side is possible as well. In typical experimental arrangements of single-shot Rayleigh thermometry, a probe volume size of $\approx (100\,\mu\mathrm{m})^3$ can therefore routinely be achieved. This might be not true for Raman thermometry in general, where optical breakdown often limits the laser spot diameter to values above 200 µm.

In contrast to the very high temporal resolution (sub-microsecond regime using quality-switched laser pulses), which is often below the Kolmogorov time scales for many practical turbulent flows, the length scales of the smallest structures of these flows, given by *Batchelor* [7.97], might not be resolved spatially. The situation is even worse for fluids with Schmidt numbers much larger than 1. This limited spatial resolution, although much better than typical intrusive probe techniques such as thermocouples, can act similar to a low-pass filter and may influence the measurement of local temperatures and, even worse, local temperature gradients in the case of 1-D or 2-D applications.

7.3.3 Resonant Techniques

Temperature from Absorption Measurements

Absorption spectroscopy is one of the oldest techniques for the non-intrusive investigation of gaseous media. The subject of interest in laser absorption spectroscopy (LAS) is mostly the absolute concentration or absorber density of one or more atomic or molecular species that is present in a mixture [7.98, 99]. Apart from that, LAS is able to determine simultaneously physical boundary conditions such as temperature, velocity, pressure or mass flux etc. to which the absorbers are exposed [7.100].

The basic setup of an absorption spectrometer can be described as a radiation source, which emits collimated light with an initial intensity $I_0(\nu)$ through the sample under investigation towards a radiation detector. Part of the radiation, $\mathrm{d}I(\nu)$, is absorbed by atomic or molecular constituents along each path increment $\mathrm{d}l$ in a simple one-step process. The light intensity $I(\nu)$ behind the sample is monitored to determine the total loss and is used as a quantitative measure for the number of absorbers along the beam path. The transition frequency ν at which the absorption occurs is characteristic of the absorbing substance, so that a simultaneous species identification (a spectral fingerprint) is possible. Integration of the light losses over the total absorption path l leads, under the assumption of a spatially homogenous absorber distribution and a monochromatic light source, to the Lambert–Beer equation

$$I(\nu, l) = I_0(\nu) \exp\left[-\kappa(\nu) C l\right] , \tag{7.20}$$

where C is the absorber concentration, and $\kappa'(\nu) = \kappa(\nu) C$ is the linear molar absorption coefficient [7.98].

At thermal equilibrium the fractional population $f_{v,J}(T)$ of level $i = |v, J\rangle$ with energy E_i is described by the Boltzmann equation (7.16). In an equilibrium state of particle ensemble and radiation field the upward and downward radiative transition rates must be equal and the Einstein coefficients are related by the following equation:

$$\frac{A_{21}}{B_{21}} = \frac{8\pi h \nu_{12}^3}{c^3} \,. \tag{7.21}$$

At low laser intensities the total amount ΔI absorbed at the transition frequency ν_{12} by any upward transitions from E_1 to E_2 is then described as:

$$-\Delta I(\nu_{12}) = I_0(\nu_{12}) N_1 \Delta l \frac{A_{21} c^2}{8\pi \nu_{12}^2} \,. \tag{7.22}$$

Absorption-Line Parameters: Line Strength and Shape. In order to remove its line-shape dependence, $\kappa(\nu)$ is often expressed as a product of a frequency-independent line-strength factor, S, called the integrated absorption coefficient, and a normalized line-shape function $\phi(\nu - \nu_{12})$ with the half-width γ centered at ν_{12}:

$$\kappa(\nu) = S\phi(\nu - \nu_{12}) \,; \quad \int_{-\infty}^{\infty} \phi(\nu - \nu_{12}) \mathrm{d}\nu = 1 \,;$$

$$S = \int_{-\infty}^{\infty} \kappa(\nu) \mathrm{d}\nu \,. \tag{7.23}$$

With these relations we can rewrite the Lambert–Beer relation as

$$I(\nu, l) = I_0(\nu) \exp\left[-S\phi(\nu) N_1 l\right] \tag{7.24}$$

and remove the line-shape dependence by integrating over the entire absorption line, so that the total spectral area S occupied by the absorption line reflects only the absorption strength and the number density of absorbers in the initial level E_1. In this case the relation between the Einstein coefficient for spontaneous emission, A_{21}, and S becomes, $S = (A_{21} N_1 \frac{g_2}{g_1} \nu_{12}^2) \frac{c^2}{8\pi}$ [7.101], which shows that the integrated absorption coefficient is only proportional to the absorber specific constants and the number of atoms in the initial state.

Temperature Dependencies. In any combustion-related sensor for molecular species it is important to recognize that S is a strong function of temperature. If the pressure remains constant during a temperature change the absorber density will change as T^{-1}. In addition, the fractional population $f_{v,J}$ (7.16) at the initial energy level changes as a function of temperature and energy of the probed state. A change in temperature of several hundred degrees can cause variations in the integrated absorption coefficient over two orders of magnitude. On the other hand, this strong temperature dependence can be used to measure the temperature itself by taking the ratio of the integrated absorption of at least two suitable transitions [7.100, 102].

Line shapes and Broadening. The finite lifetimes of all excited states lead to natural or radiative line broadening, which is described by a Lorentzian profile with a width γ_N. In addition, the thermal motion of the absorbers with mass M in a gas at thermal equilibrium at a temperature T causes a velocity-dependent Doppler shift in the transition frequency, resulting in a distribution of transition frequencies, which is modeled by a Gaussian line-shape function of width γ_D. Furthermore, collisional broadening is generated by frequent perturbations of the absorber through collisions with other gas molecules, which results in a shortening of the lifetime of the excited state and in a shift of the energy levels involved. This line-shape is often sufficiently described by a Lorentzian function. To take into account the effect of different collision partners separate foreign-gas and self-broadening coefficients γ_{L_i} are introduced and empirically derived expressions for the pressure and temperature dependence of the half-width are used and can be combined to give

$$\gamma_{\mathrm{Lorentz}} = \left(\gamma_{L_s} \frac{p_s}{p_{\mathrm{tot}}} + \gamma_{L_f} \frac{p_f}{p_{\mathrm{tot}}}\right) \left(\frac{T_0}{T}\right)^n \tag{7.25}$$

with T_0 a reference and T the actual temperature. p_i and p_{tot} are the partial and total pressures, respectively; n reflects the temperature dependence with kinetic gas theory yielding a power law of $n = 0.5$. Finally, at intermediate pressures, when none of the aforementioned mechanisms dominates, the experimental line-shape is described by a convolution of the Gauss and Lorentz profiles, the so-called Voigt function, which generally cannot be expressed in an analytical form. Approximations and further literature on line-shapes can be found in [7.98, 103, 104].

LAS can be applied to any absorber that has either a permanent dipole moment or an allowed electronic transition. In the first case nearly any heteronuclear molecule relevant to combustion such as H_2O, CO, CO_2, CH_4, NO, NO_2, NH_3 [7.99, 102, 105, 106] can be detected via strong ground-state rotational–vibrational transitions in the mid-infrared or via weaker overtone

and combination bands in the near-infrared (0.75–3 μm) spectral region. Even stronger electronic transitions of all atoms, ions, molecules, and free radicals important in combustion, e.g., H, O, N, O_2, NO, CH_4, CH, OH, NH_2, CH_3, HO_2 [7.98, 107, 108] are accessible in the visible (350–750 nm) and most often in the ultraviolet part (< 350 nm) of the spectrum.

Long-Path Absorption Techniques. To increase detection sensitivities in absorption measurements the path length of the sample-traversing beam must be increased. White- or Herriot-type mirror arrangements are often employed at the cost of spatial resolution. Another line-of-sight absorption technique that has emerged recently as a species-specific combustion diagnostic tool is cavity ring-down laser absorption spectroscopy (CRLAS) [7.109] to monitor reactants, intermediates and products with very high sensitivity ($< 10^{-6}$ fractional absorption). In CRLAS a laser beam is coupled into a linear cavity formed by two concave mirrors with high reflectivity (> 99.98%). The intensity decay in the cavity is given by $\mathrm{d}I/\mathrm{d}t = -ITc/L$, where L is the length of the cavity with mirrors of transmissivity T. This leads to the exponential solution $I(t) = I_0 \exp(-Ttc/L)$ with the decay constant $\tau = L/Tc$. One can define a total round-trip loss of $\Gamma = 1 - \exp(-2L/c\tau)$, since the round-trip time in the cavity is $\tau_{\mathrm{rt}} = 2L/c$ [7.109]. The intensity of the trapped light pulse is monitored in time via transmission through the output mirror on successive passes inside the cavity. Every absorption species along its multiple trips between the mirrors due to the probed species increases the overall photon decay rate of the light pulse

$$\frac{1}{\tau} = \frac{[\mathrm{T} + \Lambda + \kappa(\nu)h]\,c}{L} \tag{7.26}$$

from that of the empty resonator with τ_{rt}. In (7.26) $T + \Lambda$ are cavity losses due to mirror transmission (T), and due to nonspecific absorption and scattering (Λ). Therefore, the decay time is a quantitative measure of the absorption strength, and hence the concentration of the species inside the cavity. Because only the decay time is relevant the method also has the advantage of being insensitive to pulse-to-pulse energy fluctuations of the laser source. However, any other intensity losses should be avoided (scattering, surface reflection, bulk material absorption etc.), as they reduce the beam intensity inside the cavity and thereby the decay time.

Intermediates in hydrocarbon combustion, such as hydroxyl, methylene and methyl radicals, have been detected in laminar flames [7.110, 111] and low-pressure plasmas [7.112], respectively, using CRLAS or intracavity absorption (ICLAS) with ultraviolet light to stimulate electronic transitions. The exceptionally high signal-to-noise level in such measurements leads to very accurate, path-integrated temperature determinations with accuracies of less than 2% in atmospheric pressure flames. Using CRLAS, HCO [7.113], hydrocarbons (CH_4, CH_3), water, and CO_2 have also been detected quantitatively in their characteristic infrared spectrum around 3 μm with very high spectral resolution (0.007 cm^{-1}) in low-pressure (50 mbar) laminar methane/air flames using an optical parametric oscillator [7.114], and ICLAS has made possible the detection of CH_2 in flames [7.111]. Besides combustion diagnostics CRLAS is also increasingly being applied in other fields of physical chemistry including high-resolution spectroscopy [7.115] and chemical kinetics [7.116].

Absorption Thermometry. For temperature measurements based on the ratio of absorption strengths, the peak absorption or the integrated area of at least two absorption features of a target molecule must be known. From this data the absolute temperature can be calculated using the Boltzmann law (7.16). The technique is frequently described in the literature [7.117]. In an optical path with spatially homogeneous properties in thermal equilibrium the integrated absorbance areas a_1 and a_2 (cm^{-1}) of the two transitions

$$a_i = \int_{-\infty}^{\infty} -\ln\left(\frac{I}{I_0}\right)\mathrm{d}\nu \tag{7.27}$$

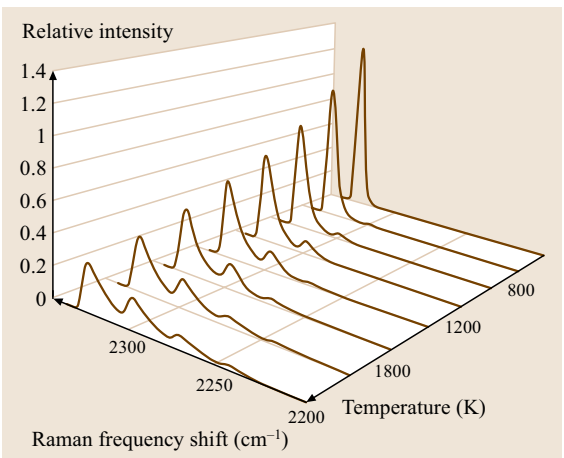

Fig. 7.29 Relative Raman scattering intensities of molecular nitrogen for different temperatures [7.86]

are measured. I and I_0 represent the transmitted and the incident light intensities, respectively. The integration is over frequency ν (cm^{-1}). Each area can be expressed as

$$a_i = S_i(T)pxl\,, \tag{7.28}$$

where x and T (in K) are the absorber mole fraction and temperature, respectively; p (in bar) is the pressure and the path length is given by l (in cm). The line strengths S_i ($\mathrm{cm}^{-2}\,\mathrm{bar}^{-1}$) can be expressed as

$$S_i(T) = S_i(T_0)\frac{T_0}{T}\frac{Z(T_0)}{Z(T)}\frac{1-\exp\left(-\frac{hc\nu_{0,i}}{k_\mathrm{B}T}\right)}{1-\exp\left(-\frac{hc\nu_{0,i}}{k_\mathrm{B}T_0}\right)} \times\exp\left[-\frac{hc}{k_\mathrm{B}}E_i''\left(\frac{1}{T}-\frac{1}{T_0}\right)\right], \tag{7.29}$$

where T_0 is a reference temperature, k_B is the Boltzmann constant, Z is the absorber's partition function, and $\nu_{0,i}$ (in cm^{-1}) and E_i'' (in cm^{-1}) are the frequency and lower-state energy of the i-th transition, respectively. The ratio R of the areas a_1/a_2 can therefore be reduced to a function of the absorber temperature T only:

$$R \equiv \frac{a_1}{a_2} = f(T) \approx \frac{S_1(T_0)}{S_2(T_0)}\exp\left[-\frac{hc}{k_\mathrm{B}}(E_1''-E_2'')\left(\frac{1}{T}-\frac{1}{T_0}\right)\right]. \tag{7.30}$$

Typically a_1 and a_2 are measured and one can derive the temperature by solving (7.30). If the two transitions are chosen in the right way as explained below the ratio R is a unique function of temperature over several 100 K, as demonstrated in Fig. 7.30.

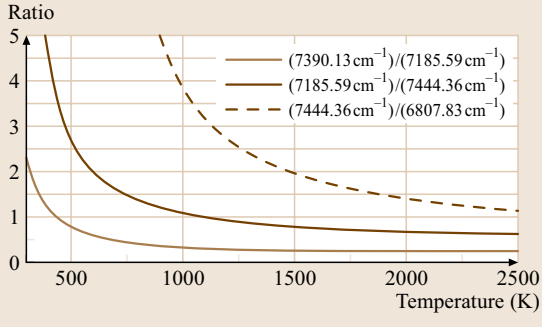

Fig. 7.30 The peak ratio and the integrated absorbance area ratio is a unique function of temperature. Shown are three different ratios from the four water transitions used in [7.118]

In principle, there are different ways to detect integrated absorbance areas. A common approach is to use tunable, spectrally narrow-band light sources and tune the wavelength over the absorption features to detect entire line-shapes. The tuning approach has some advantages in contrast to simple peak absorption measurements since one can use the integrated areas of the peaks to derive temperature more accurately. Additionally, species concentration can be measured and one is able to determine other physical parameters such as pressure (due to pressure broadening) from the line-shape.

Alternatively, spectrally broadband light can be transmitted through the region of interest and the signal can be detected by wavelength dispersion. In this way, several absorption peaks appear on the wavelength axis, with center frequencies corresponding to molecular transitions.

Tunable Diode Laser Absorption Spectroscopy (TDLAS). Laser diodes are small, easy to handle and provide powerful laser light at almost any desired wavelength in the near and mid-IR [7.100]. Diodes originally manufactured for telecommunication applications are available at low prices. Distributed feedback (DFB) laser diodes emit narrow-band [full-width at half-maximum (FWHM) $10^{-4}\,\mathrm{cm}^{-1}$] laser light that can be wavelength tuned either by varying temperature or current. The temperature tuning range is typically several nm wide, but only slowly adjustable. Current tuning can be done very fast and the tuning range is typically a few cm^{-1}. This is sufficient to tune the laser diode over an absorption line (typically $0.15\,\mathrm{cm}^{-1}$ FWHM at atmospheric pressure) within one millisecond or faster.

A typical setup for direct absorption TDLAS is shown in Fig. 7.31. The simplest sensor for TDLAS thermometry contains one fiber-coupled laser diode that is tuned over two absorption features that are spectrally close but not overlapping [7.119]. The laser light is led through a flexible fiber and pitched across the region of

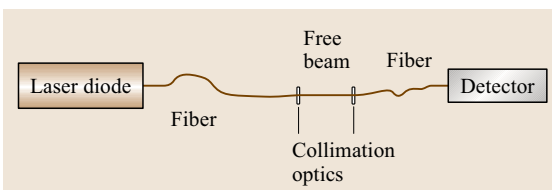

Fig. 7.31 TDLAS setup with a tunable laser diode, the system to measure within the free beam path, and the detector

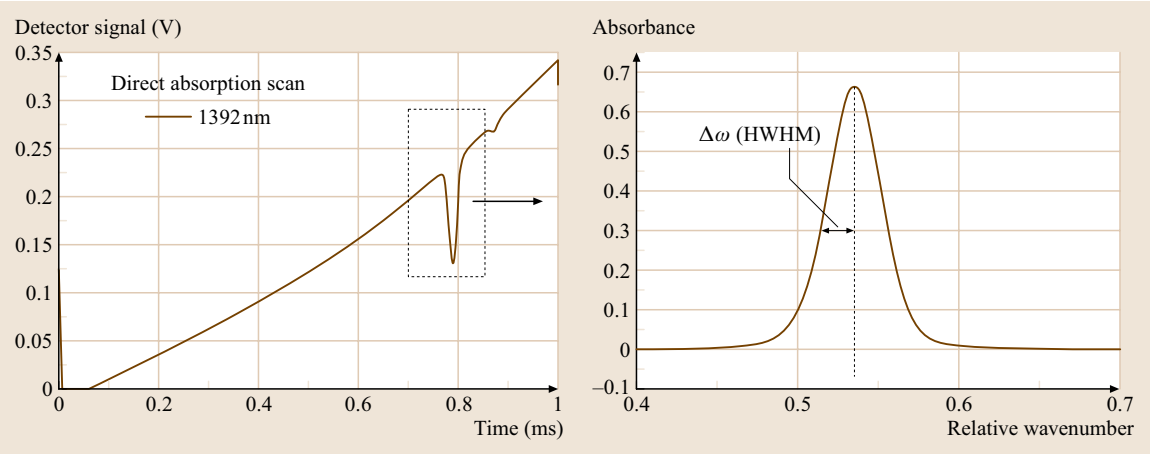

Fig. 7.32 The raw signal (*left*) is transformed into a Voigt peak [7.120]

interest. A detector collects the intensity of the transmitted light over time. The temporal variation in wavelength is observed by simultaneously monitoring the laser tuning with an etalon. The area of the Voigt-shaped absorption peak is integrated to get the integrated absorbance area a_i as shown in Fig. 7.32. A part of the laser beam can be coupled out and used as reference signal. A baseline is then fit to the scan and the peak absorbances or the integrated areas a_i of the Voigt-shaped peaks are computed to derive temperature from their ratios.

Line Selection. Two-line thermometry has a high temperature sensitivity over a limited temperature range (several 100 K) that depends on the corresponding ground-state energies of the two transitions used. In principle, the two peaks should have a large difference in ground-state energies to make sure the ratio of the detected absorptions changes strongly with temperature. But the absorbance of the two lines should be of the same order of magnitude ($0.25 < \text{ratio} < 4$) to prevent one line from dominating the ratio [7.121]. For low temperatures, lines with low ground-state energies should be used and for flame temperatures, transitions originating from higher ground-state energies are necessary. If higher accuracy over a wider temperature range is desired, several laser diodes can be multiplexed into one fiber to access more transitions with different ground-state energies. A sensor with four laser diodes has demonstrated excellent temperature sensitivity in the range 300–2500 K by using multiple ratios [7.118]. The multiplexing approach also enables temperature and several species concentrations to be monitored simultaneously, e.g., fuel and water in an engine [7.122]. The drawback of the multiplexed sensor is that the system becomes more complex since the different wavelengths of the transmitted light must be separated and detected by multiple detectors. In a 600 MW power plant, CO, H_2O and gas temperature were measured in [7.123].

Spectral positions, ground-state energies and further information about more then 1.7 million absorption lines of 37 molecules can be found in the high-resolution transmission molecular absorption/high-temperature spectroscopic absorption parameters HITRAN/HITEMP database [7.124]. Water vapor is present in moist air and is one of the main products in hydrocarbon combustion and is therefore present in many practical systems. It has a rich absorption spectrum in the mid-IR that can be probed with diode lasers. This is the reason why a combination of several water transitions is often used for temperature measurements in flow and combustion processes.

Wavelength Modulation Spectroscopy (WMS) with 2f Detection. In the simple TDLAS direct absorption approach the sensitivity is limited to absorbances of typically > 1%. This is due to the limited signal-to-noise (S/N) ratio since the small absorption signal has to be separated from the huge 100% transmission signal and a baseline has to be taken from a reference channel or from a fit to the wings of the wavelength scan. If one wishes to use peaks with lower absorbance, the laser tuning (at, e.g., 1 kHz) can be overlayed with a fast modulation frequency (of, e.g., 500 kHz). Then, the signal is detected with a lock-in amplifier to separate the phase-coupled signal from noise. When we detect the second harmonic of the modulated signal as shown in

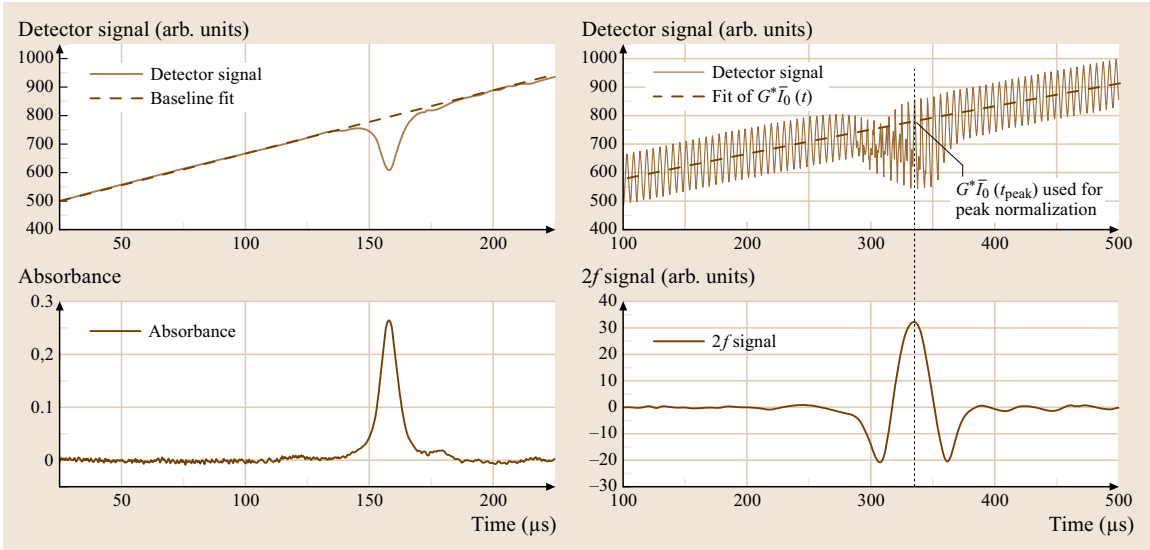

Fig. 7.33 Comparison of the direct absorption method (*left*) and the WMS technique with 2 f detection (*right*) [7.125]

Fig. 7.33, the signal sits on a zero background, making a zero-absorption baseline unnecessary.

The gain in S/N ratio is especially good for weak lines, as shown in Fig. 7.34. This gain in sensitivity comes at the expense of a more complex sensor and a more difficult interpretation of the signal. For thermometry it is sufficient to take the ratio of the peak intensities and not integrated areas. This makes the evaluation of the WMS technique with 2f detection straightforward [7.126].

Laser-Induced Fluorescence

Laser-induced fluorescence (LIF) is the process of spontaneous emission from an excited electronic state populated upon absorption of a laser photon. Large cross-sections mainly in the visible and ultraviolet spectral range enable species detection down to the sub-ppm concentration level. Many combustion-relevant species such as OH, O_2, NO, CH, CN, NH, C_2 can be accessed selectively. Detailed treatments are given in the textbooks of *Eckbreth* [7.86], *Kohse-Höinghaus* and *Jeffries* [7.77], and in the review articles of *Kohse-Höinghaus* [7.127] and *Daily* [7.128]. LIF can be understood as two subsequent steps. Absorption of (typically) one photon leads to the population of a (typically electronically) excited state in the respective atom or molecule. After a certain lifetime τ this excited species can relax into a lower-lying state by emitting a fluorescence photon. Fluorescence typically competes with alternative processes that lead to a depopulation of the excited state (quenching, photodissociation, ionization) without the emission of photons. The ratio of fluorescence rate to excitation rate is given by the fluorescence quantum yield ϕ.

Equation (7.31) describes the LIF intensity I_{LIF} for one species in the regime of weak excitation as

$$I_{LIF} = cI_{laser}N(p,T)f_{v,J}(T)B_{ik}\Gamma(p,T)\phi \qquad (7.31)$$

with c being a parameter dependent on the specific experimental setup. The LIF intensity I_{LIF} is proportional

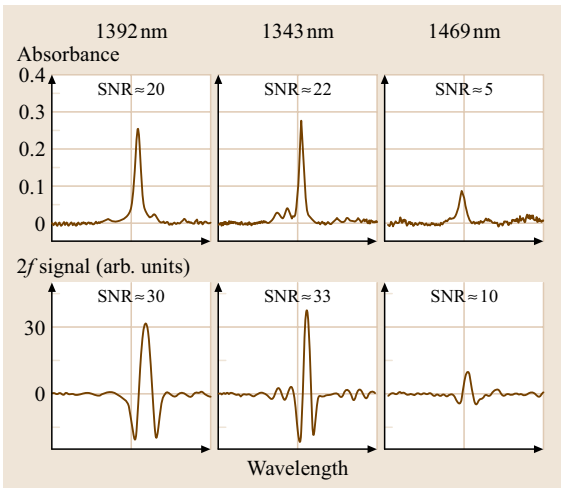

Fig. 7.34 Comparison of signal-to-noise ratios in direct absorption (*upper row*) and wavelength modulation with second-harmonic detection (*lower row*) [7.125]

to the number density of the excitable molecules in the probed volume V, which is determined by the number density of the respective species $N(p, T)$ times the temperature-dependent Boltzmann fraction $f_{v,J}$ giving the population of the initial level i. The Einstein B_{ik} coefficient describes the absorption probability for transition $i \rightarrow k$. Within the linear regime, the fluorescence intensity depends linearly on the laser intensity I_{laser} and the spectral overlap $\Gamma(p, T)$ of the laser profile and the absorption line. All these factors determine the number density of excited molecules and, therefore, the absorption part of the LIF process. The fluorescence quantum yield ϕ in (7.32) gives the ratio of the spontaneous emission rate (from level k) versus the total rate of (radiative and nonradiative) relaxation processes:

$$\phi = \frac{A_{ki}}{\sum_j A_{kj} + Q_k(p, T) + P_k} \,. \tag{7.32}$$

ϕ therefore depends on the rate of spontaneous emission (given by the Einstein A_{ki} coefficient) divided by the sum of the rates of all depopulation processes of the excited state (spontaneous emission from state k to all possible ground-state levels: ΣA_{kj}, quenching $Q_k(p, T)$ and pre-dissociation P_k). The detection efficiency of fluorescence photons depends on the observed solid angle $\Omega/4\pi$, the transmission of the optical system ε and the response of the detector η. The effects of polarization are discussed in [7.129].

When quantifying signal intensities obtained from LIF one usually has to account for numerous temperature-dependent effects. The resulting overall temperature dependence in turn is the basis for LIF thermometry. The spectral overlap factor $\Gamma(p, T)$ can be calculated from spectra simulations which are available for the most important combustion-relevant species [7.130, 131]. This is mainly important in high-pressure applications where collisional broadening causes the individual rotational lines to blend, yielding absorption features that are spectrally broader than the laser line. At atmospheric pressure and above the denominator in the fluorescence quantum yield ϕ is dominated by fluorescence quenching ($Q \gg A$). For a large number of colliders quenching rates, e.g., for OH and NO, have been determined as a function of temperature and pressure, enabling the development of simulation models [7.132, 133]. Therefore, quenching can be quantified as long as the local gas composition and temperature are known. Additional losses from the excited state can occur due to pre-dissociation P_k and photoionization. Besides these processes other collisionally induced energy-transfer processes must be considered. Vibrational (VET) and rotational energy transfer (RET) populate excited levels within the excited state, which can subsequently fluoresce. This especially gains importance if levels with significantly different effective fluorescence lifetimes are involved. Furthermore, fluorescence signal may be shifted to different spectral regions compared to the direct transitions from the laser-populated level. The implications of these effects are discussed in further detail in [7.86, 129].

With increasing laser intensity a transition from the linear LIF response [as given in (7.31)] towards a saturation regime (with I_{LIF} independent of I_{laser}) is observed. Saturation occurs through downward pumping of population from the excited state. At the same time, the laser-coupled ground-state levels can be depleted because of too slow population equilibration via RET from neighboring states. The overall effect can be modeled based on the rate equations of the individual processes. For simple systems with constant laser intensity, the system (that is, its state populations) reaches a steady state after some characteristic time τ_{ss}. If the temporal laser pulse width τ_{laser} is much larger than τ_{ss}, the steady-state solution may be used to describe the overall LIF process. This yields relatively simple *nontransient LIF models* [7.130, 134]. *Transient LIF models*, on the other hand, involve solving the fully time-dependent rate equations [7.129, 135]. For many practical applications, simple nontransient models yield an adequate description of the LIF process. This is true in particular for nanosecond laser excitation and high-pressure environments.

LIF Thermometry: Theory. For LIF thermometry, different methods have been established that involve different experimental and data evaluation procedures: single-line techniques (where only a single ground state is probed), two-line techniques (where two ground states are probed and the temperature is inferred from the ratio of two LIF intensities), and multi-line techniques (where three or more ground states are probed and temperature is inferred from a Boltzmann plot or by fitting spectral simulations). Theoretical analysis of line-shape, quenching, energy transfer, and noise effects for the different techniques have been performed by several authors [7.129, 136–139].

Particularly relevant in this context are of course the temperature-dependent terms. The dominant temperature influence in (7.31) is given by the Boltzmann fraction (7.16) of the species population in the laser-excited ground state. The temperature dependence is due to both the exponential factor for the particular

transition and the partition function $Z(T)$. The spectral overlap fraction Γ depends on temperature via collisional broadening and shifting effects. The quenching rate Q depends on temperature due to both the varying collisional frequency and quenching cross-sections. Finally, the number density N of the target LIF species depends on concentration, pressure, and temperature via the ideal gas law.

In *single-line LIF thermometry*, an overall temperature dependence of the LIF signal can be calculated from (7.31) if the spectroscopic data (term energies for Boltzmann fraction, collisional broadening, quenching) are known. The laser intensity I_{laser} is readily measured. It is, however, evident from (7.31) that the number density of the target species N must be known. This is the case in nonreactive flows where concentrations are constant (e.g., O_2 in the inlet stroke of internal combustion engines [7.140], or NO seeded in constant amounts to a flow [7.138]) or when concentrations can be derived from chemical kinetic simulations (as shown, e.g., for NO in a low-pressure flame [7.141]). Finally, the calculated relative temperatures need to be calibrated at a known temperature.

Two-line LIF thermometry is much more frequently used. In this approach, two LIF measurements are performed from different ground states. The fluorescence ratio R from the two measurements is then given by

$$R_{12} = \frac{I_{\text{LIF},1}}{I_{\text{LIF},2}} = \frac{c_1 I_{\text{laser},1} g_1 \exp\left(-\frac{\varepsilon_1}{k_B T}\right) B_1 \Gamma_1(p,T) \frac{A_1}{[A_1+Q_1(p,T)]}}{c_2 I_{\text{laser},2} g_2 \exp\left(-\frac{\varepsilon_2}{k_B T}\right) B_2 \Gamma_2(p,T) \frac{A_2}{[A_2+Q_2(p,T)]}} \tag{7.33}$$

with ε_i being the term values in Joules. By taking the ratio the species concentration, which is the major unknown factor in most applications, cancels out. This makes the two-line techniques applicable to reacting systems. It should be noted that the partition function $Z(T)$ also cancels out in the ratio.

Commonly, more assumptions about the remaining temperature-dependent factors are made: Q is assumed to dominate over A (which is usually the case in atmospheric or high-pressure systems); if Q is the same for the excited states in both measurements (by choosing either a molecule for which Q does not depend on the rotational quantum number such as NO, or by choosing transitions that excite into the same upper state), then Q also cancels out: the ratio R_{12} becomes independent of quenching processes. If, finally, the temperature dependence of the overlap coefficients and the influence of laser energy fluctuations are neglected, then the fluorescence ratio is given by a Boltzmann relation only,

$$R_{12} \propto \exp\left(-\frac{\Delta\varepsilon_{12}}{k_B T}\right) \tag{7.34}$$

depending on the temperature T, the ground-state energy difference $\Delta\varepsilon_{12}$, and the Boltzmann constant k. Equation (7.34) reduces the temperature dependence of the LIF ratio to the temperature dependence of the relative ground-state populations, which represents the most important temperature influence in the two-line technique. Nevertheless, additional influence of the overlap fraction $\Gamma(p, T)$ and quenching $Q(p, T)$ may become important depending on the specific target species.

The constants c_1 and c_2 in (7.33) summarize the efficiency of the detection system. If they are the same for both excitation wavelengths, quantitative temperature measurements are in principle possible without calibration if the spectroscopic constants of the two transitions are known. In many cases, however, known temperature data is necessary to calibrate the c_1/c_2 ratio.

The precision of any thermometry technique depends on the sensitivity of the LIF signal strength(s) on temperature. In a two-line technique, high sensitivity of the fluorescence ratio R_{12} on temperature is desired, i. e., a large change in R_{12} with temperature. Mathematically, this can be expressed as the second derivative being zero:

$$\frac{d^2 R_{12}}{dT^2} = 0 \Leftrightarrow T = \frac{\Delta\varepsilon_{12}}{2k} . \tag{7.35}$$

Depending on the temperature range to be investigated in the two-line technique, this equation gives the condition for the ground-state energy differences that yield the highest temperature sensitivity. For much higher or lower temperatures, the sensitivity may decrease severely. A two-line technique is therefore most sensitive within a certain temperature range only. Table 7.4 compares the sensitivities of different NO two-line thermometry methods used in flames.

Multi-line LIF thermometry offers high temperature sensitivity over a wide temperature range by probing a number of ground states with different term energies. In a basic approach we can assume, similar to the two-line technique, that the main temperature influence of the LIF signal arises from the ground-state population only. Furthermore it is assumed that the influence of temperature on the overlap fraction and quenching is equal for all transitions, c is equal for all transitions, and

Table 7.4 Comparison of the temperature sensitivities of different NO two-line LIF thermometry methods in flames

Reference	Excited NO lines	Maximum temperature sensitivity $\Delta\varepsilon_{12}/2k$ (K)
Tamura et al. [7.142]	$A-X(0,0)O_{12}(1.5)$ and $A-X(0,0)O_{12}(19.5)$	498
Tsujishita et al. [7.143]	$A-X(0,0)Q_2(17.5)$ and $A-X(0,0)Q_2(27.5)$	566
Bessler et al. [7.144]	$A-X(0,0)Q_1$ & $P_{21}(33.5)$ and $A-X(0,2)O_{12}(5.5)$	1420
Bell et al. [7.145]	$A-X(0,0)R_1$ & $Q_{21}(21.5)$ and $A-X(0,2)O_{12}(8.5-10.5)$ band head	2300

$A \ll Q$ is valid. Then, for any transition i, (7.31) can be rewritten as

$$\ln\left(\frac{I_{\mathrm{LIF},i}}{I_{\mathrm{laser},i}}\frac{g_i}{A_i B_i}\right) = -\frac{1}{T}\frac{\varepsilon_i}{k} - \ln\left(\frac{Z(T)}{cN(T)\Gamma(p,T)Q(p,T)}\right), \quad (7.36)$$

where the last term is constant for all transitions. The signals $I_{\mathrm{LIF},i}$ and the laser intensity $I_{\mathrm{laser},i}$ are measured, and g_i, A_i and B_i are spectroscopic constants. By plotting the left term of (7.36) versus ε_i for different transitions, the temperature can be derived from the slope of the plot, which is $-1/k_{\mathrm{B}}T$. This is called a *Boltzmann* plot (Fig. 7.35).

In many practical applications there are a number of effects that complicate this simple analysis:

- The assumption that Q is constant for all transitions does not always hold. In OH, for example, Q is known to depend on the rotational quantum number J [7.136].
- Transitions may overlap, so that the LIF signal does not arise from a single ground state. This is the case, e.g., for NO, especially at elevated pressures. The overlap fractions Γ of many transitions must then be considered simultaneously.
- In many practical applications, background signals are present, such that $I_{\mathrm{total}} = I_{\mathrm{LIF}} + I_{\mathrm{background}}$. The simple Eqs. (7.31–7.36) then cannot be applied; instead, corrections for the background contribution are necessary.
- The assumption of weak laser excitation that was used for deriving (7.31) may not hold. LIF saturation and rotational energy transfer may have significant effects on thermometry techniques [7.129, 146].
- Especially for larger molecules, the spectroscopy is complex and often only poorly understood.

Accurate LIF thermometry techniques need to include a full description of these effects. This can either be done by multi-temperature calibration measurements (yielding an empirical description of the temperature dependence of the signals) or by using detailed spectral simulations. For NO-LIF thermometry a multi-line scanning approach [7.147] that simultaneously considers the effects of line-shape and background contribution based on spectra simulations has been developed [7.131].

Target Molecules for LIF-Based Thermometry. The choice of the target molecule for LIF thermometry influences the accessible temperature range, versatility of the technique, experimental approach, and spectroscopic evaluation procedure. Temperature measurements have been performed using atomic fluorescence tracers such as indium [7.148–150], diatomic tracers such as OH [7.136, 139, 143, 151–155], NO [7.137, 138, 142, 143, 145, 147, 153, 155–168], O_2 [7.140, 151, 169–171], iodine [7.172, 173], CH [7.163] and C_2 [7.163], and organic molecules such as ketones [7.174–177] or toluene [7.178–180]. The availability of these molecules differs in reactive systems. The presence of OH and hot O_2 is limited to regions of reactive or hot gases like behind the flame front in combustion processes; the indium technique requires the activation of a precursor within a flame front; CH and C_2 are short-lived combustion intermediates; organic molecules that can be added to the fuel are only available in unburned gases and are therefore limited to temperature measurements in unburned mixtures.

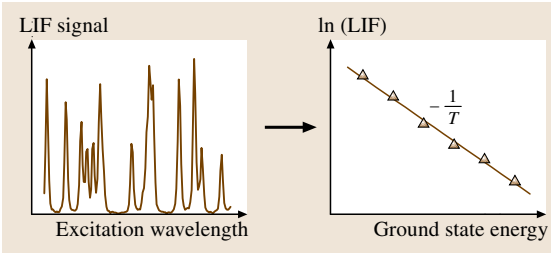

Fig. 7.35 Section of a typical LIF excitation scan (here NO at ≈ 225.3 nm) and the resulting Boltzmann plot. The slope of the Boltzmann plot gives the negative inverse temperature

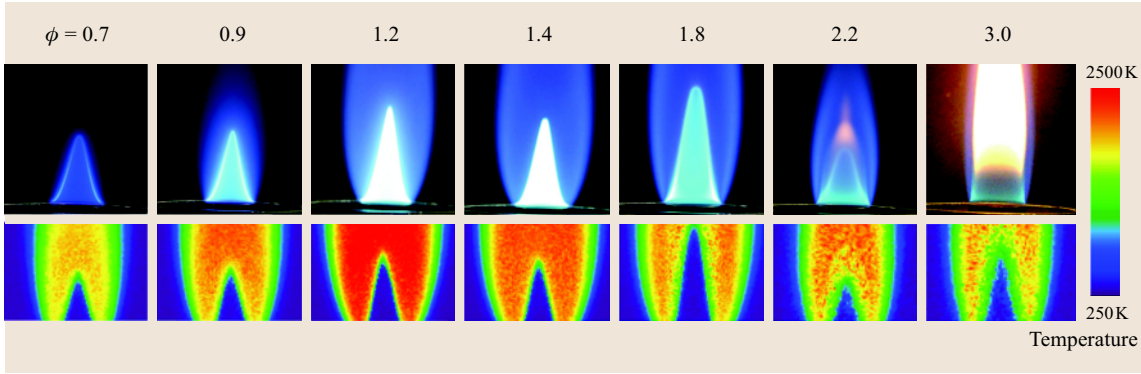

Fig. 7.36 *Top*: time-averaged flame luminosity. *Bottom*: temperature fields measured with NO multi-line LIF thermometry in laboratory flames at different equivalence ratios ϕ [7.147]

Nitric oxide (NO), seeded into reactive flow systems, has the advantage for combustion-related thermometry to be present in both the unburned and post-flame gases (Fig. 7.36). It is stable at room and elevated temperatures and therefore has the potential of making a wide temperature range accessible for LIF thermometry. NO seeding is easy to perform and does not require difficult procedures like those required for indium. Furthermore, NO provides strong fluorescence signals. Therefore, only low seeding concentrations, which do not influence the system under study, are necessary for thermometry ($\approx 100-1000$ ppm); since NO is produced in many combustion systems, seeding may not be necessary at all. In contrast to OH, fluorescence quenching in the NO $A^2\Sigma^+$, $v' = 0$ state is insensitive to rotational quantum number [7.181–183]. Therefore, it is not required that both laser-excited transitions populate the same excited rotational level.

Single-line techniques have dominantly been applied to turbulent flows seeded with NO [7.157–159]. *Tamura* et al. used detailed chemistry simulations to calculate local NO concentrations for the interpretation of a single-line thermometry technique [7.142]. Two-line techniques have been applied to turbulent flows [7.137, 139, 160, 164, 165] and low-pressure [7.142] and atmospheric-pressure [7.143, 144, 184] flames (Table 7.4). Almost all of this work employed different rotational transitions within the $A-X(0, 0)$ vibrational bands. Vibrational temperatures have been measured with transitions in the NO $A-X(0, 0)$ and (0,2) bands [7.144]. Multi-line techniques have been applied in stable low-pressure [7.155], atmospheric-pressure [7.143, 162] and high-pressure. [7.161, 185] flames, sooting flames [7.147], and spray systems [7.167], and in an arcjet reactor [7.163]. Comparisons were performed among NO single-, two- and multi-line techniques [7.138, 142, 162]. NO thermometry has also been compared to LIF methods using other target molecules [7.143, 153, 155, 163].

Whereas mono- and diatomic species typically provide line spectra, both in absorption and fluorescence emission, in the UV that resolve individual rotational transitions, in larger molecules the high density of states causes blending of many transitions into continuous absorption and emission bands. Furthermore, intramolecular energy transfer processes (intersystem crossing, internal conversion) open up in addition to those mentioned above. The variation of the efficacy of these energy-transfer paths as a function of vibrational excitation, temperature and pressure, can result in a temperature-dependent shift of the absorption and emission spectra.

Organic molecules such as aromatics and ketones are frequently used for observing mixing processes between fuel and air in combustion systems [7.186]. The original application was fuel concentration measurements. For many of these substances that are often used as fluorescent tracers pronounced temperature dependence has been found. The temperature dependence of LIF signals from organic molecules is usually a detrimental effect for quantitative fuel concentration measurements. However, the temperature dependence can also be exploited to measure temperature and even to measure temperature and fuel concentration simultaneously.

For a few larger organic molecules the temperature behavior of absorption cross-sections and fluorescence quantum yields is well enough understood to use them for gas-phase measurements. Acetone has been most thoroughly studied and has been used for temperature measurements in flows [7.175, 187, 188]. The under-

standing of 3-pentanone fluorescence has also evolved to a state [7.187, 189] that makes this tracer useful not only for fuel concentration but also for simultaneous temperature measurements, i. e., in internal combustion engines [7.176, 188]. The temperature effects in toluene LIF have been investigated [7.178, 180, 190]. It appears that toluene is also suitable as a tracer for measuring temperature at least in oxygen-free environments [7.179]. The combination of simultaneous temperature and fuel concentration measurements is particularly interesting for combustion systems because it provides fuel number densities, fuel concentrations and equivalence ratios (based on the assumption that oxygen is evenly distributed within the air) in fuel/air mixtures prior to ignition [7.188].

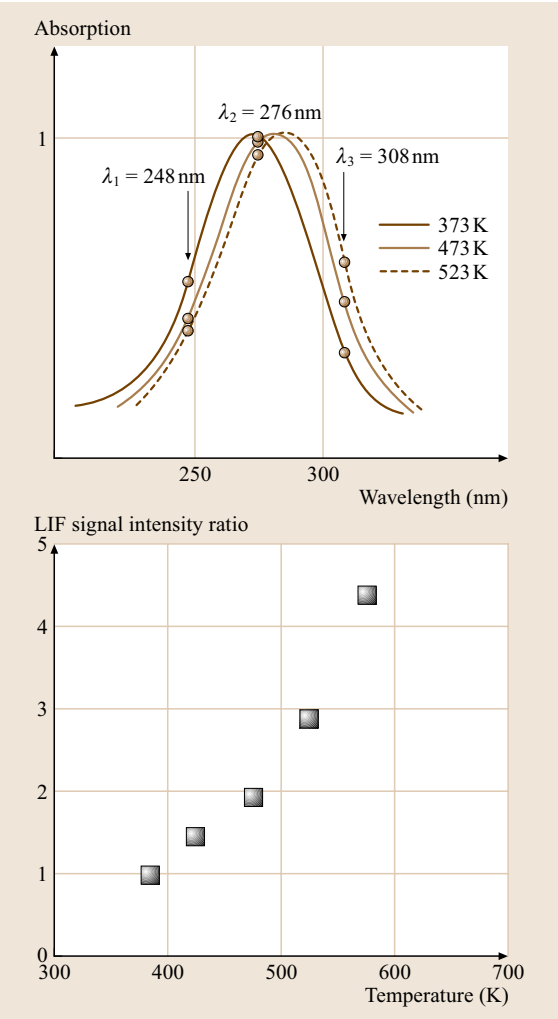

Fig. 7.37 Temperature dependence of the absorption spectrum of 3-pentanone (*top*) and the resulting temperature effect (*bottom*) found by taking the ratio of the signals from two excitation wavelengths (248 and 348 nm), which is the basis for thermometry based on two excitation colors and a single detection color [7.188]

Thurber et al. [7.175] determined temperature fields (350–500 K range) in a flow passing a heated cylinder using single-line excitation of acetone at 248 nm. In this nonreacting flow the mole fraction of acetone in a nitrogen stream was constant. Independence from the requirement of constant mole fraction is achieved when two-line excitation schemes are employed. This was first demonstrated for 3-pentanone by *Großmann* et al. [7.187] and then expanded for applications with acetone by *Thurber* et al. [7.175, 191]. They also compared single- and two-line acetone thermometry and assesses the conditions (for homogeneous distribution of tracers) where one of the two techniques has advantages in terms of temperature precision and signal-to-noise ratio [7.175].

The absorption spectrum of 3-pentanone exhibits a temperature-induced shift towards longer wavelengths of about 10 nm per increase of 100 K (Fig. 7.37). Upon excitation in this region, fluorescence is emitted between 330 and 550 nm, with a spectral distribution that is almost independent of the absorbed wavelength. This spectral shift of the absorption, albeit undesired for concentration measurements with single-wavelength excitation, can be used for measuring temperature. After excitation at two different wavelengths (248 and 308 nm)

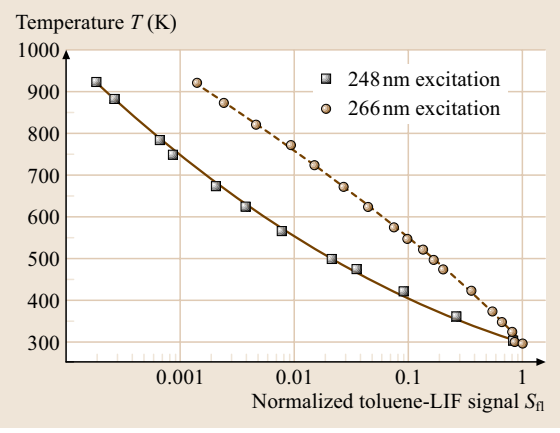

Fig. 7.38 Calibration curves for the determination of temperature from the toluene LIF signal in a homogeneously seeded nitrogen gas flow at atmospheric pressure (*Symbols*: experimental data, *lines*: fit)

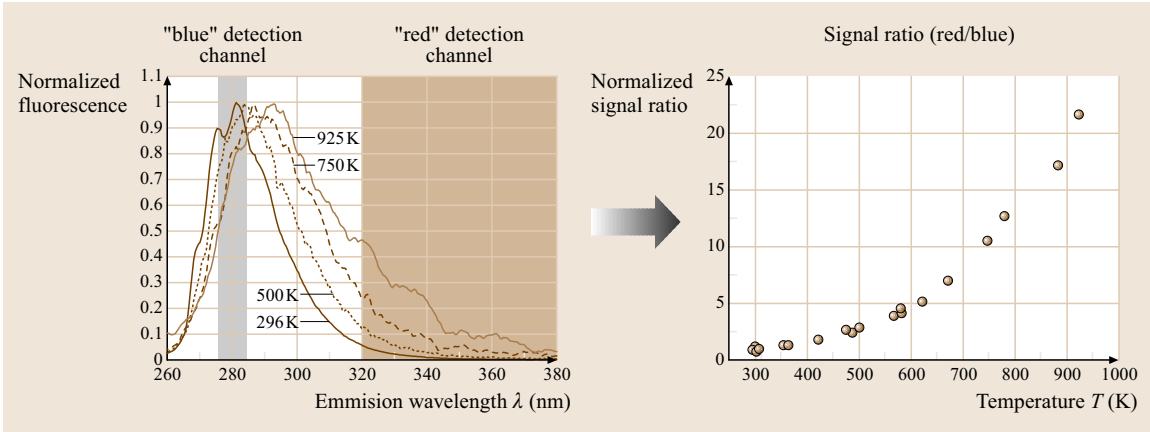

Fig. 7.39 Scheme for two-color toluene LIF

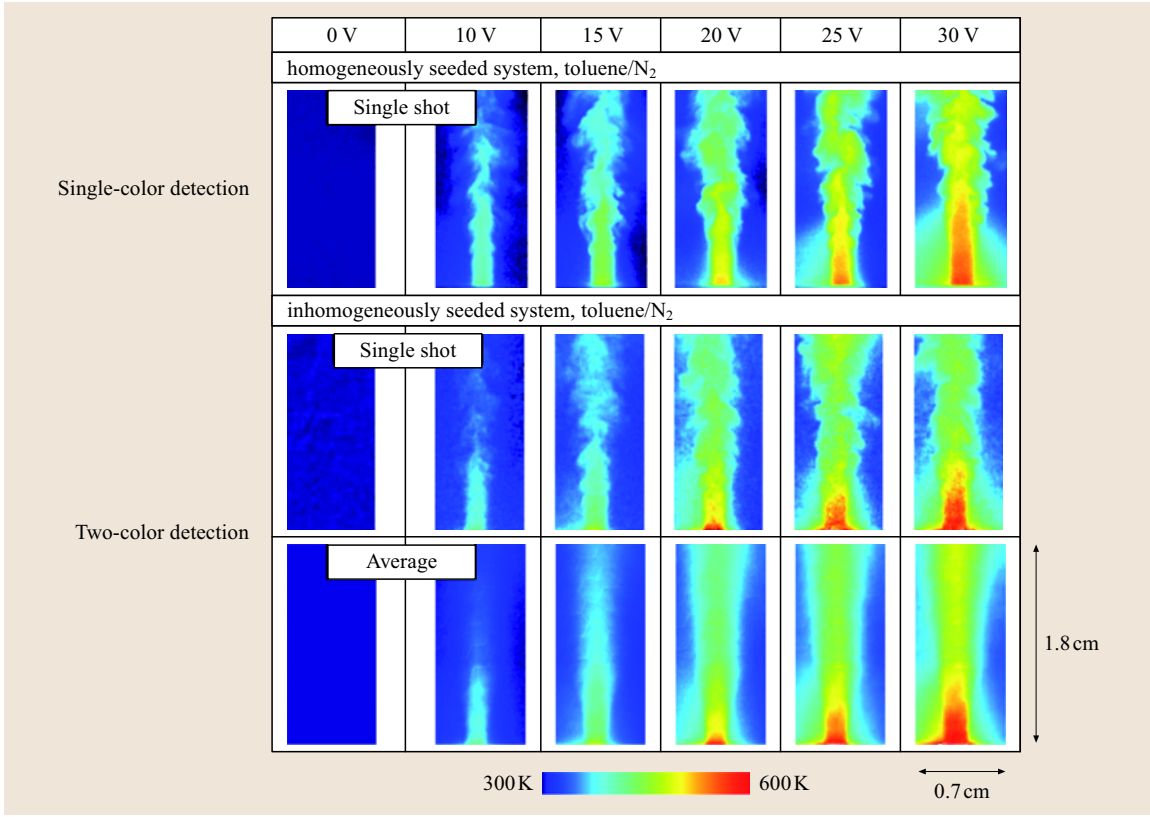

Fig. 7.40 Temperature measurements based on toluene LIF. From *left* to *right* increasing heating power of the injected gas jet that is injected into room-temperature nitrogen [7.177]

the ratio of the LIF intensities reflects the local temperature; Fig. 7.37 shows data for 308 nm [7.192]. In imaging measurements the local temperature can be evaluated for each pixel from the relative signal intensities. This technique has been applied to measurements in an optically-accessible two-stroke engine [7.176, 188].

The temperature dependence of the toluene LIF signal can be used to visualize temperature distributions in homogenously seeded flows using a one-laser one-camera setup based on the strong variation of the fluorescence quantum yield with temperature (Fig. 7.38). In flows with inhomogeneous toluene concentration distribution (e.g., mixing studies) the LIF signal depends on both the local tracer number density and the local temperature. In this case, one can take advantage of the red shift of the emission spectrum with increasing temperature (Fig. 7.39). A two-color detection technique, using single-color excitation and two-color detection then allows temperature measurements.

A demonstration of toluene LIF thermometry based on single- and two-color detection is shown in Fig. 7.40 [7.177]. A heated gas jet is injected through a 1.7 mm orifice into room-temperature nitrogen. The jet and the surrounding atmosphere is seeded with 0.5–2% toluene. The first row of images relies on spatially invariant toluene composition while the second row displays images where the toluene concentration in the jet and the surrounding area is different. The first two lines shows single-shot images, the third row displays temperature measurements that are averaged over subsequent measurements. Images are taken with 248 nm excitation and detection in the spectral bands shown in the left frame in Fig. 7.39.

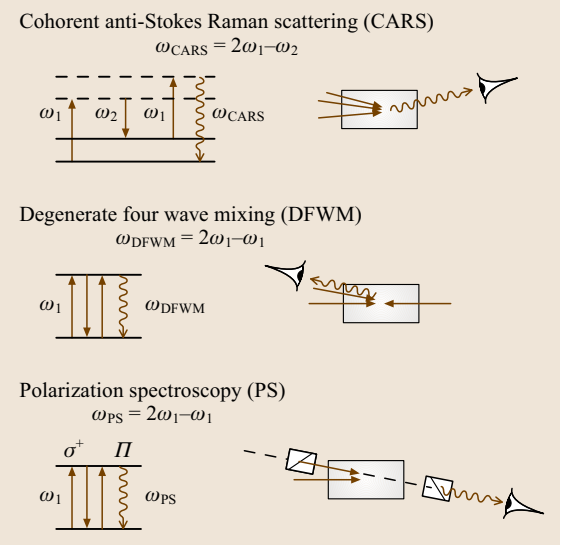

Fig. 7.41 *Left*: energy-level diagrams of various optical four-wave-mixing techniques. *Right*: schematic experimental arrangements of laser beams and direction of signal detection

7.3.4 Nonlinear Techniques

Nonlinear wave-mixing phenomena are usually not observed at the low light intensities of incoherent thermal radiators. However, the development of high-power tunable laser systems has triggered the study of numerous new nonlinear optical phenomena in liquid, solid and gaseous samples. The attained signal intensities in molecule-specific resonantly enhanced higher-order wave mixing processes can be large due to their strong dependence on the intensities of all incoming beams, the concentration of the sample molecule and the interaction length (e.g., the effective spatial extent in the sample where the signal is produced inside the interaction region of all beams). The energy level schemes of multibeam techniques most often established in combustion diagnostics today are summarized in Fig. 7.41 together with sketches of the experimental setups. The nonlinear susceptibilities are enhanced whenever one or more of the frequencies of the in-

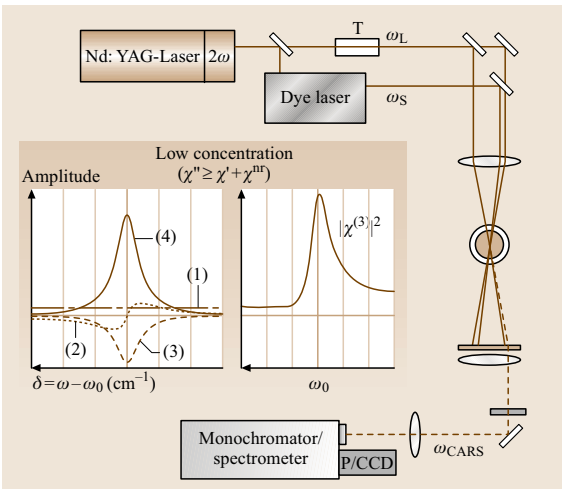

Fig. 7.42 Experimental arrangement of a CARS spectrometer. The dye laser can be either a narrow-band laser for scanning CARS or a broadband laser for single-shot CARS thermometry. In the case of scanning CARS a photomultiplier tube is used at the exit plane of the monochromator; in the case of a broadband dye laser a CCD camera is used in connection with a spectrometer. The *insets* show a typical CARS line-shape function for an isolated transition at low concentration of the species under consideration; it is composed of the constant nonresonant background (1), the interference contributions with χ_{nr} (2, 3) and the Lorentzian-shaped resonant part (4) of the third-order susceptibility $\chi^{(3)}$

teracting laser beams coincide with allowed single- or multiphoton transitions. In the macroscopic picture the induced higher-order polarization terms arise from the nonlinear mixing of the input waves and give rise to the radiation of the same or various new sum- and/or difference frequency combinations of the frequencies of the input waves. This produces a coherent signal beam in a direction determined by the phase-matching condition

$$\boldsymbol{k}_{\mathrm{sig}} = \sum \boldsymbol{k}_j \,, \tag{7.37}$$

where $|\boldsymbol{k}_j| = n_j \omega_j / c$ is the magnitude of the corresponding beam wave vector. Through focusing of the beams good spatial resolution transverse to the beam propagation direction can be obtained with sample volumes of several tens of μm^3 without sacrificing signal intensity due to the larger crossing angles. Each of these techniques can be used for thermometry. However, CARS has emerged as the most robust technique even under harsh conditions such as gas turbine combustors [7.193].

Coherent Anti-Stokes Raman Scattering (CARS)

coherent anti-Stokes Raman scattering (CARS) [7.86] belongs to the class of nonlinear, coherent processes. A typical experimental sketch is presented in Fig. 7.42. The signals of coherent processes are generally strong and emitted in a laser-like beam, but the signal generation depends nonlinearly on the concentration of the probe molecules and is also intrinsically a nonlinear function of the exciting laser intensities. CARS therefore imposes stronger demands on the laser source such as to stability, beam quality, and mode structure, and since two laser beams are involved, on alignment. For thermometry in air-breathing flames, N_2 is used preferentially as the probe molecule because of its large concentration and the complete spectroscopic database that is available. The CARS technique allows only point measurements; simultaneous thermometry of an extended line or plane (as in LIF or Raman) is not possible. However, due to its high accuracy, CARS is often used to define a temperature standard for the investigation and validation of other thermometry methods.

In CARS experiments (Fig. 7.41) one fixed frequency (pump) and one broadband (Stokes) laser beam in the visible with a frequency difference equal to a Raman-allowed transition are aligned and focused onto the sample to create, in a four-wave mixing process, a coherent beam at the anti-Stokes frequency $(2\omega_1 - \omega_2)$, well separated spatially and spectrally from all incoming beams. The CARS radiation is then dispersed in a spectrometer and detected with a CCD camera (Fig. 7.42). In the unsaturated regime the CARS intensity at frequency $\omega_{\mathrm{CARS}} = \omega_3 = 2\omega_1 - \omega_2$ for an isolated transition [7.86] is (7.38)

$$I_{\mathrm{CARS}} = I_3 = \frac{\omega_3^2}{n_1^2 n_2 n_3 c^4 \varepsilon_0^2} (lN\Delta_j)^2 I_1^2 I_2 \left| \chi^{(3)}_{\mathrm{CARS}} \right|^2 \,, \tag{7.38}$$

with

$$\chi^{(3)}_{\mathrm{CARS}} = K_j \frac{\Gamma_j}{2\Delta\omega_j - \mathrm{i}\Gamma_j} + \chi_{\mathrm{nr}} \,;$$

$$K_j = \frac{\omega_3^2 (4\pi)^2 n_1 \varepsilon_0 c^4}{n_2 \hbar \omega_2^4 \Gamma_j} \left(\frac{\partial \sigma}{\partial \Omega} \right)_j \,; \tag{7.39}$$

I_{CARS} is dependent on higher powers of the pump (1) and Stokes (2) laser intensities as well as on the square of the number density difference $N\Delta_j$ between the lower and upper Raman levels of the j-th transition. Equation (7.38) is written for perfect phase matching of the beams, i. e., when (7.37) holds and the corresponding signal intensity is maximized. Γ_j is the total broadening rate of the transition and $\Delta\omega_j = \omega_1 - \omega_2 - \omega_j$, the detuning from the Raman transition frequency. The spectral structure of the CARS signature over thermally populated levels is contained in the expression of the third-order susceptibility $\chi^{(3)}$ (7.39), which is therefore an accurate measure of the gas temperature. This is exploited for thermometry applications through least squares fitting of computer-generated to experimental CARS spectral shapes, if proper account is taken of the various physical effects contributing to the CARS spectral signature, such as coherences in the CARS pump beams [7.194, 195], saturation and collisional effects [7.196, 197] or the noise characteristics when broadband Stokes lasers are employed [7.198].

In their pioneering work *Taran* et al. [7.199] recorded the first CARS spectra of molecular hydrogen in an atmospheric pressure Bunsen flame using a narrowband scanning dye laser as a Stokes beam. *Eckbreth* et al. [7.193] introduced single-pulse temperature and species measurements by using a broadband Stokes dye laser that covers Raman shifts of the whole investigated spectral branch. Species concentrations can be determined from either the integrated CARS line intensity or its spectral shape [7.200, 201] through calibration measurements and spectral modeling, respectively. For

low concentrations the (real) nonresonant contribution χ_{nr} in the susceptibility expression (7.39) is significant and limits the detection sensitivity due to interference with the resonant contribution. To illustrate this behavior, the real and imaginary susceptibility components determining the CARS line-shape are depicted in the inset of Fig. 7.42 for an assumed low concentration of the resonant species in a nonresonant buffer gas.

Due to the $\Delta v = 1$, $\Delta J = 0$ selection rules in vibrational Q-branch Raman spectra, individual lines are closely spaced and one needs different laser dyes to cover all the Stokes wavelengths for detecting different species. Alternatively, *Aldén* et al. and *Seeger* et al. excited the pure rotational transitions to enable temperature and species concentration measurements to be made in what is called the single-shot broadband rotational CARS (RCARS) technique [7.202–204]. The 4-dicyanmethylene-2-methyl-6-(p-dimethylaminostyryl)-4H-pyran (DCM) laser dye covers most of the rotational Stokes shift even for spectra at 1000 K or higher and multiple species can be detected within the same spectral range as well. Since both the pump and Stokes beam in the corresponding level scheme (Fig. 7.41) originate from the same Stokes laser, additional spectral noise averaging takes place, which makes this technique less susceptible to mode noise in the laser sources. Problems in this technique are stray light from the pump beam as well as a lower temperature measurement accuracy at high temperatures.

7.3.5 Conclusions

In this section various spectroscopic methods that enable non-intrusive temperature measurements have been outlined. The main focus here was on gas-phase applications. In general, no single technique for thermometry is appropriate for all problems. Depending on the demands such as the required resolution, accuracy, and precision, and parameters such as the density, gas composition, and temperature range, different techniques exhibit specific benefits. Common to all the methods discussed is the application of lasers as a light source and sensitive low-noise detectors. Low-signal techniques such as Raman scattering or nonlinear techniques such as CARS have thereby recently become feasible. For other techniques such as absorption or fluorescence spectroscopy these improvements have led to dramatic improvements in sensitivity and selectivity. The various techniques differ in their temporal and spatial characteristics from time averaging to instantaneous detection and from point (0-D), line (1-D) or planar (2-D) measurements.

Most of the instrumentation necessary for laser-based thermometry is commercially available. The different methods were not only developed for laboratory environments but have already proved their applicability in harsh environments in many cases. Problems in fluid mechanics, engineering science and others have been tackled using laser diagnostics with great success. Spectroscopy is therefore a prominent example of the transfer of fundamental science to the solution of technical tasks.

7.4 Transition Detection by Temperature-Sensitive Paint

7.4.1 Introduction

The method of temperature-sensitive paint (TSP) encompasses the visualization and quantitative evaluation of the temperature on a body's surface with the help of a temperature-sensitive coating. This coating has to be excited by narrow-band, incident light and temperature-sensitive emitted light is detected with the help of photosensitive devices (i. e., CCD cameras). In contrast to thermometric measurements using point sensors such as thermocouples or resistance temperature detectors, this method enables the mapping of a complete three-dimensional (3-D) surface at once. An overview of temperature measurement in general is given, for example, by *Childs* et al. [7.205].

Short Historical Overview

Nowadays, there may be the impression that the TSP technique is a rather new method that had emerged at the same time as the pressure-sensitive paint (PSP) method in the 1980s. But this holds true (if at all) for the *name TSP* only. The technique itself has been known (and in use) since the 1940s and is well documented in the literature in a variety of papers dealing with *thermographic phosphors* or *phosphor thermometry*. Moreover, the principle of phosphorescence has been known much longer and was largely the domain of academia until the introduction of the fluorescent lamp in the 1930s. In parallel to this, there was increased interest in luminescing materials and the temperature dependency of such *phosphors* soon played an important rule, since the

degradation of light output with increasing temperature represents a drawback for lamp manufacturing. Therefore, thermal characterization was an important task for those studying phosphors and it was early suggested by *Neubert* [7.206] to use phosphors for temperature measurements. The thermographic *method* originated with *Urbach* in 1949 [7.207], who additionally published the characteristics of a number of thermally sensitive phosphors known at that time.

Phosphor thermometry as a tool for 2-D surface temperature measurement on a wind-tunnel model was reported for the first time by *Bradley* in 1953 [7.208]. He used a half-wedge which was partly covered by a phosphor-coated plastic sheet to study the boundary layer in a supersonic flow (Mach number $M = 2.3$), using a temperature-sensitive coating provided by Urbach. In the following decades, the development of rockets and space reentry vehicles had shown the need for heat transfer measurements on wind-tunnel models, especially in supersonic and hypersonic testing. Therefore, the use of temperature-sensitive paints was concentrated on inorganic, thermographic phosphors capable of being applied in the high temperature range [7.209].

Additionally to wind tunnel testing, the TSP method with the use of thermographic phosphors was applied to a variety of other applications. For example, Monaweck and McGonnagle [7.210] used the method of phosphor thermometry in 1956 for nondestructive testing of reactor fuel elements, where the heat transfer from the fuel to the coolant was investigated. Ongoing development of the *thermographic phosphor thermography* (TPT) has extended its application range to temperature field measurement on electronic circuits, isolation checks, to medicine, or turbine and combustion testing, to name just a few examples. Furthermore, research has been undertaken to use thermographic phosphors to compensate the temperature dependency of pressure-sensitive paints [7.211].

With the advent of modern infrared (IR) camera techniques, an alternative method has been made available for heat transfer measurement on wind-tunnel models, as long as combustion is not involved. Since in turbine testing the radiation of combustion is superimposed on the surface temperature radiation of the turbine blade under investigation, it is problematical to use the IR technique in that case. The use of a thermographic phosphor, on the other hand, makes it possible to filter out the surface temperature distribution on the blade by detecting the phosphor's fluorescence intensity in a certain wavelength range only, which is different from the radiation caused by combustion. Therefore, thermographic phosphors are a commonly used tool in turbine and combustion testing (see, for example, [7.212]), whereas their use in wind tunnels is not as widespread, since the IR technique is applicable here. Things have changed since that time, whereby now cryogenic wind tunnel testing has become more and more important.

With the advent of modern cryogenic wind tunnels like the National Aeronautics and Space Administration (NASA) Langley national transonic facility (NTF) or Europe's new counterpart, the European transonic wind tunnel (ETW), it was for the first time possible to achieve full-scale flight Reynolds numbers at transonic speeds with subscale models. By using nitrogen as the test gas instead of air, and cooling the flow by continuous injecting of liquid nitrogen, it is possible to get 5 to 6 times higher Reynolds numbers in cryogenic wind tunnels compared to so-called *warm* transonic wind tunnels. Additionally, by pressurizing the wind tunnel it is possible to increase the Reynolds number further. In high-speed testing by use of cryogenic wind tunnels, measurements are usually performed with unfixed transition. Hence, the detection of the laminar-to-turbulent boundary-layer transition nowadays has become of major interest in parallel to the increased use of cryogenic wind tunnels in the design phase of transport aircraft.

If a temperature difference is given between the laminar and turbulent part of a boundary layer which is undergoing transition, a thermographic method can be applied to detect the transition line. The use of IR cameras for surface temperature detection in cryogenic testing is rather difficult because of the rapid decrease in black-body radiation intensity and the shift to longer wavelengths, at least for temperatures less than 200 K. The method of thermographic phosphors was a promising alternative for transition detection measurement in cryogenic wind tunnels, using *phosphors* with the highest temperature sensitivity in the cryogenic wind-tunnel temperature regime.

With the appearance of the PSP method in the 1980s, the term *TSP* had been established in parallel, now meaning the application of a thermographic paint in wind tunnel testing not exclusively based on phosphors but on organic substances as well. The term *thermographic phosphor thermography* (TPT) is most often found in the literature in relation to turbine testing, combustion or hypersonic flow/heat transfer measurement. TSP can be interpreted as a general category which includes thermographic phosphors as a subset. *CryoTSP* describes the use of temperature-sensitive paints mainly for transition detection in cryogenic wind tunnels.

At the end of this chapter, the application of the TSP technique is described with respect to transition detection in cryogenic wind tunnels. For the same purpose it can be used in *warm* wind tunnels as well, simply by applying another paint. Using TSP for measuring absolute temperatures on a model surface in a cryogenic wind tunnel is of less interest since the temperature of the model is determined by the adjusted flow temperature, thus having no real aerodynamic relevance as opposed to heat transfer measurement in hypersonic wind tunnels. However, it is possible to perform absolute temperature measurements by cryoTSP the same way.

A comprehensive review on thermographic phosphors, including a more-detailed historical overview, is given in *Allison* and *Gillies* [7.214]. Pioneering work in the development of high-sensitivity paints for application to warm and cryogenic wind tunnels was carried out by *Campbell* et al. [7.215–217], *McLachlan* et al. [7.218], *Asai* and co-workers [7.219] or *Popernack* et al. [7.220]. In the following, the TSP method will be sometimes compared with other 2-D thermographic methods applicable to wind tunnel testing, namely infrared thermography (IRT) and thermography by use of thermochromic liquid crystals (TLC). A more-detailed comparison of the three techniques with respect to their suitability for transition detection is given in [7.221]. The summarized results of this comparison are shown in a table at the end of this section.

Thermography by the Use of Thermographic Phosphors

Thermographic phosphors mostly consist of a binder and a luminescent crystalline phosphor. Usually, the phosphor is a transition metal compound or a rare earth compound, such as yttrium oxysulfide or vanadate (V). Oxysulfides and phosphates singly doped with europium (Eu), terbium (Tb) or dysprosium (Dy) are also used. Here, the second dye provides the temperature sensitivity of the phosphor, which can be adjusted by tuning the doping rate. Thermographic phosphors can be applied to a surface as paint, consisting of thermostable binder mixed with the crystalline phosphor and sprayed with an airbrush, for example. In general, a wide variety of different sensors are known, and they cover a wide temperature range, starting from cryogenic temperatures up to 2000 K.

As an example, the phosphor formulation Y_2O_2S:0.15% Eu^{3+} as described in [7.213] will be addressed here. The luminescent rare-earth atom (here Eu) is excited by UV light and exhibits a temperature-dependent spectral distribution of fluorescent light, as shown in Fig. 7.43. The spectrum shows discrete lines in the visible range. The energy distribution within the different spectral lines is dependent on temperature, i. e. different temperatures leading to different colors of the emitted light, starting from orange–white at 290 K and going to red when the temperature increases to 420 K [7.213]. If the temperature remains below 570 K, the coating will survive and the sensor can be used repeatedly. A benefit of thermographic phosphors compared to liquid crystals, for example, is that viewing angle, pressure (or strain), and UV light intensity do not affect the emission color.

A thermographic phosphor (or a temperature-sensitive paint in general) does not necessarily exhibit a line spectrum as shown in Fig. 7.43. Wide-band emission spectra can be observed for temperature-sensitive molecules as well. Possible methods for evaluation of TSP thermograms may differ somehow depending on whether the emission spectrum is a line or continuous spectrum, but in principle they are comparable. A well-known method of temperature measurement by means of TSP is the so-called *intensity method*, where the total energy of the temperature-dependent emission light of the paint is used to evaluate temperatures. This method will be described in more detail later.

In general, the decay time (or lifetime) of fluorescence/phosphorescence is also sensitive to temperature (moreover, it is the *reason* for the temperature-dependent intensity), and in some applications evaluation of the lifetime of emission instead of the integral intensity will be more accurate. Nevertheless, it is more difficult to get complete surface thermograms based on lifetime meas-

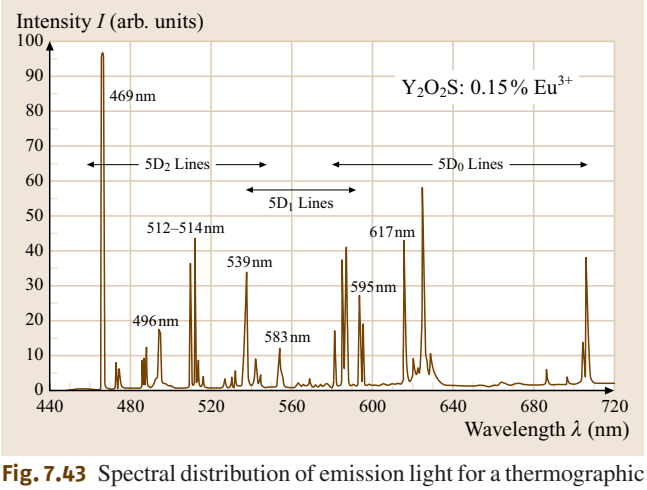

Fig. 7.43 Spectral distribution of emission light for a thermographic phosphor with line spectrum [7.213]

urement since one has to use intensified CCD cameras for direct 2-D evaluation, or a 1-D scanning system based on a photomultiplier.

In lifetime measurement, one has to excite the sensor (i. e., the paint) by a short light pulse [generated by a laser or a high-power light-emitting diode (LED) system]. Pulse duration is of the order of nanoseconds and after being excited, the TSP emits light whose intensity has a characteristic, exponential decay time (the lifetime τ), which can range from microseconds up to milliseconds. Figure 7.44, for example, shows the lifetime for the phosphor $Mg(F)GeO_6$ excited by a 266 nm pulsed laser. Starting from ambient conditions up to 550 K it shows temperature dependency of lifetime (note the logarithmic scale) and especially for $T > 400\,°C$, it shows high sensitivity, possibly making it a good sensor for that temperature range.

The method of thermographic phosphors is widely used in turbine, combustion and heat transfer measurement [7.222]. TSP in general up to now is not often used in low-speed or (warm) transonic wind-tunnel testing since infrared camera systems can be applied. However, the advantage of the TSP method compared to IRT is the large choice of optics, which may support a larger number of applications. Furthermore, high-speed cameras can be used, which enable detection of short-duration signals, this is still being a challenge with IRT.

Based on the two physical properties (temperature-sensitive *spectral distribution* and *lifetime*), at least three methods of thermographic imaging using phosphors can be defined: First, one can measure the color of emission light by the use of red–green–blue (RGB) cameras for phosphors showing line spectra. However, since the color of the light of these molecules changes less dramatically than for liquid crystals (TP: orange–white to red within 100 K. LC: red to blue within 1 K for narrow-band, or within 20 K for wide-band, liquid crystals) this technique shows rather high uncertainty. Secondly, one can use two different black-and-white (b/w) cameras equipped with optical filters, cutting out only two lines of the (multiline) emission spectrum of the thermographic phosphor (Fig. 7.43). Then, temperature calibration can be carried out by forming ratios of the two images (which have to be aligned accurately to allow for the different viewing angles). Thirdly, one optical light-gathering system and a beam splitter can be used with the two cameras to ensure the same viewing angle (but it is a rather old-fashioned method).

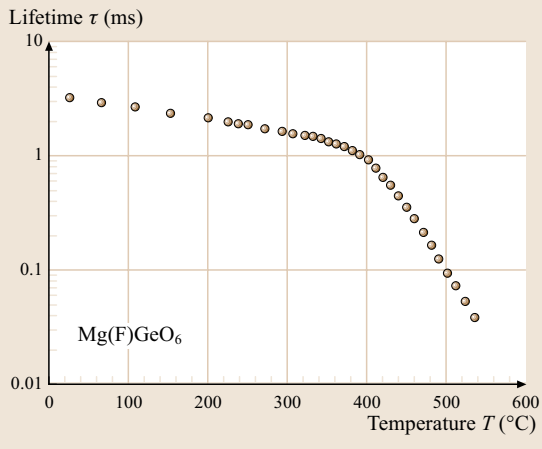

Fig. 7.44 Lifetime change with temperature for a thermographic phosphor with high sensitivity for $T > 400\,°C$

Another possibility is to relate images under temperature variations with a reference image at constant temperature, comparable to PSP evaluation (Sect. 4.2.2) where a *wind-OFF* image (constant pressure) is related to a *wind-ON* image (with a given aerodynamic pressure distribution). This method works well when the temperature-sensitive paint has a wide band emission rather than a line spectrum (intensity method).

Since the application of thermographic phosphors in aerodynamics was in the beginning mainly developed for hypersonic wind tunnels, the temperature increase was quite large and fast. Therefore, TPT development was focused on image processing and heat flux data reduction rather than on temperature measurement accuracy. One important matter is the insulating property of the paint, which is an issue for heat flux application. This is even the reason why NASA has developed an impressive technique that includes casting the model with the same binder as used for the paint [7.223].

Apart from phosphors, organic sensors can also be used for paint-based temperature measurement, but they can be destroyed by heat at higher temperatures and therefore cannot be used in hypersonic wind tunnels or combustion testing. However, this difference is more due to the material properties of the organic sensors than their functional characteristics; excitation wavelengths (UV or visible range), emission spectrum (line spectrum or wide band), wavelength shift ($\lambda_{em} - \lambda_{exc}$), and suitability for intensity or lifetime method are comparable for both kinds of temperature-sensitive paints. There is furthermore a difference in the solubility of the temperature-sensitive compound in a suited binder: phosphors tend to cluster more than organic sensors and it is more difficult to obtain a homogenously emitting paint. In the following, we will use the term temperature-

sensitive paint (TSP) for paints that are based either on phosphors or on organic molecules.

Temperature Range, Sensitivity, Spatial Resolution and Time Response of TSP

Existing TSP formulations cover the temperature range $80\,\mathrm{K} < T < 2000\,\mathrm{K}$, with the bandwidth of a single TSP being around 100 K. A comprehensive survey of different temperature-sensitive paint formulations is given in [7.224]. Some temperature-sensitive molecules show their highest sensitivity at cryogenic conditions, say, $100\,\mathrm{K} < T < 200\,\mathrm{K}$ (Fig. 7.45). The accuracy of TSP is typically around 0.1–0.8 K. As a rule of thumb, for the transition detection measurement without referencing and calibration one can clearly resolve about 0.5 K when using scientific CCD cameras with a 12 bit dynamic range. Sensitivity may be enhanced by using low noise, 16 bit CCD cameras or pixel binning. By performing a calibration of the TSP on the model under investigation (which requires temperature sensors to be in contact with the paint), and by averaging several images, thermograms with relative accuracy of less than 0.1 K can be acquired with the TSP technique. This is still more than with modern IR cameras, where up to 0.02 K changes can be resolved.

Spatial resolution is mainly determined by the CCD camera and optical detection system and therefore can by very high; this is a benefit of TSP compared to IRT. For example, thermograms of 4000×2700 pixels^2 with 14 bit dynamic range are state of the art. Nevertheless, observation of a TSP layer with too high a magnification may show some *grainy* structures caused by clustering of the sensor molecules. In conventional wind-tunnel testing (imaging a complete wing) this will not be a problem.

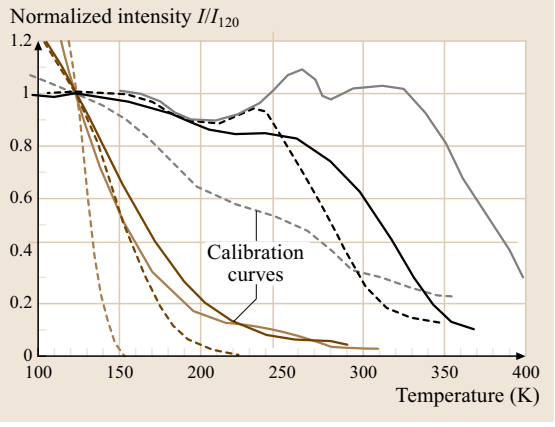

Fig. 7.45 Change of emission light intensity I with temperature for different TSPs. Some paints (brown curves) are very sensitive in the cryogenic temperature range $100 < T < 200$ K (data taken from *Liu* and *Sullivan* [7.224])

TSP has two characteristic timescales: the luminescent lifetime and the thermal diffusion timescale. The luminescent lifetime can be about 1 µs to 1 ms, which is mostly beyond the necessary exposure time for a typical TSP image in large wind-tunnel testing (approx. 1 s). However, in small wind tunnels where distances are centimeters rather than meters, the use of a high-energy light source together with a paint showing high quantum efficiency enables exposure times of the order of milliseconds when using high-sensitivity CCD cameras. The response time of a TSP *layer* is dependent upon the boundary conditions of the heat transfer in a specific application; the thermal diffusion time for a thin TSP coating is given by b^2/α_T, where b is the coating thickness and α_T the thermal diffusivity of TSP [7.224]. In general, the thermal diffusion time is much larger than the luminescent lifetime and therefore thermal diffusion limits the time response of temperature-sensitive paints.

Sensor and Measurement System

The principle of temperature-sensitive paint measurement is based on the *thermal quenching* process of the luminescence of the sensor molecules incorporated into a binder matrix. Luminescence is a general term for both fluorescence and phosphorescence and the emitting molecules are called *luminophores*. A luminophore is activated by absorption of photons of incident light in a certain wavelength range, bringing the molecule from the ground electronic to some excited electronic states. The excited electrons return to the ground state by a combination of radiative and radiationless processes and emission occurs due to the radiative process. The wavelength of the emitted light is shifted with respect to the excitation light, appearing at longer wavelengths (Stokes shift). Ruthenium complexes, for example, can be used as luminophores which are excitable by blue light (420–550 nm) and emit at (590–740 nm), i. e., red light (Fig. 7.46). Or europium complexes exist which can be excited around (340±10) nm (i. e., by UV light), showing emission around 615 nm.

The excited states of the luminophore can be deactivated by interaction with other components of the system. For example, they can be deactivated by collisions with oxygen molecules (*oxygen quenching*), which is the principle behind *pressure-sensitive paint* (PSP), described elsewhere in this book (Sect. 4.2.2). However, to enable oxygen quenching, the binder matrix has to be

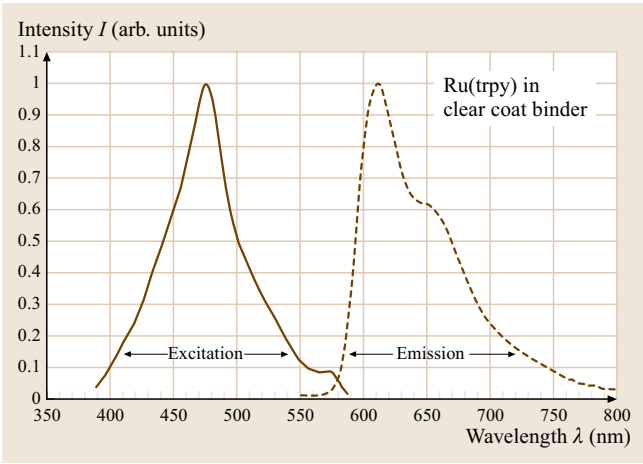

Fig. 7.46 Excitation and emission spectrum of cryoTSP based on Ru(trpy) as the sensor molecule, incorporated into a clear coat binder

penetrated by oxygen molecules, making it necessary to use a noncommercial, special binder that typically leads to a less smooth surface than for temperature-sensitive paint.

Another process for deactivation of excited states is so called *thermal quenching*: the quantum efficiency of luminescence decreases with increasing temperature because of the increased frequency of collisions. This means that the luminescent intensity of a TSP layer decreases with an increase in temperature, dark areas in an image meaning higher temperatures and bright areas meaning lower temperatures. This is in contrast to an IR result image, where high intensity denotes high temperature.

In comparison to PSP, the binder for TSP does not need to be permeable to oxygen, i. e., conventional, transparent binders like polyurethane work well. This gives the added benefit that the surface can be finished to high smoothness by polishing, which is important especially in cryogenic testing. On the other hand, TSP uses the same measurement system as PSP, i. e., same cameras and lamps (but maybe different optical filters) and the evaluation process of TSP images is nearly the same as for PSP (intensity or lifetime method).

To prevent fast temperature equilibration on metallic model surfaces by heat conduction, they have to be covered by a thermally insulating paint layer before applying the TSP coating. In addition, the color of this insulating layer should be white to serve as a screening layer, giving a more-homogenous intensity distribution and higher signal-to-noise ratio (the same holds true for PSP).

A modern TSP measurement system consists (besides the paint) of at least one scientific CCD camera with optics and an excitation light source. Using high-energy xenon flash lamps as illumination sources gives the benefit to choose excitation wavelengths by applying different filters, making *one lamp* the light source for *different luminophores*. Also (high-energy) LED arrays can be used for excitation, but with the restriction that only one wavelength range is available. For luminophores which have to be excited by UV light $< 360\,\text{nm}$ (i. e., europium complexes), the use of LEDs is hardly possible because of the present lack of efficient UV LEDs. However, this may change within the near future, as higher-power LEDs become available with their wavelength range extended to the shorter UV wavelengths (at the time of writing, 365 nm represents the short-wave limit for high-power LEDs).

To obtain a TSP thermogram of a surface using the intensity method, one has to form the ratio of two different images: a reference image taken at constant or known temperature distribution on the surface divided by a second image taken after the temperature distribution has changed somehow. With a prior measured temperature calibration for the TSP paint, one can determine absolute temperatures on the surface of interest. For example Fig. 7.47 shows the temperature variation along a line cut on the upper surface of a wing tested in the ETW cryogenic wind tunnel [7.225]. The wing image Fig. 7.47a shows the raw data of TSP intensity where inhomogeneous excitation light distribution is still seen (brighter in the mid-span area, less bright near root and tip). The resulting temperature field was evaluated by dividing the raw image Fig. 7.47a by a reference image at constant temperature. This results in the ratio image Fig. 7.47b. Line cuts within the temperature field of Fig. 7.47b are shown in Fig. 7.47c. In this example, the temperature difference between the laminar (bright areas) and turbulent part (dark grey areas) of the boundary layer was made large enough to be seen clearly in the raw image Fig. 7.47a. If the temperature difference is much smaller, it is hard to detect in the raw image but may nevertheless be clearly pronounced in the (somehow amplified) ratio image.

Some notes on the use of *intensity monitors* should be made. In pressure-sensitive paint (PSP) testing by means of the intensity method, it is common to use a *binary* paint that consists of the pressure-sensitive luminophore and a pressure-*insensitive* luminophore as an intensity monitor (often called a *reference dye*). Both are incorporated into an oxygen-permeable binder. By normalizing the pressure-sensitive emission light inten-

sity (selected by filter A) with the pressure-insensitive reading of the intensity monitor dye (selected by filter B), the resulting intensity distribution is independent of inhomogeneous light distribution caused by angular dependent excitation or by variations in paint thickness. Normally, these deviations are also canceled out by division of *wind-ON* and *wind-OFF* image of pressure-sensitive emission light only. But since the model may eventually move and deform between *wind-OFF* (no loading) and *wind-ON* (high loading) conditions, inhomogeneous intensity distribution is not canceled out completely in PSP testing. Hence, a reference dye (intensity monitor) is needed to attain high accuracy. Additionally, an intensity monitor accounts for absolute differences in excitation light intensity between *wind-ON* and *wind-OFF* image, caused by time fluctuations of the flash energy when using xenon flash lamps, or by varying excitation light sources in general.

In TSP testing, the reference and run images are usually taken under *wind-ON* conditions (tunnel is running) and a second luminophore for normalizing the TSP intensity is not strictly necessary. However, if the absolute excitation light intensity changes between the reference and run images, this can still lead to an error in the evaluated TSP temperature. Therefore, very stable light sources should be chosen (LED systems, xenon lamps with a feedback unit) when performing accurate temperature measurements by means of TSP without an intensity monitor. For transition detection it is sufficient to divide a reference image (stationary wind-tunnel conditions, temperature constant) by a run image (acquired during a temperature change in the flow) without calibration, since one is interested in a good enhancement of the transition lines rather than in absolute surface temperatures of laminar and turbulent regions on the wing.

7.4.2 Surface Heat Transfer Processes

For transition detection measurement in wind tunnels by means of TSP, a large enough temperature difference between areas of laminar and turbulent boundary layer states has to be established. If the naturally given difference in adiabatic wall temperature is too small to be seen with a temperature-sensitive paint (as is in cryogenic testing), the laminar-to-turbulent temperature difference has to be enhanced artificially [7.219]. There exist different methods for augmentation of the adiabatic wall temperature difference, and for all of them heat transfer from the wind-tunnel flow to the model substrate plays an important rule. Hence, before explaining the

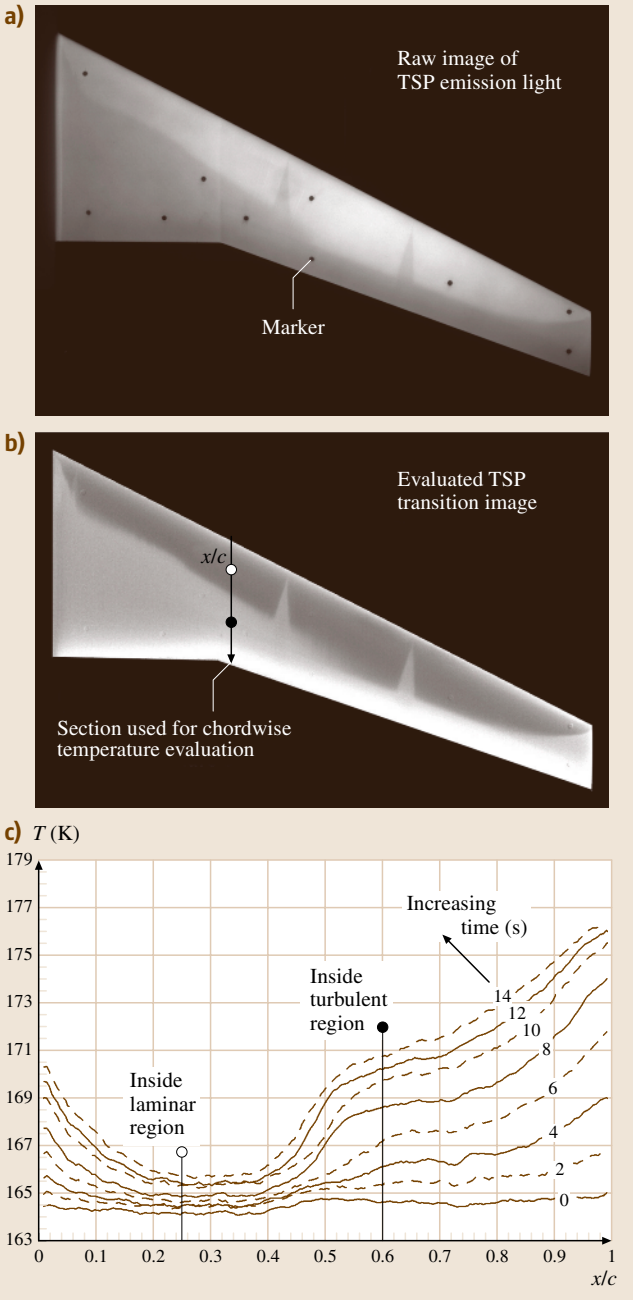

Fig. 7.47a–c Temperature distribution on line cuts crossing laminar and turbulent state of the boundary layer. Flow is from top to bottom. **(a)** Location of the line cut on upper wing surface. **(c)** Absolute temperature along line cuts at different time steps. T changes with time because of the changing flow temperature in the wind tunnel

various methods, some basic concepts of heat transfer shall first be mentioned. Three basic heat transfer processes take place near a solid wall and influence the thermal signature that is used to visualize the boundary-layer transition: heat radiation, heat conduction and heat convection.

Heat Transfer by Means of Radiation

All materials *radiate* thermal energy in amounts determined by their temperature, where the energy is removed by photons of light in the infrared and visible portions of the electromagnetic spectrum. Consider a wing section under specific test conditions in a wind tunnel, as shown in Fig. 7.48; $\dot{q}_{\mathrm{rad}}$ is the radiative heat flux per unit area (heat flux density) from the wing's surface, which can be written as

$$\dot{q}_{\mathrm{rad}} = \varepsilon\sigma T_{\mathrm{W}}^4 \,. \tag{7.40}$$

This represents the well-known Stefan–Boltzmann law, with T_{W} being the wall temperature, σ denotes the Stefan–Boltzmann constant ($\sigma = 5.6703\times10^{-8}$ W/m^2 K^4) and ε is the emissivity, a *surface* rather than a *material* property. The constant ε denotes the ratio of actual heat radiated by a body to the maximum possible heat radiation, i. e., the radiation that would occur for a certain temperature if the body were an idealized blackbody radiator. It is dependent on the material the body is made of, surface finishing (rough or shiny), and surface color. Fortunately, many technical surfaces have an ε in the range 0.92–0.98 (painted surfaces, wood, glass, carbon fiber- or glass-fiber-reinforced plastics) whereas blank metallic surfaces have ε of the order 0.05. For known ε, surface temperature distributions can be deduced from radiation measurements with the help of infrared (IR) cameras.

Equation (7.40) shows that the reading of an IR sensor scales with T^4, meaning that IR thermography is very useful at temperatures above 300 K but becomes difficult at cryogenic conditions. Moreover, an IR sensor must be cooler than the object under investigation so as not to be affected by its own heat radiation, which would be a strong source of noise. Therefore IR sensors or sensor matrices have to be cooled down with liquid nitrogen or Peltier elements to temperatures as low as 77 K to obtain high sensitivity and a high signal-to-noise ratio. In cryogenic testing, the sensor must be cooler than the object under investigation, i. e., a liquid-helium-cooled device has to be operated, since the flow is already near liquid-nitrogen temperatures.

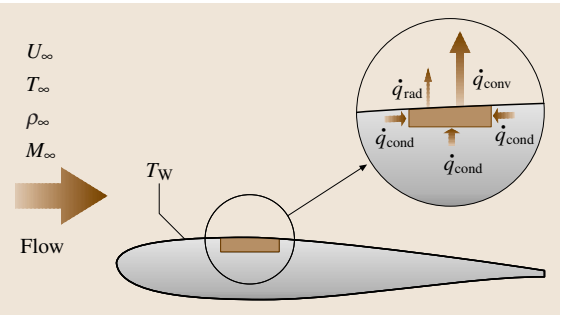

Fig. 7.48 Heat transfer processes on a wind-tunnel model's surface

Heat Transfer by Means of Conduction

Conduction is heat transfer by means of molecular or atomic movement (vibration) within a material (solid body, liquid, or gas) without any net motion of the material as a whole. Conduction is the only process which enables heat flux inside a wind-tunnel model if it is completely solid. The heat flux per unit area inside a solid material between two locations separated by the distance d is given by

$$\dot{q}_{\mathrm{cond}} = \frac{\lambda(T_{\mathrm{hot}} - T_{\mathrm{cold}})}{d} \,, \tag{7.41}$$

where the constant λ denotes the thermal conductivity of a model material (this is a simplified 1-D approach). Compared to radiation, where the absolute temperature itself determines the radiated heat flux, now the temperature difference between two locations is the scaling factor.

Heat Transfer Caused by Convection

Convection involves the transfer of heat by the motion and mixing of *macroscopic* portions of a fluid. The term natural, or *free*, convection is used if this motion and mixing is caused by density variations resulting from temperature differences within the fluid, whereas the term *forced* convection pertains motion and mixing caused by an outside force, as, for example, the flow driven by a wind-tunnel fan. Heat transfer by convection is more difficult to analyze than heat transfer by conduction because no single, constant property of the heat transferring medium (such as thermal conductivity λ) can be defined to describe this mechanism. Heat transfer by convection depends on parameters like fluid velocity, density, viscosity, turbulence level, surface roughness, geometrical parameters, type of flow (single or two phase) and state of flow (laminar or turbulent). In practice, analysis of heat transfer by convection is treated empirically (by direct observation and meas-

urement). For example, the heat transferred per unit area from a hot isothermal plate to a forced airstream is given by Newton's law

$$\dot{q}_{\text{conv}} = \alpha(T_{\text{W}} - T_{\infty}) \,, \tag{7.42}$$

where α is the (forced) convective heat transfer coefficient, which depends upon the physical properties of the fluid as well as on the physical situation, and which is different for free convection.

For convective heat transfer in wind-tunnel testing, the turbulent convective heat transfer coefficient α is of the order of several 100. It is related to the plate's Nusselt number Nu and also depends on the Prandtl number Pr. For zero pressure gradient ($\partial p/\partial x = 0$), $Pr = 1$, and $T_{\text{W}} =$ constant there is a linear relationship between the wall friction coefficient c_{f}' and the heat transfer coefficient α (Reynolds analogy):

$$\alpha = \frac{1}{2} c_{\text{f}}' u \frac{\lambda}{\nu} \,, \tag{7.43}$$

where u represents the flow velocity outside the boundary layer, and ν the kinematic viscosity of the medium. Since the wall friction in the turbulent region of the boundary layer is around 10 times higher than in the upstream laminar region, there will be different temperatures in laminar and turbulent portions of a boundary layer, when convective cooling or heating of the model by the incoming flow occurs.

7.4.3 Temperatures in Laminar and Turbulent Boundary Layer

The main principle of transition detection using thermographic methods is visualization of a temperature difference between the laminar and turbulent state of a model's boundary layer (BL) that is undergoing transition. This temperature difference occurs either naturally, caused by the different recovery factors for laminar and turbulent boundary-layer flow, or it has to be added artificially using the method of *temperature steps*, or using electrical external or internal heating of the surface. IR thermography, because of the available high-sensitivity sensors (temperature resolution up to 0.02 K), may be able to detect the small temperature differences created by the recovery process in warm, transonic wind tunnels or in flight measurements. However, if the model or wing has a blank metallic and/or shiny surface (i. e., the emissivity ε is very small and the surface can mirror radiation from heat sources surrounding the model or wing), a special paint or foil must be applied to improve emissivity. In pressure driven blow-dow type wind tunnels a temperature difference naturally occurs because flow temperature rapidly decreases due to the expension of the gas at the beginning of the test run. For transition detection measurement in continuously driven, cryogenic wind tunnels, one needs to perform an *artificial enhancement* of the laminar-to-turbulent temperature difference because there is only a small temperature difference caused by the recovery factor.

Temperature Differences Arising from the Recovery Factor

When the fluid is slowed down from its free-stream velocity U_{∞} to $U = 0$ at the wall it *recovers* some heat energy from kinetic energy, which leads to an increase in temperature on a model's surface. If the surface (for example the upper side of a wing) is thermally well insulated, approximately no heat flux occurs between model and boundary layer ($\dot{q}_{\text{cond}} = 0$), and the increase in temperature within the boundary layer leads to an increased, so-called adiabatic wall temperature (or recovery temperature) T_{aw}. The change in wall temperature is described by the recovery factor R, which depends on the physical properties of the fluid (i. e., air in common wind tunnels and nitrogen (N_2) in cryogenic wind tunnels), and on flow conditions. The adiabatic wall temperature can be written [7.226, 227]

$$T_{\text{aw}} = T_{\infty} + R\frac{U_{\infty}^2}{2c_{\text{p,air}}} = T_{\infty}\left(1 + R\frac{\gamma - 1}{2}M_{\infty}^2\right) \,, \tag{7.44}$$

with $C_{\text{p,air}}$ being the specific heat of air at constant pressure (which is very similar to $C_{\text{p},N2}$), γ the isentropic exponent and M_{∞} denotes the Mach number of the undisturbed wind tunnel flow. γ is nearly constant at lower temperatures or pressures and can be set to 1.4 without much lack of accuracy. It is obvious that there is a different recovery factor for a laminar boundary layer in comparison to a turbulent boundary layer and the two can be estimated to $R_{\text{lam}} \approx 0.84$ and $R_{\text{tur}} \approx 0.9$, respectively (for a Prandtl number of $Pr = 0.71$). Thus, the difference in adiabatic wall temperature on a wing's surface which is subject to a partly laminar and partly turbulent boundary layer can be written as:

$$\begin{aligned} \delta T_{\text{aw}} &\equiv T_{\text{aw,tur}} - T_{\text{aw,lam}} \\ &= T_{\infty}\,(R_{\text{tur}} - R_{\text{lam}})\left(\frac{\gamma - 1}{2}M_{\infty}^2\right) \\ &\approx 0.012 T_{\infty} M_{\infty}^2 \,. \end{aligned} \tag{7.45}$$

An estimate for δT_{aw} is shown in Table 7.5 for different M_{∞} and T_{∞}. Note that here δT_{aw} represents an up-

Table 7.5 Maximum possible adiabatic wall temperature differences caused by the recovery factor

M_∞	T_∞ (K)	δT_{aw} (K)
0.2	1000	0.48
0.2	300	0.15
0.2	100	0.05
0.8	1000	7.7
0.8	300	2.3
0.8	100	0.77

per limit for the possible temperature difference, which holds true only for a perfectly insulated model surface. Even though the model surface may be well insulated, true adiabatic conditions can never be reached, i. e., a certain amount of heat exchange between flow and model will always take place. Therefore, real δT values are smaller than shown in Table 7.5.

Temperature Difference Produced by the Method of Temperature Steps

Since in boundary layer flow the convective heat transfer coefficient α_{tur} is larger than α_{lam}, a temperature *change* in the outer flow will be seen faster on the surface underneath the turbulent boundary layer, leading to a temperature difference δT between turbulent and laminar regions for a certain amount of time. When the change stops, this difference will vanish in time because of heat exchange by internal conduction and outer convection. There is competition between the generation of a temperature difference by means of convective heat transfer (if the flow temperature differs from the model temperature) and internal equilibration by conduction. Therefore, a metallic model must be thermally well insulated against the flow, for example by the use of thermally insulating paint or foils.

More effective is the use of non-metallic models, manufactured from carbon-fiber- or glass-fiber-reinforced plastic, wood, glass or suchlike (note however that glass or wood models are rarely found in modern wind-tunnel testing). In practice, one has to apply the temperature change in the oncoming flow quickly (if possible), this being denoted a *temperature step*, which can either be positive or negative. In cryogenic testing it is very easy to generate a temperature step by increasing the amount of (normally continuously) injected nitrogen, leading to a negative gradient $-\mathrm{d}T/\mathrm{d}t$ [7.225]. Furthermore one can stop the continuous injection of nitrogen, leading to an increase in flow temperature $+\mathrm{d}T/\mathrm{d}t$, caused by the heat input of the fan (at least for the higher Mach numbers > 0.4).

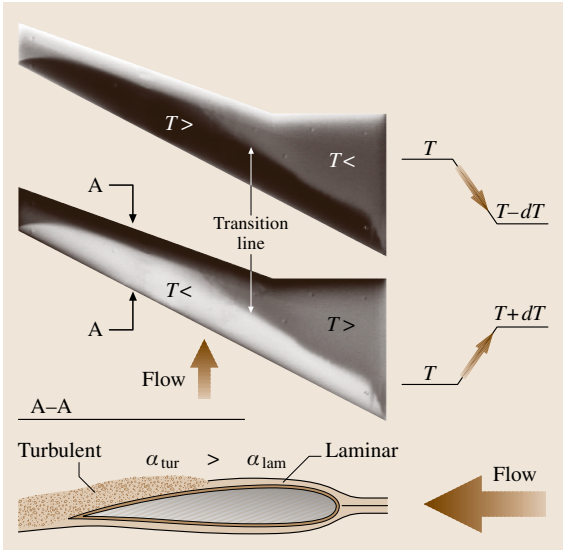

Fig. 7.49 Method of temperature steps for transition detection measurement by means of TSP, suitable for cryogenic wind tunnels

By having a sufficiently large temperature difference δT between turbulent and laminar regions on a model surface, the transition line can be seen as the borderline between light and dark areas in the evaluated TSP image (Fig. 7.49).

Temperature Differences Produced by Electrical Heating

Another method for artificially generating temperature differences between model surface and flow is to heat up the model or single parts of a model (for example, the wing, or slats and flaps). This can be achieved by classical heating foils, where the heating elements of thin electrically resistant material (thin copper strips) are embedded in Kapton foils that can be mounted on, or beneath but close to the surface. Figure 7.50 shows the application of such heating foils mounted in the leeward side of a half-model slat. Transition detection on this slat was performed successfully in a low speed, cryogenic wind tunnel [7.228].

Nowadays the highly developed technology of carbon-fiber-reinforced plastic (CFK) has enabled the use of more-homogeneous and more-efficient heating layers applicable to models made of glass-fiber-reinforced plastic or of carbon-fiber-reinforced plastic [7.229]. In the case of carbon fiber, a single sheet of carbon with electrical connections which function as an electrical heater is laminated with the other sheets

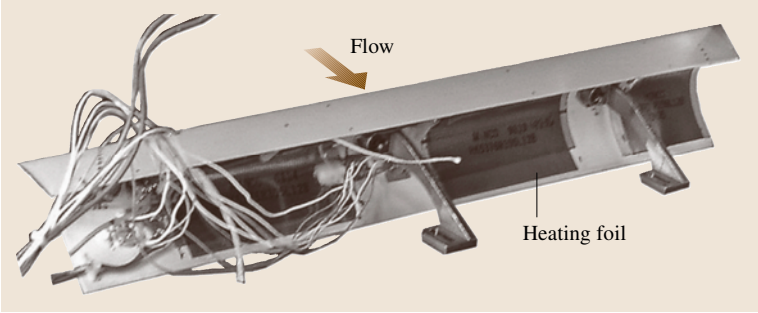

Fig. 7.50 Conventional heating foils implemented into the slat of a half model. Opposite side of the slat is painted with TSP

of carbon fiber in such a way that the carbon sheet has a very small distance to the surface to ensure that most of the heat is conducted to the surface and not to the inner parts of the model. Figure 7.51 shows a schematic drawing of the application of a heating layer of carbon inside a wing section. Thermographic investigation of the surface temperature distribution of such models equipped with carbon heating sheets has also shown very good homogeneity of the surface temperature for large heated areas and high temperatures [7.229].

Additional Methods for Establishing a Boundary-Layer Temperature Difference

In some cryogenic facilities a temperature difference can be established by injecting warm, gaseous nitrogen in addition to the continuously injected, liquid nitrogen. Furthermore, an artificial temperature difference can also be established by adjusting the complete model to a temperature different from the flow temperature. This can be realized by heating or cooling the model outside the test section (in a separate chamber) and moving it to the test section just before acquisition of transition images begins (model transport method [7.228]). Although this enables the implementation of positive as well as negative temperatures difference betweens model and flow, it is hardly practicable in most industrial-scale wind tunnels since it takes some time to move the model. Thermographic images may thereby become rather expensive by wasting tunnel time for model transport. Moreover, special care has to be taken to prevent humidity from entering the test section with the model during transport. However, sometimes this is the only method available if temperature steps cannot be generated some other way and the existing model cannot be equipped with heating foils.

Some workers have used special infrared radiators that can be used for heating the model from outside, but, in general, and compared with the aforementioned methods, these radiators produce only a small increase in temperature with poor homogeneity and less stability in time [7.229].

Finally, some blow-down wind tunnels exist (for example the Ludwieg-type cryogenic wind tunnel DNW-KRG in Göttingen), which can provide a suitably large temperature step within milliseconds. Since the flow is driven by a large pressure difference between a storage tube and a low-pressure vessel, the gas (nitrogen) expands quickly when the so-called *fast shutter valve* is opened. Thus, a temperature drop is created automatically during operation making such wind tunnels well suited for transition detection by means of TSP, also at ambient temperatures.

Influence of Temperature Difference on Boundary Layer Instability

It is well known that a temperature gradient inside the boundary layer changes the stability properties, at least for the Tollmien–Schlichting (TS) instability. This property was used as a method for laminar flow control by

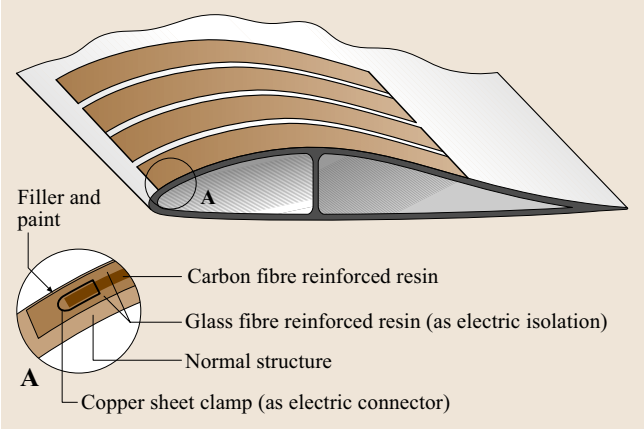

Fig. 7.51 Implementation of carbon-fiber-reinforced resin heating layer into a carbon-fiber-reinforced plastic model (courtesy K. de Groot)

cooling a model in air, or heating a model in water. Following *Reshotko* [7.230], as cited by *Saric* [7.231], the boundary-layer equation near the wall can be written as

$$\mu \frac{\partial^2 u}{\partial y^2} = \rho V_0 \frac{\partial u}{\partial y} + \frac{\mathrm{d}p}{\mathrm{d}x} - \frac{\mathrm{d}\mu}{\mathrm{d}T}\frac{\partial T}{\partial y}\frac{\partial u}{\partial y}\,, \quad y \approx 0\,, \tag{7.46}$$

with u being the flow velocity inside the boundary layer, y the wall normal coordinate, p the pressure, and μ the dynamic viscosity. A fuller boundary layer (i. e., a more-negative $\partial^2 u/\partial y^2$) usually results in lower disturbance growth so that anything that makes the left-hand side of (7.46) more negative will stabilize the boundary layer [7.231]. Thus, model cooling in air ($\partial T/\partial y > 0, \partial\mu/\partial T > 0$), which is equivalent to heating the flow, will result in a more-stable boundary layer. On the other hand, cooling the flow (or heating the model) makes the boundary layer more unstable. This fact has to be taken into account when performing transition detection by the method of temperature steps, especially when using negative steps $-\mathrm{d}T/\mathrm{d}t$ in the flow or using electrical heating of the model.

In cryogenic wind tunnel testing in ETW, it is possible to realize $+\mathrm{d}T/\mathrm{d}t$ as well as $-\mathrm{d}T/\mathrm{d}t$ with the same rate of heating or cooling for Mach numbers above 0.4. In a cryoTSP test campaign in 2003, the mentioned influence of temperature steps was investigated, leading to rule-of-thumb criteria for a suitable selection of $\mathrm{d}T/\mathrm{d}t$ [7.225]. Additionally, during a temperature step the Reynolds number changes slightly (caused by the changing viscosity) and it can be observed that the location of transition moves in time during image acquisition, at least for Reynolds numbers in the range where x/c_{trans} strongly depends on Re(Re < 3Mio).

7.4.4 Transition Detection by Means of TSP

Infrared thermography is well established in flight tests, and may be easier to use in warm wind tunnels, but TSP is to be recommended for cryogenic testing. Hence, the term *cryoTSP* has become established. Nevertheless, since some industrial wind tunnels are already equipped with a PSP system, it may also be a good opportunity to perform transition detection with the TSP technique in a *warm* wind tunnel by using the same cameras and lamps as for PSP but different filter for lamps together with a TSP suited for the wind-tunnel temperature range. The following discussion on cryoTSP also holds in principle for TSP at higher temperatures.

At the end of this section, results of transition detection measurements obtained using the DLR mobile PSP/TSP system [7.225, 232] will be presented. A cryoTSP paint originally developed by the Japanese Aeronautics Exploration Agency (JAXA) (former National Aeronautics Laboratory (NAL) of Japan) was used [7.233]. Transition detection was performed [7.234, 235] in different, industrial cryogenic wind tunnels such as the European transonic wind tunnel (ETW), the pilot facility of ETW (PETW), the low-speed cryogenic wind tunnel of the German–Dutch wind tunnels in Cologne (DNW-KKK) or the cryogenic Ludwieg-tube wind tunnel in Göttingen (DNW-KRG).

Required Properties for TSP in Cryogenic Testing

It has to be stated that, in comparison to laboratory (small-scale) wind-tunnel testing, a cryoTSP suited for large-scale, industrial wind tunnels needs to have the following additional properties: *high luminescent intensity* (The intensity of excitation light varies inversely proportionally to the square of the distance between the model and the light source. To apply TSP in large-scale wind tunnels, the TSP formulation must provide very high brightness.); *coating robustness at cryogenic temperatures* (In general, polymer coating on a large metallic surface is subject to cracking when cooled down to cryogenic temperatures, or warmed up after the test. This is due to a large difference in thermal contraction between the TSP and the substrate, especially for aluminium models.); *smooth surface* (At cryogenic temperatures, boundary layers on model surfaces are very thin, especially in the leading edge region. To prevent premature transitions, surface roughness of the coating must be as small as possible.) JAXA has successfully optimized a cryoTSP with respect to these properties, this being tested in laboratory-scale wind tunnels beforehand [7.233]. The paint is based on a metal-organic compound (abbreviation Ru(trpy)) implemented into a polyurethane binder, and has a wide-band excitation and emission spectrum (Fig. 7.46).

Figure 7.52 shows a calibration curve for the cryoTSP used here in the range $100\,\mathrm{K} < T < 300\,\mathrm{K}$. At first glance, the calibration curve suggests that this TSP shows a nearly constant sensitivity in the range $110\,\mathrm{K} < T < 170\,\mathrm{K}$ and becomes less sensitive for $T > 170\,\mathrm{K}$. However, for transition detection things are different; the reason lies in the special technique of *temperature steps* used in cryogenic wind tunnels. When performing transition detection by the use of temperature steps, one starts at a given, constant flow temperature,

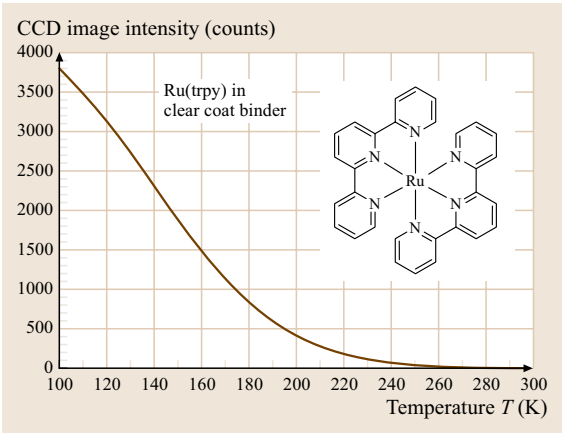

Fig. 7.52 Decrement of intensity with increasing temperature for Ru-based cryoTSP

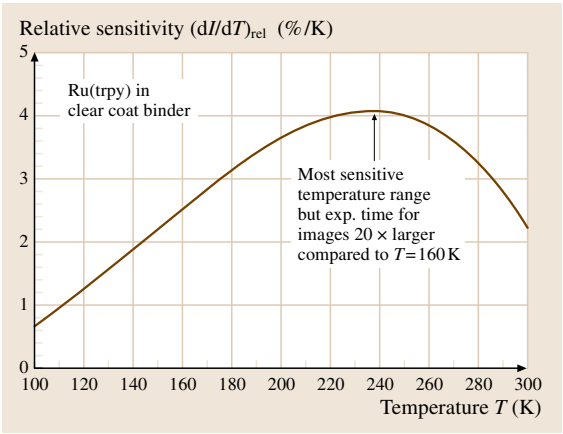

Fig. 7.53 Relative sensitivity for the used cryoTSP paint

say $T_{start} = 170\,K$. Then a positive step $+dT/dt$ of (say) 0.5 K/s is applied until the flow temperature increases to 180 K. No temperature smaller than 170 K for this working point exists, and there is no need to use the full dynamic range shown in Fig. 7.52, where the curve starts at 100 K. Exposure time of the camera, aperture of the objective lenses, flash frequency, or absolute intensity of the excitation light source can be adjusted in such a way that 3000 intensity counts are measured at 170 K, instead of 1000 counts at 170 K as given in Fig. 7.52 (12 bit dynamic range camera = 4095 intensity counts at maximum). This increases the steepness of the calibration curve for this working point, making the system more sensitive.

Thus, for transition detection by the method of temperature steps it is more convenient to refer to the *relative sensitivity* of the measurement system given by

$$\left(\frac{dI}{dT}\right)_{rel} = \left(\frac{dI(T)}{dT}\frac{1}{I(T)} \times 100\right) \quad [\%/K] \quad (7.47)$$

to get an estimate for the resolvable temperature differences at a given working point (I = intensity counts on CCD image, T = flow temperature). Figure 7.53 shows $(dI/dT)_{rel}$ for the cryoTSP used here, which exhibits its highest relative sensitivity around 240 K. This fact has been amply demonstrated in different cryogenic wind-tunnel tests using the JAXA paint, showing good transition images even at 240 K. However, the image exposure time for $T = 240\,K$ is around 20 times larger compared to that for 160 K (Fig. 7.52), which mostly limits the practical application range of this paint to $T < 240\,K$ in large, continuously driven, industrial wind tunnels such as ETW.

DLR has since improved the described cryoTSP by implementing a second luminophore into the paint, showing high sensitivity in the range $240\,K < T < 320\,K$ in parallel to high intensity [7.236]. This second, europium-based luminophore has to be excited by UV light that is clearly separated from the blue light necessary for excitation of the Ru(trpy) luminophore (working range: $100\,K < T < 240\,K$). On the other hand, the emitted wavelength of this europium complex is in the same range as emission light for Ru(trpy) ($600\,nm < \lambda_{em} < 650\,nm$). Using this two-component cryoTSP (2C-cryoTSP), it is possible to perform transition detection in the complete range $100\,K < T < 320\,K$ by the use of a single paint, with the same camera–filter assembly, but by changing the lamp filter, or by using two different lamps (for example xenon lamp with UV filter in addition to a blue high-power LED).

Especially on metallic wind-tunnel models, before applying the TSP it is necessary to spray a carrier paint which serves as a thermal insulation (thickness about 100 µm), reducing the heat flux from flow to model (or vice versa). Additionally, this paint should be white to serve as a screening layer for the TSP, giving a more homogenous background intensity distribution. The same screen layer can be used for IR measurement on a metallic model but must be different for liquid crystals, for instance, since they require a black background to absorb the light which penetrates the TLC layer.

Results of Transition Detection by cryoTSP

An example for transition detection on a full model 3D wing is shown in Fig. 7.54. This cryoTSP measurement [7.225, 234] was conducted in the ETW wind tunnel using a 12 bit dynamic range CCD camera with

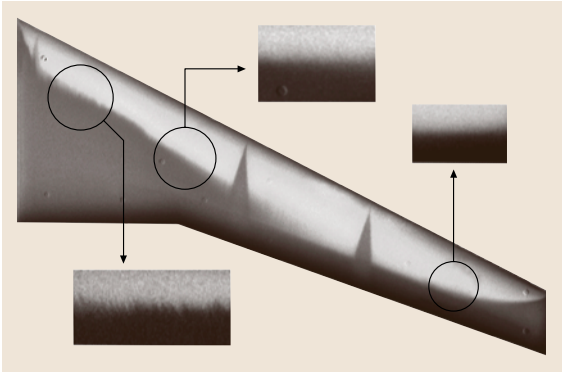

Fig. 7.54 Result image of transition detection on a full model wing tested in ETW. Re = 6 Mio, $M = 0.79$, $C_L = 0.5$, $T = 170$ K, tunnel pressure $p = 120$ kPa. Flow is from top to bottom

1280×1024 pixel^2 spatial resolution, and the method of temperature steps. Compared to IR images (typical resolution 320×240 pixel^2), the high spatial resolution of the CCD image allows us to highlight details of the transition line even when the complete wing is recorded by the camera as one image. In the transition image Fig. 7.54 turbulent areas are represented as dark regions and laminar areas appear bright.

Figure 7.55 shows a cryoTSP transition image of measurement in the DNW-KRG. Since this Ludwieg-type wind tunnel is operated as a blow-down wind tunnel, no artificial temperature step or model heating was applied, and high-quality result images could be gathered with a short exposure time of 0.4 s. Besides the transition line, the signatures of (strong) vortices located in the junction area of the main airfoil and the two cylindrical *noses* could be clearly seen.

Transition detection on a thick 2D profile is shown in Fig. 7.56. A carbon-fiber-reinforced plastic model was tested at low Mach numbers in the DNW-KKK low-speed cryogenic wind tunnel. Temperature *steps* were created by adding warm nitrogen to the tunnel flow.

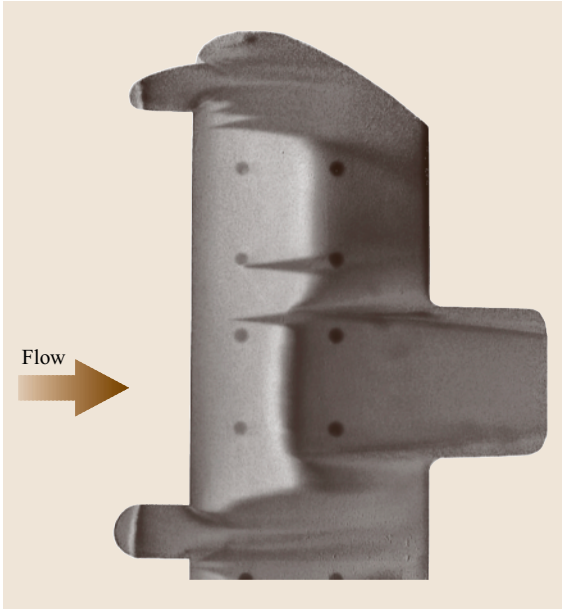

Fig. 7.55 Transition detection in the Ludwieg type DNW-KRG cryogenic wind tunnel. Re = 4 Mio, $M = 0.8$, $T = 200$ K, $p = 260$ kPa

Since carbon fiber has a low thermal conductivity and moderate heat capacity, results could be obtained even at the rather high temperature of $T = 258$ K and low attainable gradients by blowing in warm gas. The two examples shown in the figure refer to a 30×30 cm^2 area located in the mid-span region of a 2.40 m-long model (chord length = 30 cm). The left image in Fig. 7.56 shows transition for a negative angle of attack ($\alpha = -5°$), caused by a laminar separation bubble (bright vertical line in the middle). In the right image, transition takes place near the nose (sharp, vertical line), while flow separation can also be seen (rolling line in the middle). Note here (for $\alpha = 15°$): dark area = turbulent; small, somewhat brighter area near nose = laminar; bright area to the right = separated flow. The darker area near the

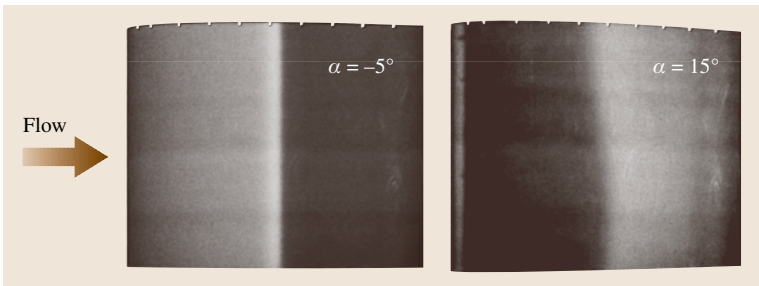

Fig. 7.56 TSP result images of a thick 2-D wing tested in the DNW-KKK wind tunnel. Re = 2.5 Mio, $M = 0.25$, $T = 258$ K, $p = 100$ kPa

nose in the left image in Fig. 7.56 ($\alpha = -5°$) indicates a more-effective heating here (flow was warmer than model). This is caused by a higher wall shear stress near the leading edge because of the thin boundary layer. The same holds true for the dark leading edge area in Fig. 7.54.

Finally, Fig. 7.57 shows a result of transition detection on a half model slat, tested at low Mach numbers in the DNW-KKK cryogenic wind tunnel [7.228]. We applied the heating foil method to establish a temperature difference between flow and slat (Fig. 7.50). Nevertheless the signatures of the three heating foils can still be seen in the TSP image (Fig. 7.57b), the transition line being clearly visible as the borderline between the darker, laminar region near the leading edge and the brighter turbulent region downstream. Here, the turbulent part of the boundary layer is cooled by the flow, thus appearing brighter in the image. The laminar *breakthrough* on the bottom part of the slat in Fig. 7.57b is caused by an upstream strake mounted on the model engine.

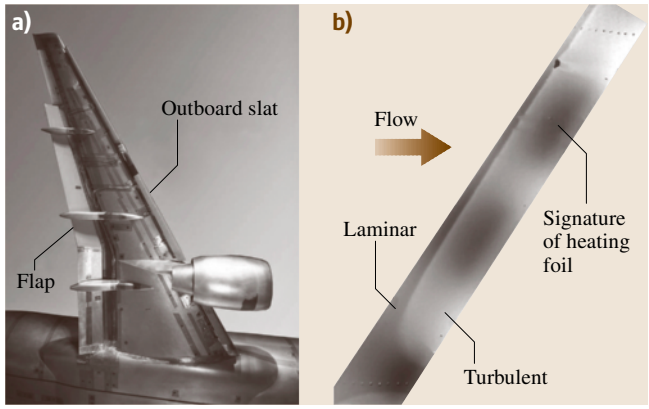

Fig. 7.57a,b Transition detection on high-lift devices in half model testing in DNW-KKK. Re = 2 Mio, $M = 0.18$, $T = 205$ K, $p = 100$ kPa. **(a)** Half model prepared for test. **(b)** Transition patterns on inner part of the outboard slat (seen in the middle of **(a)**)

7.4.5 Comparison with Other Methods

As already mentioned, other well-established thermographic methods such as infrared thermography (IRT) or liquid-crystal thermography (TLC) can be also used for transition detection. The benefits and drawbacks of the various methods are presented in Table 7.6 (the method of thermographic phosphors (TPT) was included in the general classification of TSP). Pros and cons are listed with respect to their use in large, industrial wind tunnels. However, certain drawbacks in large-scale testing may not necessarily also be the case in laboratory-scale testing. This should be kept in mind.

The features of the different methods were compared primarily with respect to their use as a transition detection tool in Table 7.6. Their usefulness with respect to absolute temperature measurement was not analyzed in detail, since for transition detection all methods do not require a sensor calibration. However, the suitability for absolute temperature measurement is strongly related to temperature difference measurements used in transition detection. Moreover, thermographic methods can be used for the measurement of (conductive and convective) heat fluxes and wall shear stresses (because of the Reynolds analogy). The suitability of the different methods for such measurements has not been treated here.

The frame rates mentioned in the table have to be considered as *typical* image frequencies of the thermography *system*. For example, modern focal-plane array IR cameras typically have frame rates of 50 Hz, i. e., they operate at video frequency. However, by binning of image pixels their frame rate can be increased up to about 500 Hz. 12 bit dynamic range CCD cameras typically used for the TSP method offer frame rates of around 10 Hz, which may be extended to around 20 Hz by binning of the CCD pixels. In large wind tunnels, exposure times usually are greater than 0.1 s (i. e., frame rates < 10 Hz result) caused by the large distances between the lamp/camera and model. The lifetime of the TSP luminophores is of the order of microseconds but incorporated into a polyurethane binder, the response time of a TSP *layer* is of the order of 5–20 ms (depending on the thickness). The response time for thermographic liquid crystals is < 6 ms but incorporated into paint or polymer it is around 100–200 ms, thus limiting the frame rate for TLC in the table to 5 Hz.

Further development of these methods is rapid and improvements in temperature sensitivity, ease of use, absolute temperature range, bandwidth, and spatial resolution will be made in the future. For example, to the author's knowledge, chemists in the UK are performing research for liquid crystals applicable in the cryogenic temperature range. However, since LCs available today are not suitable for cryogenic temperatures, their useful temperature range starts at $-30\,°C$ in Table 7.6. Future IR cameras will have spatial resolution comparable to today's standard CCD cameras, in addition to increased frame rates. However, they will still be rather expensive. In the field of temperature-sensitive paint, DLR, for example, will further improve the existing cryoTSP formulation and will develop new TSPs for warm wind tunnels and turbine testing at ambient temperatures.

Table 7.6 Comparison of different methods for thermographic imaging in wind tunnel testing. (IRT: infrared thermography, TSP: temperature-sensitive paint, TPT: thermographic phospor thermometry, TLC: thermochromic liquid crystals, NB: narrow band, WB: wide band)

Method	Principle	Operation range (K)	Bandwidth (K)	Typical frame rate	Max. resolution (K)	Suitability for transition detection	Benefits	Drawbacks
IRT	Detection of radiated heat	200–1400	≈ 200	50 Hz	0.02	• Good in ambient and high temperature testing • Standard cameras not suitable for cryogenic testing (< 200 K)	• Ready to use in most applications • No surface preparation for nonmetalic models necessary • Various cameras available • Good temperature sensitivity without calibration • High temperature and time resolution	• IR system comparatively expensive • Special optics, windows and cameras necessary • Small spatial resolution
TSP (incl. TPT)	Change of luminescent light intensity and lifetime of fluorescence/ phosporescence	80–2000	≈ 100	10 Hz	0.1	• Good for cryogenic testing and high temperature testing (using phospors) • Not much used at ambient temperatures	• Covers all temperatures given in wind tunnel testing • High spatial resolution • No *special* optics, windows or cameras necessary • Same equipment as for PSP can be used • Very smooth surface finishing possible	• Application of paint layer needed • Less temp. resolution compared to IRT • Need for excitation light source and filters for lamp and camera
TLC	Color change of scattered light	240–390	0.5–2 (NB) 5–30 (WB)	5 Hz	0.1	• At ambient conditions with small changes in absolute flow temperatures	• Various TLC formulations available • Excitation with white light • No special optics, windows or cameras necessary	• Relatively small bandwidth • Sensitive to illumination and viewing angle

Finally, progress in the development of modern, high-sensitivity, high-dynamic-range CCD cameras as well as in high-intensity excitation light sources (for example high-energy visible-range LEDs and UV LEDs) will expand the application range for thermographic imaging by means of TSPs.

References

7.1 G.M. Carlomagno: Heat transfer measurements by means of infrared thermography. In: *Measurement Techniques VKI Lect Series 1993-05 Rhode-Saint-Genese* (VKI, Rhode-Saint-Genese 1993) pp. 1–114

7.2 S.M.J. Straley: Physics of liquid crystals, Rev. Mod. Phys. **46**(4), 617–704 (1974)

7.3 P. Bonnett, T.V. Jones, D.G. Donnell: Shear-stress measurement in aerodynamic testing using cholesteric liquid crystals, Liquid Cryst. **6**, 271–280 (1989)

7.4 S.A. Hippensteele, L.M. Russell, F.S. Stepka: Evaluation of a method for heat transfer measurements and thermal visualisation of a heater elements and liquid crystals, Trans. ASME **105**, 184–189 (1983)

7.5 D.K. Hollingsworth, A.L. Boehman, E.G. Smith, R.J. Moffat: Measurement of temperature and heat transfer coefficient distributions in a complex flow using liquid crystal thermography and true-color image processing, ASME J. Heat Transfer **123**, 35–42 (1989)

7.6 J.K. Hay, D.K. Hollingsworth: A comparison of trichromic systems for use in the calibration of polymer-dispersed thermochromic liquid crystals, Exp. Thermal Fluid Sci. **12**, 1–12 (1996)

7.7 H. Babinsky, J.A. Edwards: Automatic liquid crystal thermography for transient heat transfer measurements in hypersonic flow, Exp. Fluids **21**, 227–236 (1996)

7.8 J. Stasiek: Thermochromic liquid crystals and true color image processing in heat transfer and fluid-flow research, J. Heat Mass Transfer **33**, 27–29 (1997)

7.9 R.T. Kukreja, S.C. Lau: Distribution of local heat transfer coefficient on surfaces with solid and perforated ribs, Enhanced Heat Transfer **5**, 9–21 (1998)

7.10 D.R. Sabatino, T.J. Praisner, C.R. Smith: A high-accuracy calibration technique for thermochromic liquid crystal temperature measurements, Exp. Fluids **28**, 497–505 (2000)

7.11 T.J. Praisner, D.R. Sabatino, C.R. Smith: Simultaneously combined liquid crystal surface heat transfer and PIV flow-field measurements, Exp. Fluids **300**, 1–10 (2001)

7.12 W. Hiller, T.A. Kowalewski: Simultaneous measurement of the temperature and velocity fields in thermal convective flows. In: *Flow Visualization IV*, ed. by C. Veret (Hemisphere, Paris 1987) pp. 617–622

7.13 W.J. Hiller, S. Koch, T.A. Kowalewski: Three-dimensional structures in laminar natural convection in a cube enclosure, Exp. Therm. Fluid Sci. **2**, 34–44 (1989)

7.14 W.J. Hiller, S. Koch, T.A. Kowalewski, D.G. de Vahl, M. Behnia: Experimental and numerical investigation of natural convection in a cube with two heated side walls. In: *Proc. of IUTAM Symp.*, ed. by H.K. Moffat, A. Tsinober (Cambridge Univ. Press, Cambridge 1990) pp. 717–726

7.15 D. Dabiri, M. Gharib: Digital particle image thermometry: The method and implementation, Exp. Fluids **97**, 77–86 (1991)

7.16 H.G. Park, D. Dabiri, M. Gharib: Digital particle image velocimetry/thermometry and application to the wake of a heated circular cylinder, Exp. Fluids **30**, 327–338 (2001)

7.17 W.J. Hiller, S. Koch, T.A. Kowalewski, P. Mitgau, K. Range: Visualization of 3-D natural convection. In: *Proc. 6th Int. Symp. Flow Visualization*, ed. by Y. Tanida, H. Miyashiro (Springer, Berlin, Heidelberg 1992) pp. 674–678

7.18 W.J. Hiller, S. Koch, T.A. Kowalewski, F. Stella: Onset of natural convection in a cube, Int. J. Heat Mass Transfer **36**, 3251–3263 (1993)

7.19 S. Koch: *Berührungslose Messung von Temperatur und Geschwindigkeit in freier Konvektion, Dissertation*, Mitteilungen aus dem MPI, Vol. 108 (Univ. Göttingen, Göttingen 1993)

7.20 T.A. Kowalewski, A. Cybulski, M. Rebow: Particle image velocimetry and thermometry in freezing water. In: *8th Int. Symp. Flow Visualization*, ed. by G.M. Carlomagno, I. Grant (ODE, Edinburgh 1998) pp. 24.1–24.8, CD ROM

7.21 K. Range: *Temperaturmessungen auf den Innenwänden eines Konvektionsbehälters mit Flüssigkristallen, Diplom*, MPIFS Bericht, Vol. 101 (Univ. Göttingen, Göttingen 1992)

7.22 W.J. Hiller, S. Koch, T.A. Kowalewski: Simultane Erfassung von Temperatur- und Geschwindigkeitsfeldern in einer thermischen Konvektionsströmung mit ungekapselten Flüssigkristalltracern. In: *2D-Meßtechnik DGLR-Workshop DGLR-Bericht 88-04* (DGLR, Bonn 1988) pp. 31–39, in German

7.23 E. Fornalik, Y. Yamamoto, W. Chen, K. Nakabe, K. Suzuki: Visualization of heat transfer enhancement regions modified by the interaction of inclined impinging jets into crossflow. In: *Image Processing Methods in Applied Mechanics Euromech 406 IPPT Reports 4/1999*, ed. by T.A. Kowalewski, J. Kompenhans, W. Kosinski (IPPT PAN, Warsaw 1999) pp. 95–98

7.24 T.A. Kowalewski, M. Rebow: Freezing of water in the differentially heated cubic cavity, Int. J. Comp. Fluid Dyn. **11**, 193–210 (1999)

7.25 T. Michalek, T.A. Kowalewski: Experimental model of mould filling flow. In: *Eurotherm 69 Heat and Mass Transfer in Solid-Liquid Phase Change Processes*, ed. by B. Šarler, D. Gobin (Polit. Nova Gorica, Lubljana 2003) pp. 61–68

7.26 T. Michalek, T.A. Kowalewski, B. Saler: Natural convection for anomalous density variation of water – numerical benchmark, Prog. Comput. Fluid Dyn. **5**, 158–170 (2005)

7.27 M. Giangi, F. Stella, T.A. Kowalewski: Phase-change problems with free convection: fixed grid simulation, Comp. Vis. Sci. **2**, 123–130 (1999)

7.28 M. Giangi, T.A. Kowalewski, F. Stella, E. Leonardi: Natural convection during ice formation: numerical simulation versus experimental results, Comp. Assisted Mech. Eng. Sci. **7**, 321–342 (2000)

7.29 J. Banaszek, Y. Jaluria, T.A. Kowalewski, M. Rebow: Semi-implicit FEM analysis of natural convection in freezing water, Num. Heat Transfer A **36**, 449–472 (1999)

7.30 T.A. Kowalewski, A. Cybulski: Experimental and numerical investigations of natural convection in freezing water, Proc. Int. Conf. Heat Transfer Change of Phase, Mechanics **61**(2), 7–16 (1996)

7.31 T.A. Kowalewski, A. Cybulski: Natural convection with phase change, IPPT Rep. **8**, 1–58 (1997), (in Polish)

7.32 A.Y. Gelfgat, P.Z. Bar-Yoseph, A. Solan, T.A. Kowalewski: An axisymmetry breaking instability of axially symmetric natural convection, Int. J. Trans. Phenomena **1**, 173–190 (1999)

7.33 C. Abegg, D.G. de Vahl, W.J. Hiller, S. Koch, T.A. Kowalewski, E. Leonardi, G.H. Yeoh: Experimental and numerical study of three-dimensional natural convection and freezing in water. In: *Proc. 10th Int. Heat Transfer Conf.*, Vol. 4, ed. by G.F. Hewitt (Taylor Francis, New York 1994) pp. 1–6

7.34 T.A. Kowalewski, A. Cybulski, T. Sobiecki: Experimental model for casting problems. In: *Computational Methods and Experimental Measurements*, ed. by Y.V. Esteve, G.M. Carlomagno, C.A. Brebia (WIT, Southampton 2001) pp. 179–188

7.35 K. Dekajlo, T.A. Kowalewski, H.J.S. Fernando: Experiments on up-slope to down-slope transition in an inclined box filled with water. In: *ICTAM04 CD-ROM Proceedings IPPT PAN*, ed. by W. Gutkowsky, T.A. Kowalewski (Springer, Dordrecht 2004)

7.36 T.A. Kowalewski: Experimental validation of numerical codes in thermally driven flows. In: *Advances in Computational Heat Transfer*, ed. by G.D. de Vahl, E. Leonardi (Begel House, New York 1998) pp. 1–15

7.37 A. Schulz: Infrared thermography as applied to film cooling of gas turbine components, Meas. Sci. Technol. **11**, 948–956 (2000)

7.38 W.P. Dixon, P. Czysz: The use of thermographic phosphors for heat transfer measurement in hypersonic wind tunnel. In: *Society of Photo-Optical Engineers 11th Annual Symposium* (1966)

7.39 G. Meyers, J. Van der Geest, J. Sanborn, F. Davis: Comparison of advanced cooling concepts using color thermography. In: *AIAA 3rd Applied Aerodynamics Conf. AIAA Paper AIAA-85-1289* (1985)

7.40 E. Gartenberg, A.S. Roberts: Twenty-five years of aerodynamic research with infrared imaging, J. Aircr. **29**(2), 161–171 (1992)

7.41 J. Wendt: Infrared thermography. In: *The Second Joint Europe/US Short Course in Hypersonics* (1989)

7.42 M.F. Westby: *Heat transfer measurements using infrared thermography in rarefied flows*, Technical Memorandum W1 (Defense Research Agency, Farnborough 1992)

7.43 M. Martiny, R. Schiele, M. Gritsch, A. Schulz, S. Wittig: In situ calibration for quantitative infrared thermography, QIRT '96, Stuttgart, Eurotherm Seminar **50**, 3–8 (1996)

7.44 S.R. Sargent, C.R. Hedlund, P.M. Ligrani: An infrared thermography imaging system for convective heat transfer measurements in complex flows, Meas. Sci. Technol. **9**(12), 1974–1981 (1998)

7.45 V. Scherer, A. Pfeiffer, S. Wittig: *Bestimmung der Wärmeübergangszahlen in abgelösten Strömungen mit Hilfe einer Infrarotkamera*, DGLR Workshop, 2D-Meßtechnik (DGLR, Bonn 1988) pp. 245–253

7.46 V. Scherer, S. Wittig: The influence of the recirculating region: a comparison of the convective heat transfer downstream of a backward-facing step and behind a jet in a cross-flow. In: *ASME Winter Annual Meeting* (ASME, Fairfield 1989), Paper 89-GT-59

7.47 M. Martiny, A. Schulz, S. Wittig: Full coverage film cooling investigations: adiabatic wall temperatures and flow visualization. In: *Winter Annual Meeting* (ASME, Fairfield 1995), Paper 95-WA/HT-4

7.48 M. Martiny, A. Schulz, S. Wittig: Mathematical model describing the coupled heat transfer in effusion cooled combustor walls. In: *Int. Gas Turbine Aeroengine Congr. Exhibition* (ASME, Fairfield 1997), Paper 97-GT-329

7.49 C.R. Hedlund, P.M. Ligrani, H.-K. Moon, B. Glezer: Heat transfer and flow phenomena in a swirl chamber simulating turbine blade internal cooling, ASME Trans. J. Turbomachin. **121**(4), 804–813 (1999)

7.50 B. Sen, D.L. Schmidt, D.G. Bogard: Film cooling with compound angle holes: heat transfer, ASME Trans. J. Turbomachin. **118**(4), 800–806 (1996)

7.51 U.M. Yuki, D.G. Bogard, J.M. Cutbirth: Effect of coolant injection on heat transfer for a simulated turbine airfoil leading edge. In: *Int. Gas Turbine Aeroengine Congr. Exhibition* (ASME, Fairfield 1998), Paper 98-GT-431

7.52 M. Gritsch, A. Schulz, S. Wittig: Adiabatic wall effectiveness measurements of film cooling holes with expanded exits, ASME Trans. J. Turbomachin. **120**, 549–556 (1998)

7.53 M. Gritsch, A. Schulz, S. Wittig: Heat transfer coefficient measurements of film cooling holes with expanded exits. In: *Int. Gas Turbine Aeroengine Congr. Exhibition* (ASME, Fairfield 1998), Paper 98-GT-28

7.54 P.C. Sweeny, J.F. Rhodes: An infrared technique for evaluating turbine airfoil cooling designs. In: *Int. Gas Turbine Aeroengine Congr. Exhibition* (ASME, Fairfield 1999), Paper 99-GT-142

7.55 C.M. Bell, H. Hamakawa, P.M. Ligrani: Film cooling from shaped holes, ASME Trans. J. Heat Transfer **122**(2), 224–232 (2000)

7.56 T. Fukukawa, P.M. Ligrani: Transonic film cooling effectiveness from shaped holes on a simulated turbine airfoil, AIAA J. Thermophys. Heat Transfer **16**(2), 228–237 (2002)

7.57 S.Y. Won, N.K. Burgess, S. Peddicord, P.M. Ligrani: Spatially-resolved surface heat transfer for parallel rib turbulators with 45 degree orientations including test surface conduction analysis, ASME Trans. J. Heat Transfer **126**(2), 193–201 (2004)

7.58 R.G. Driggers, C. Webb, S.J. Pruchnic, C.E. Halford, E.E. Burroughs: Laboratory measurement of sampled infrared imaging system performance, Opt. Eng. **38**(5), 852–861 (1999)

7.59 T. Astarita, G. Cardone, G.M. Carlomagno: IR heat transfer measurements in a rotating channel, QIRT '96, Stuttgart, Eurotherm Seminar **50**, 147–152 (1996)

7.60 G. Cardone, T. Astarita, G.M. Carlomagno: Heat transfer measurements on a rotating disc. In: *5th Int. Symp. Transport Phenomena and Dynamics of Rotating Machinery A* (1994) pp. 663–672

7.61 F.P. Hindle, S.J. Carey, K. Ozanyan, D.E. Winterbone, E.E. Clough, H. McCann: Measurement of gaseous hydrocarbon distribution by a near-infrared absorption tomography system, J. Electron. Imaging **10**(3), 593–600 (2001)

7.62 I.S.I. Group Inc., SWI: Southwest Infrared, VideoTherm Camera Systems, 1521 Eastridge Dr. NE, Albuquerque, NM 87112-4508 USA (http://www.swinfrared.com)

7.63 AGEMA Infrared Systems, ENEA Embedded Technology, 12760 High Bluff Drive, San Diego, CA 92130 USA (http://www.enea.com/907.epibrw)

7.64 Flir Systems Inc., 25 Esquire Road, North Billerica, MA 01862 USA (http://www.flirthermography.com/contact/worldmap.asp)

7.65 P.M. Ligrani, M.M. Oliveira, T. Blaskovich: Comparison of heat transfer augmentation techniques, AIAA J. **41**(3), 337–362 (2003)

7.66 W.P. Stricker: Measurements of temperature in laboratory flames and practical devices. In: *Applied Combustion Diagnostics*, ed. by K. Kohse-Höinghaus, J.B. Jeffries (Taylor Francis, New York 2002)

7.67 N.M. Laurendeau: Temperature measurements by light-scattering methods, Prog. Energy Combust. Sci. **14**, 147–170 (1988)

7.68 R.W. Dibble, R.E. Hollenbach: Laser Rayleigh thermometry in turbulent flames, Proc. Combust. Inst. **18**, 1489–1499 (1981)

7.69 J.N. Forkey, N.D. Finkelstein, W.R. Lempert, R.B. Miles: Demonstration and characterization of filtered Rayleigh scattering for planar velocity measurements, AIAA J. **34**, 442–448 (1996)

7.70 D. Hoffman, K.-U. Münch, A. Leipertz: Two-dimensional temperature determination in sooting flames by filtered Rayleigh scattering, Opt. Lett. **21**, 525–527 (1996)

7.71 R.B. Miles, J.N. Forkey, W.R. Lempert: Rayleigh scattering measurements in supersonic/hypersonic facilities, AIAA Paper **92-3894** (1992)

7.72 R.S. Barlow, C.D. Carter, R.W. Pitz: Multiscalar diagnostics in turbulent flames. In: *Applied Combustion Diagnostics*, ed. by K. Kohse-Höinghaus, J.B. Jeffries (Taylor Francis, New York 2002) pp. 384–407

7.73 D.F. Marran, J.H. Frank, M.B. Long, S.H. Stårner: Intracavity technique for improved Raman/Rayleigh imaging in flames, Opt. Lett. **20**, 791–793 (1995)

7.74 G.G. Stokes: *Mathematical and Physical Papers* (Cambridge Univ. Press, Cambridge 1880)

7.75 D.A. Long: *The Raman Effect: A Unified Treatment of the Theory of Raman Scattering by Molecules* (Wiley, New York 2002)

7.76 D. Geyer: *1D Raman/Rayleigh experiments in a turbulent opposed-jet*, Ph.D. Thesis (TU Darmstadt, Darmstadt 2004)

7.77 K. Kohse-Höinghaus, J.B. Jeffries (Eds.): *Applied Combustion Diagnostics* (Taylor Francis, New York 2002)

7.78 T. Landenfeld, A. Kremer, E.P. Hassel, J. Janicka, T. Schäfer, J. Kazenwadel, C. Schulz, J. Wolfrum: Laserdiagnostic and numerical studies of strongly swirling natural-gas flames, Proc. Combust. Inst. **27**, 1023–1030 (1998)

7.79 C. Schulz, V. Sick, J. Wolfrum, V. Drewes, M. Zahn, R. Maly: Quantitative 2D single-shot imaging of NO concentrations and temperatures in a transparent SI engine, Proc. Combust. Inst. **26**, 2597–2604 (1996)

7.80 J. Warnatz, U. Maas, R.W. Dibble: *Combustion*, 3rd edn. (Springer, Berlin, Heidelberg 2001)

7.81 V. Bergmann, W. Meier, D. Wolff, W. Stricker: Application of spontaneous Raman and Rayleigh scattering and 2D LIF for the characterization of a turbulent $CH_4/H_2/N_2$ jet diffusion flame, Appl. Phys. B **66**, 489–502 (1998)

7.82 D. Geyer, A. Kempf, A. Dreizler, J. Janicka: Scalar dissipation rates in isothermal and reactive turbulent opposed-jets: 1D-Raman/Rayleigh experiments supported by LES, Proc. Combust. Inst. **30**, 681–689 (2005)

7.83 H.W. Schrötter: Linear Raman spectroscopy: A state of the art report. In: *Nonlinear Raman Spectroscopy and Its Chemical Applications*, NATO Adv. Study Inst. Ser. C, Vol. 93, ed. by W.J. Kiefer, D.A. Long (Kluwer, Dordrecht 1982)

7.84 J. Zetterberg, Z.S. Li, M. Afzelius, M. Aldén: Two-dimensional temperature measurements in flames using filtered Rayleigh scattering at 254 nm. In: *European Combustion Meeting* (The Combustion Institute, Orléans 2003)

7.85 W. Meier, R.S. Barlow, Y.-L. Chen, J.-Y. Chen: Raman/Rayleigh/LIF measurements in a turbulent $CH_4/H_2/N_2$ jet diffusion flame: experimental techniques and turbulence–chemistry interaction, Combust. Flame **123**, 326–343 (2000)

7.86 A.C. Eckbreth: *Laser Diagnostics for Combustion Temperature and Species*, 2nd edn. (Gordon Breach, Amsterdam 1996)

7.87 S.B. Pope: *Turbulent Flows* (Cambridge Univ. Press, Cambridge 2000) p. 771

7.88 C. Schneider, A. Dreizler, J. Janicka: Fluid dynamical analysis of atmospheric reacting and isothermal swirling flows, Flow Turbulence Combust. **74**, 103–127 (2005)

7.89 W. Meier, S. Prucker, M.H. Cao, W. Stricker: Characterization of turbulent H_2/N_2/air jet diffusion flames by single-pulse spontaneous Raman scattering, Combust. Sci. Technol. **118**, 293–312 (1996)

7.90 R.W. Pitz, J.A. Wehrmeyer, J.M. Bowling, T.S. Cheng: Single pulse vibrational Raman scattering by a broadband KrF excimer laser in a hydrogen-air flame, Appl. Opt. **29**, 2325–2332 (1990)

7.91 A. Brockhinke, P. Andresen, K. Kohse-Höinghaus: Quantitative one-dimensional single-pulse multispecies concentration and temperature measurements in the lift-off region of a turbulent H_2-air diffusion flame, Appl. Phys. B **61**, 533–545 (1995)

7.92 W. Meier, O. Keck: Laser Raman scattering in fuel-rich flames: background levels at different excitation wavelengths, Meas. Sci. Technol. **13**, 741–749 (2002)

7.93 G. Herzberg: *Molecular Spectra and Molecular Structure*, Spectra of Diatomic Molecules, Vol. 1 (Krieger, Malabar 1989)

7.94 G. Herzberg: *Molecular Spectra and Molecular Structure*, Electronic Spectra and Electronic Structure of Polyatomic Molecules, Vol. 3, 2nd edn. (Krieger, Malabar 1991)

7.95 M.M. Tacke, D. Geyer, E.P. Hassel, J. Janicka: A detailed investigation of the stabilization point of lifted turbulent diffision flames, Proc. Combust. Inst. **27**, 1157–1165 (1998)

7.96 R.S. Barlow, P.C. Miles: A shutter-based line-imaging sytem for single-shot Raman scattering measurements of gradients in mixture fraction, Proc. Combust. Inst. **28**, 269–277 (2000)

7.97 H. Tennekes, J. Lumley: *A First Course in Turbulence* (MIT Press, Cambridge 1972)

7.98 V. Ebert, J. Wolfrum: Absorption spectroscopy. In: *Optical Measurements-Techniques and Applications*, ed. by F. Mayinger (Springer, Berlin, Heidelberg 1994) pp. 273–312

7.99 D.S. Baer, R.K. Hanson, M.E. Newfield, N.K.J.M. Gopaul: Multiplexed diode-laser sensor system for simultaneous H_2O, O_2, and temperature measurements, Opt. Lett. **19**, 1900–1902 (1994)

7.100 M.G. Allen: Diode laser absorption sensors for gas dynamic and combustion flows, Meas. Sci. Technol. **9**, 545–562 (1998)

7.101 A.P. Thorne: *Spectrophysics* (Chapman Hall, London 1988)

7.102 E.R. Furlong, D.S. Baer, R.K. Hanson: Combustion Control and Monitoring using a Multiplexed Diode-Laser Sensor System, Proc. Combust. Inst. **26**, 2851–2858 (1996)

7.103 A. Thorne, U. Litzén, S. Johannson: *Spectrophysics* (Springer, Berlin, Heidelberg 1999)

7.104 I.I. Sobel'man, L.A. Vainshtein, E.A. Yukov: *Excitation of Atoms and Broadening of Spectral Lines* (Springer, Berlin, Heidelberg 1995)

7.105 V. Ebert, T. Fernholz, C. Giesemann, H. Pitz, H. Teichert, J. Wolfrum, H. Jaritz: Simultaneous diode-laser-based in-situ detection of multiple species and temperature in a gas-fired power plant, Proc. Combust. Inst. **28**, 423–430 (2000)

7.106 S. Schäfer, M. Mashni, J. Sneider, A. Miklos, P. Hess, V. Ebert, K.-U. Pleban, H. Pitz: Sensitive detection of methane with a 1.65 µm diode laser by photoacoustic and absorption spectroscopy, Appl. Phys. B **66**, 511–516 (1998)

7.107 C.A. Taatjes, D.B. Oh: Time-resolved wavelength modulation spectroscopy measurements of HO_2 kinetics, Appl. Opt. **36**, 5817–5821 (1997)

7.108 K. Kohse-Höinghaus, D.F. Davidson, A.Y. Chang, R.K. Hanson: Quantitative NH_2 concentration determination in shock-tube laser-absorption experiments, J. Quant. Spectrosc. Radiat. Transfer **42**, 1–17 (1989)

7.109 J.J. Scherer, J.B. Paul, A. O'Keefe, R.J. Saykally: Cavity ringdown laser absorption spectroscopy: History, development, and application to pulsed molecular beams, Chem. Rev. **97**, 25 (1997)

7.110 S. Cheskis, I. Derzy, V.A. Lozovsky, A. Kachanov, D. Romanini: Cavity ring-down spectroscopy of OH radicals in low pressure flames, Appl. Phys. B **66**, 377–381 (1998)

7.111 S. Cheskis, I. Derzy, V.A. Lozovsky, A. Kachanov, F. Stoeckel: Intracavity laser absorption spectroscopy detection of CH_2 radicals in hydrocarbon flames, Chem. Phys. Lett. **277**, 423 (1997)

7.112 P. Zalicki, Y. Ma, R.N. Zare, J.R. Dadamio, E.H. Wahl, T.G. Owano, C.H. Kruger: Methyl radical measurement by cavity ring-down spectroscopy, Chem. Phys. Lett. **234**, 269–274 (1995)

7.113 J.J. Scherer, D.J. Rakestraw: Cavity ring-down laser absorption spectroscopy detection of formyl (HCO) radical in a low pressure flame, J. Chem. Phys. **265**, 169–176 (1997)

7.114 J.J. Scherer, K.W. Aniolek, N.P. Cernansky, D.J. Rakestraw: Determination of methyl radical concentrations in a methane/air flame by infrared cavity ringdown laser absorption spectroscopy, J. Chem. Phys. **107**, 6196–6203 (1997)

7.115 Y. He, M. Hippler, M. Quack: High-resolution cavity rind-down absorption spectroscopy of nitrous oxide and chloroform using near-infrared cw diode laser, Chem. Phys. Lett. **289**, 527–534 (1998)

7.116 T. Yu, M.C. Lin: Kinetics of the C_6H_5 + NO association reaction, J. Phys. Chem. **98**, 2105–2109 (1994)

7.117 S.T. Sanders, J. Wang, J.B. Jeffries, R.K. Hanson: Diode-laser absorption sensor for line-of-sight gas

temperature distributions, Appl. Opt. **40**, 4404–4415 (2001)
7.118 D.W. Mattison, S.T. Sanders, L. Ma, K.M. Hinckley, J.B. Jeffries, R.K. Hanson, C.M. Brophy: Pulse detonation engine characterization and control using tunable diode-laser sensors, J. Propulsion Power **19**, 568–572 (2003)
7.119 X. Zhou, J.B. Jeffries, R.K. Hanson: Development of a fast temperature sensor for combustion gases using a single tunable diode laser, Appl. Phys. B **81**, 711–722 (2005)
7.120 J.T.C. Liu, G.B. Rieker, J.B. Jeffries, R.K. Hanson, M.R. Gruber, C.D. Carter, T. Mathur: Near infrared diode laser absorption diagnostic for temperature and water vapor in a scramjet combustor, Appl. Opt. **44**, 6701–6711 (2005)
7.121 V. Nagali, R.K. Hanson: Design of a diode-laser sensor to monitor water vapor in high-pressure combustion gases, Appl. Opt. **36**, 9518–9527 (1997)
7.122 S.T. Sanders, J.A. Baldwin, T.P. Jenkins, D.S. Baer, R.K. Hanson: Diode-laser sensor for monitoring multiple combustion parameters in pulse detonation engines, Proc. Combust. Inst. **28**, 587–594 (2000)
7.123 H. Teichert, T. Fernholz, V. Ebert: Simultaneous in-situ measurements of CO, H_2O and gas temperatures in a full-sized coal-fired power plant by near-infrared diode lasers, Appl. Opt. **42**, 2043–2051 (2003)
7.124 L.S. Rothman, D. Jacquemart, A. Barbe, D.C. Benner, M. Birk, L.R. Brown, K. Carleer, C. Chackerian Jr., Chance, L.H. Coudert, V. Dana, V.M. Devi, J.-M. Flaut, R.R. Gamache, A. Goldmann, J.-M. Hartmann, K.W. Jucks, A.G. Maki, S.T. Mandin, S.T. Massie, J. Orphal, A. Perrin, C.P. Rinsland, M.A.H. Smith, J. Tennyson, R.N. Tolchenov, R.A. Toth, J. Vander Auwera, P. Varanasi, G. Wagner: The HITRAN 2004 molecular spectroscopic database, J. Quant. Spectrosc. Radiat. Transfer **96**, 139–204 (2004), (http://cfa-www.harvard.edu/HITRAN/)
7.125 G.B. Rieker, J.T.C. Liu, J.B. Jeffries, R.K. Hanson, T. Mathur, M.R. Gruber, C.D. Carter: Diode laser sensor for gas temperature and H_2O concentration in a scramjet combustor using wavelength modulation spectroscopy, AIAA Paper **2005-3710** (2005)
7.126 J.T.C. Liu, J.B. Jeffries, R.K. Hanson: Wavelength modulation absorption spectroscopy with 2f detection using multiplexed diode lasers for rapid temperature measurements in gaseous flows, Appl. Phys. B **78**, 503–511 (2004)
7.127 K. Kohse-Höinghaus: Laser techniques for the quantitative detection of reactive intermediates in combustion systems, Prog. Energy Combust. Sci. **20**, 203–279 (1994)
7.128 J.W. Daily: Laser induced fluorescence spectroscopy in flames, Prog. Energy Combust. Sci. **23**, 133–199 (1997)
7.129 E.W. Rothe, Y. Gu, A. Chryssostomou, P. Andresen, F. Bormann: Effect of laser intensity and of lower-state rotational energy transfer upon temperature measurements made with laser-induced predissociative fluorescence, Appl. Phys. B **66**, 251 (1998)
7.130 J. Luque, D.R. Crosley: *LIFBASE: Database and spectral simulation for diatomic molecules* (SRI International, Menlo Park 1999), MP-99-0099, (www.sri.com/cem/lifbase)
7.131 W.G. Bessler, C. Schulz, V. Sick, J.W. Daily: www.lifsim.com). In: *3rd Joint meeting of the US sections of The Combustion Institute* (Combustion Institute, Chicago 2003) pp. 1–6, Paper PI05
7.132 R. Kienle, M.P. Lee, K. Kohse-Höinghaus: A scaling formalism for the representation of rotational energy transfer in OH A in combustion experiments, Appl. Phys. B **63**, 403–418 (1996)
7.133 P.H. Paul, J.A. Gray, J.L.D. Jr., J.W.T. Jr.: A model for temperature-dependent collisional quenching of NO $A^2\Sigma^+$, Appl. Phys. B **57**, 249–259 (1993)
7.134 W.G. Bessler, M. Hofmann, F. Zimmermann, G. Suck, J. Jakobs, S. Nicklitzsch, T. Lee, J. Wolfrum, C. Schulz: Quantitative in-cylinder NO-LIF imaging in a realistic gasoline engine with spray-guided direct injection, Proc. Combust. Inst. **30**, 2667–2674 (2005)
7.135 J.W. Daily, T.B. Settersten, W.G. Bessler, C. Schulz, V. Sick: A computer code to simulate laser excitation and collision dynamics in nitric oxide. In: *4th Joint Meeting of the U.S. Sections of the Combustion Institute* (The Combustion Institute, Philadelphia 2005)
7.136 R. Cattolica: OH rotational temperature from two-line laser-excited fluorescence, Appl. Opt. **20**, 1156–1166 (1981)
7.137 K.P. Gross, R.L. McKenzie: Singe-pulse gas thermometry at low temperatures using two-photon laser-induced fluorescence in NO-N_2 mixtures, Opt. Lett. **8**, 368–370 (1983)
7.138 M.P. Lee, B.K. McMillin, R.K. Hanson: Temperature measurements in gases by use of planar laser-induced fluorescence imaging of NO, Appl. Opt. **32**, 5379–5396 (1993)
7.139 J.M. Seitzman, R.K. Hanson: Two-line planar fluorescence for temporally resolved temperature imaging in a reacting supersonic flow over a body, Appl. Phys. B **57**, 385–391 (1993)
7.140 A. Roller, A. Arnold, M. Decker, V. Sick, J. Wolfrum, W. Hentschel, K.-P. Schindler: Non-intrusive temperature measurements during the compression phase of a DI Diesel engine, SAE Tech. Paper Ser. **952461** (1995)
7.141 M. Tamura, P.A. Berg, J.E. Harrington, J. Luque, J.B. Jeffries, G.P. Smith, D.R. Crosley: Collisional quenching of CH (A), OH A, and NO (A) in low-pressure hydrocarbon flames, Combust. Flame **114**, 502–514 (1998)
7.142 M. Tamura, J. Luque, J.E. Harrington, P.A. Berg, G.P. Smith, J.B. Jeffries, D.R. Crosley: Laser-induced fluorescence of seeded nitric oxide as a flame thermometer, Appl. Phys. B **66**, 503–510 (1998)

7.143 M. Tsujishita, A. Hirano, M. Yokoo, T. Sakuraya, Y. Takeshita: Accurate thermometry using NO and OH laser-induced fluorescence in an atmospheric pressure flame, JSME Int. J. Ser. B **42**, 119 (1999)

7.144 W.G. Bessler, F. Hildenbrand, C. Schulz: Two-line laser-induced fluorescence imaging of vibrational temperatures of seeded NO, Appl. Opt. **40**, 748–756 (2001)

7.145 J.B. Bell, M.S. Day, J.F. Grcar, W.G. Bessler, C. Schulz, P. Glarborg, A.D. Jensen: Detailed modeling and laser-induced fluorescence imaging of nitric oxide in a NH_3-seeded non-premixed methane/air flame, Proc. Combust. Inst. **29**, 2195–2202 (2002)

7.146 J.W. Daily, E.W. Rothe: Effect of laser intensity and lower-state rotational energy transfer upon temperature measurements made with laser-induced fluorescence, Appl. Phys. B **68**, 131–140 (1999)

7.147 W.G. Bessler, C. Schulz: Quantitative multi-line NO-LIF temperature imaging, Appl. Phys. B **78**, 519–533 (2004)

7.148 J.E. Dec, J.O. Keller: High speed thermometry using two-line atomic fluorescence, Proc. Combust. Inst. **21**, 1737–1745 (1986)

7.149 C.F. Kaminski, J. Engström, M. Aldén: Quasi-instantaneous two-dimensional temperature measurements in a spark ignition engine using 2-line atomic fluorescence, Proc. Combust. Inst. **27**, 85–93 (1998)

7.150 J. Engström, J. Nygren, M. Aldén, C.F. Kaminski: Two-line atomic fluorescence as a temperature probe for highly sooting flames, Opt. Lett. **25**, 1469–1471 (2000)

7.151 P. Andresen, A. Bath, W. Groger, H.W. Lulf, G. Meijer, J.J. ter Meulen: Laser-induced fluorescence with tunable excimer lasers as a possible method for instantaneous temperature field measurements at high pressures: checks with an atmospheric flame, Appl. Opt. **27**, 365–378 (1988)

7.152 A. Arnold, B. Lange, T. Bouché, Z. Heitzmann, G. Schiff, W. Ketterle, P. Monkhouse, J. Wolfrum: Absolute temperature fields in flames by 2D-LIF of OH using excimer lasers and CARS spectroscopy, Ber. Bunsenges. Phys. Chem. **96**, 1388–1392 (1992)

7.153 B.K. McMillin, J.M. Seitzman, R.K. Hanson: Comparison of NO and OH planar fluorescence temperature measurements in scramjet model flowfields, AIAA J. **32**, 1945–1952 (1994)

7.154 B. Atakan, J. Heinze, U.E. Meier: OH laser-induced fluorescence at high pressures: spectroscopic and two-dimensional measurements exciting the A-X (1,0) transition, Appl. Phys. B **64**, 585–591 (1997)

7.155 A.T. Hartlieb, B. Atakan, K. Kohse-Höinghaus: Temperature measurement in fuel-rich non-sooting low-pressure hydrocarbon flames, Appl. Phys. B **70**, 435–445 (2000)

7.156 R.L. McKenzie, K.P. Gross: Two-photon excitation of nitric oxide fluorescence as a temperature indicator in unsteady gasdynamic processes, Appl. Opt. **20**, 2153–2165 (1981)

7.157 J.M. Seitzman, G. Kychakoff, R.K. Hanson: Instantaneous temperature field measurements using planar laser-induced fluorescence, Opt. Lett. **10**, 439–441 (1985)

7.158 K.P. Gross, R.L. McKenzie: Measurements of fluctuating temperatures in a supersonic turbulent flow using laser-induced fluorescence, AIAA J. **23**, 1932–1936 (1985)

7.159 K.P. Gross, R.L. McKenzie, P. Logan: Measurement of temperature, density, pressure, and their fluctuations in supersonic turbulence using laser-induced fluorescence, Exp. Fluids **5**, 372–380 (1987)

7.160 B.K. McMillin, J.L. Palmer, R.K. Hanson: Temporally resolved, two-line fluorescence imaging of NO temperature in a transverse jet in a supersonic cross flow, Appl. Opt. **32**, 7532–7545 (1993)

7.161 A.O. Vyrodov, J. Heinze, M. Dillmann, U.E. Meier, A.W. Stricker: Laser-induced fluorescence thermometry and concentration measurements on NO A-X (0,0) transitions in the exhaust gas of high pressure CH_4/air flames, Appl. Phys. B **61**, 409–414 (1995)

7.162 M. Yorozu, Y. Okada, A. Endo: Two dimensional rotational temperature measurement by multiline laser induced fluorescence of nitric oxide in combustion flame, Opt. Rev. **3**, 293–298 (1996)

7.163 E.A. Brinkman, G.A. Raiche, M.S. Brown, J.B. Jeffries: Optical diagnostics for temperature measurement in a dc arcjet reactor used for diamond deposition, Appl. Phys. B. **64**, 689 (1997)

7.164 P.C. Palma, T.J. McIntyre, A.F.P. Houwing: PLIF thermometry in shock tunnel flows using a Raman-shifted tunable excimer laser, Shock Waves **8**, 275–284 (1998)

7.165 W.M. Ruyten, M.S. Smith, L.L. Price, W.D. Williams: Three-line fluorescence thermometry of optically thick shock-tunnel flow, Appl. Opt. **37**, 2334–2339 (1998)

7.166 G. Dilecce, M. Simek, M. Vigliotti, S. De Benedictis: Fast LIF approach to NO rotational temperature and density measurement: Application to a gas-dynamic expansion, Appl. Spectrosc. **54**, 824–831 (2000)

7.167 H. Kronemayer, W. Bessler, C. Schulz: Gas-phase temperature measurements in evaporating sprays and spray flames based on NO multiline LIF, Appl. Phys. B **81**, 1071–1074 (2005)

7.168 W.G. Bessler, C. Schulz, T. Lee, D.I. Shin, M. Hofmann, J.B. Jeffries, J. Wolfrum, R.K. Hanson: Quantitative NO-LIF imaging in high-pressure flames. In: *Optical and Laser Diagnostics*, ed. by C. Arcoumanis, K.T.V. Grattan (Institute of Physics, Bristol, Philadelphia 2003) pp. 107–114

7.169 M.P. Lee, P.H. Paul, R.K. Hanson: Quantitative imaging of temperature fields in air using planar laser-induced fluorescence of O_2, Opt. Lett. **12**, 75–77 (1987)

7.170 G. Laufer, R.L. McKenzie, D.G. Fletcher: Method for measuring temperatures and densities in hyper-

sonic wind tunnel air flows using laser-induced O_2 fluorescence, Appl. Opt. **29**, 4873–4883 (1990)
7.171 M.S. Smith, L.L. Price, W.D. Williams: Laser-induced fluorescence diagnostics using a two-line excitation method, AIAA J. **31**, 478–482 (1993)
7.172 T. Ni-Imi, T. Fujimoto, N. Shimizu: Method for planar measurement of temperature in compressible flow using two-line laser-induced iodine fluorescence, Opt. Lett. **15**, 918–920 (1990)
7.173 A. Kido, S. Kubota, H. Ogawa, N. Miyamoto: Simultaneous measurements of concentration and temperature distributions in unsteady gas jets by an iodine LIF method, SAE Tech. Paper Ser. **980146** (1998)
7.174 F. Großmann, P.B. Monkhouse, M. Ridder, V. Sick, J. Wolfrum: Temperature and pressure dependences of the laser-induced fluorescence of gas-phase acetone and 3-pentanone, Appl. Phys. B **62**, 249–253 (1996)
7.175 M.C. Thurber, F. Grisch, R.K. Hanson: Temperature imaging with single- and dual-wavelength acetone planar laser-induced fluorescence, Opt. Lett. **22**, 251–253 (1997)
7.176 S. Einecke, C. Schulz, V. Sick, A. Dreizler, R. Schießl, U. Maas: Two-dimensional temperature measurements in an SI engine using two-line tracer LIF, SAE Tech. Paper Ser. **982468** (1998)
7.177 M. Luong, W. Koban, C. Schulz: Novel strategies for imaging temperature distribution using Toluene LIF, J. Phys. **45**, 133–139 (2005)
7.178 W. Koban, J.D. Koch, V. Sick, N. Wermuth, R.K. Hanson, C. Schulz: Predicting LIF signal strength for toluene and 3-pentanone under engine-related temperature and pressure conditions, Proc. Combust. Inst. **30**, 1545–1553 (2005)
7.179 W. Koban, C. Schulz: Toluene as a tracer for fuel, temperature and oxygen concentrations, SAE Tech. Paper Ser. **2005-01-2091** (2005)
7.180 W. Koban, J.D. Koch, R.K. Hanson, C. Schulz: Toluene LIF at elevated temperatures: Implications for fuel/air ratio measurements, Appl. Phys. B **80**, 147–150 (2005)
7.181 H. Zacharias, J.B. Halpern, K.H. Welge: Two-photon excitation of NO ($A^2\Sigma^+$; $v' = 0,1,2$) and radiation lifetime and quenching measurements, Chem. Phys. Lett. **43**, 41–44 (1976)
7.182 G.F. Nutt, S.C. Haydon, A.J. McIntosh: Measurement of electronic quenching rates in nitric oxide using two-photon spectroscopy, Chem. Phys. Lett. **62**, 402–404 (1979)
7.183 I.S. McDermid, J.B. Laudenslager: Radiative lifetimes and electronic quenching rate constants for single-photon-excited rotational levels of NO ($A^2\Sigma^+$, $v' = 0$), J. Quant. Spectrosc. Radiat. Transfer **27**, 483–492 (1982)
7.184 N. Sullivan, A. Jensen, P. Glarborg, M.S. Day, J.F. Grcar, J.B. Bell, C. Pope, R.J. Kee: Ammonia conversion and NO_x formation in laminar coflowing non-premixed methane/air flames, Combust. Flame **131**, 285–298 (2002)
7.185 W.G. Bessler, C. Schulz, T. Lee, D.I. Shin, M. Hofmann, J.B. Jeffries, J. Wolfrum, R.K. Hanson: Quantitative NO-LIF imaging in high-pressure flames, Appl. Phys. B **75**, 97–102 (2002)
7.186 C. Schulz, V. Sick: Tracer-LIF diagnostics: Quantitative measurement of fuel concentration, temperature and air/fuel ratio in practical combustion situations, Prog. Energy Combust Sci. **31**, 75–121 (2005)
7.187 F. Großmann, P.B. Monkhouse, M. Ridder, V. Sick, J. Wolfrum: Temperature and pressure dependencies of the laser-induced fluorescence of gas-phase acetone and 3-pentanone, Appl. Phys. B **62**, 249–253 (1996)
7.188 S. Einecke, C. Schulz, V. Sick: Measurement of temperature, fuel concentration and equivalence ratio fields using tracer LIF in IC engine combustion, Appl. Phys. B **71**, 717–723 (2000)
7.189 J.D. Koch, R.K. Hanson: Temperature and excitation wavelength dependencies of 3-pentanone absorption and fluorescence for PLIF applications, Appl. Phys. B **76**, 319–324 (2003)
7.190 W. Koban, J.D. Koch, R.K. Hanson, C. Schulz: Absorption and fluorescence of toluene vapor at elevated temperatures, Phys. Chem. Chem. Phys. **6**, 2940–2945 (2004)
7.191 M.C. Thurber, B.J. Kirby, R.K. Hanson: Instantaneous imaging of temperature and mixture fraction with dual-wavelength acetone PLIF, AIAA Paper **98-0397** (1998)
7.192 N.P. Tait, D.A. Greenhalgh: PLIF imaging of fuel fraction in practical devices and LII imaging of soot, Ber. Bunsenges. Phys. Chem. **97**, 1619 (1993)
7.193 A.C. Eckbreth: CARS thermometry in practical combustors, Combust. Flame **39**, 133–147 (1980)
7.194 R.J. Hall: Intensity convolutions of CARS spectra, Opt. Commun. **52**, 360–366 (1985)
7.195 R.E. Teets: Accurate convolutions of coherent anti-Stokes Raman spectra, Opt. Lett. **9**, 226–228 (1984)
7.196 M. Péalat, M. Lefebvre, J.-P.E. Taran, P.L. Kelley: Sensitivity of quantitative vibrational coherent anti-Stokes Raman spectroscopy to saturation and stark shifts, Phys. Rev. **38**, 1948–1965 (1988)
7.197 M.L. Koszykowski, R.L. Farrow, R.E. Palmer: Calculation of collisionally narrowed coherent anti-Stokes Raman spectroscopy spectra, Opt. Lett. **10**, 478–480 (1985)
7.198 S. Kröll, M. Aldén, T. Berglind, R.J. Hall: Noise characteristics of single shot broadband Raman-resonant CARS with single- and multimode lasers, Appl. Opt. **26**, 1068–1073 (1987)
7.199 P.R. Regnier, J.P. Taran: On the possibility of measuring gas concentrations by stimulated anti-Stokes scattering, Appl. Phys. Lett. **23**, 240–242 (1973)
7.200 W.A. England, J.M. Milne, S.N. Jenny, D.A. Greenhalgh: Application of CARS to an operating chemical reactor, Appl. Spectrosc. **38**, 867–876 (1984)

7.201 A.C. Eckbreth, R.J. Hall: CARS concentration sensitivity with and without nonresonant background suppression, Combust. Sci. Technol. **25**, 175–192 (1981)

7.202 M. Schenk, T. Seeger, A. Leipertz: Time-resolved CO_2 thermometry for pressures as great as 5 MPa by use of pure rotational coherent anti-Stokes Raman scattering, Appl. Opt. **44**, 6526–6536 (2005)

7.203 P.-E. Bengtsson, L. Martinsson, M. Aldén: Dual-broadband rotational CARS measurements in an IC engine, Proc. Combust. Inst. **25**, 1735–1742 (1994)

7.204 P.-E. Bengtsson, M. Aldén: Soot-visualization strategies using laser techniques, Appl. Phys. B **60**, 51–59 (1995)

7.205 P.R.N. Childs, J.R. Greenwood, C.A. Long: Review of temperature measurement, Rev. Sci. Instrum. **71**(8), 2959–2978 (2000)

7.206 P. Neubert: Device for indicating the temperature distribution of hot bodies, US Patent No. 2071471 (1937)

7.207 F. Urbach, N.R. Nail, D. Pearlman: The observation of temperature distributions and of thermal radiation by means of non-linear phosphors, J. Opt. Soc. Am. **39**(12), 1011–1019 (1949)

7.208 L.C. Bradley: A temperature-sensitive phosphor used to measure surface temperatures in aerodynamics, Rev. Sci. Instrum. **24**(3), 219–220 (1953)

7.209 G.M. Buck: Surface temperature/heat transfer measurement using a quantitative phosphor thermography system. In: *29th Aerospace Sciences Meeting AIAA Paper 91-0064* (1991)

7.210 J.H. Monaweck, W.J. McGonnagle: Thermal testing of reactor fuel elements. In: *Proc. Symp. Nondestructive Test Field Nuclear Energy*, ed. by D.R. Green (ASTM, West Conshohocken 1957), ASTM Special Tech. Publ. 352–357

7.211 S.W. Allison, M.R. Cates, D.L. Beshears: A survey of thermally sensitive phosphors for pressure sensitive paint applications, Proc. ISA 46th Annual, ISA **397**, 29–37 (2000)

7.212 J.P. Feist, A.L. Heyes: The characterization of Y2O2S:Sm powder as a thermographic phosphor for high temperature applications, Meas. Sci. Technol. **11**, 942–947 (2000)

7.213 Y. Le Sant, J.L. Edy: Phosphor thermography technique in hypersonic wind tunnels: First results. In: *15th ICIASF* (1993)

7.214 S.W. Allison, G.T. Gillies: Remote thermometry with thermographic phosphors: Instrumentation and application, Rev. Sci. Instrum. **68**(7), 2615–2650 (1997)

7.215 T. Liu, B.T. Campbell, J.P. Sullivan: Thermal paints for shock/boundary layer interaction in inlet flows, AIAA Paper **92-3626** (1992)

7.216 B.T. Campbell, T. Liu, J.P. Sullivan: Temperature measurement using fluorescent molecules. In: *6th International Symposium on Application of Laser Technique* (1992)

7.217 B.T. Campbell, T. Liu, J.P. Sullivan: Temperature sensitive fluorescent paint systems, AIAA Paper **94-2483** (1994)

7.218 B.G. Mc. Lachlan, J.H. Bell, J. Gallery, M. Gouterman, J. Callis: Boundary layer transition detection by luminescent imaging, AIAA Paper **93-0177** (1993)

7.219 K. Asai, H. Kanda, T. Kunimasu, T. Liu, J.P. Sullivan: Detection of boundary-layer transition in a cryogenic wind tunnel by using luminescent paint, AIAA Paper **96-2185** (1996)

7.220 T.G. Popernack, L.R. Owens, M.P. Hamner, M.J. Morris: Application of temperature sensitive paint for detection of boundary layer transition, ICIASF Proc. (1997)

7.221 U. Fey, K. De Groot, Y. Le Sant: Thermography as a tool in wind tunnel testing, DLR Rep. **IB 224-2007A09** (2007)

7.222 J.P. Hubner, B.F. Carroll, K.S. Schanze: Heat transfer measurements in hypersonic flow using luminescent coating techniques, AIAA Paper **2002-0741** (2002)

7.223 I. Le Sant: Private communication, ONERA (2006)

7.224 T. Liu, J.P. Sullivan: *Pressure and Temperature Sensitive Paint* (Springer, Berlin, Heidelberg 2005)

7.225 U. Fey, R.H. Engler, Y. Egami, y. Iijima, K. Asai, U. Jansen, J. Quest: ETW). In: *20th Int. Congress on Instrumentation in Aerospace Simulation Facilities, ICIASF 2003 Record* (2003) pp. 77–88

7.226 W. Banks, C.P. van Dam, H.J. Shiu, G.M. Miller: Visualization of in-flight flow phenomena using infrared thermography. In: *9th Int. Symposium on Flow Visualization* (2000) pp. 1–11, 24 (NASA TM-2000-209027)

7.227 J. Sullivan, J.W. Gregory, C.Y. Huang, H. Sakaue: Flow visualization applications of luminescent paints. In: *10th Int. Symposium on Flow Visualization* (2002)

7.228 Y. Egami, U. Fey, C. Klein, M. Sitzmann, J. Wild: Transition detection on high-lift devices in DNW-KKK by means of temperature-sensitive paint. In: *12th Int. Symp. on Flow Visual.* (2006)

7.229 K. De Groot: Private communication, DLR (2006)

7.230 E. Reshotko: *Laminar Flow Control, Special course on stability and transition of laminar flows*, AGARD Rep., Vol. 709 (VKI, Brussels 1984)

7.231 W.S. Saric, H.L. Reed: Toward practical laminar flow control – Remaining challenges. In: *34th AIAA Fluid Dynamics Conference* (2004)

7.232 U. Fey, Y. Egami, C. Klein: Using cryoTSP as a tool for transition detection and instability examination at high Reynolds numbers. In: *Notes on Numerical Fluid Mechanics and Multidisciplinary Design*, Vol. 96, ed. by C. Tropea, S. Jarkirlic, H.-J. Heinemann, R. Henke, H. Hönlinger (Springer, Berlin, Heidelberg 2007)

7.233 Y. Iijima, Y. Egami, A. Nishizawa, K. Asai, U. Fey, R.H. Engler: Optimization of temperature-sensitive paint formulation for large-scale cryogenic wind tunnels. In: *20th Int. Congress on Instrumentation in*

Aerospace Simulation Facilities (ICIASF), ICIASF 2003 Record (2003) pp. 70–77

7.234 U. Fey, Y. Egami, R.H. Engler: High Reynolds number transition detection by means of temperature sensitive paint. In: *44th AIAA Aerospace Sciences Meeting and Exhibit AIAA Paper 2006-514* (2006)

7.235 U. Fey, Y. Egami, R.H. Engler: Using cryoTSP as a tool for transition detection. In: *Int. Council of the Aeronautical Sciences* (2006)

7.236 Y. Egami, U. Fey, J. Quest: Development of new two-component TSP for cryogenic testing. In: *45th Aerospace Sciences Meeting and Exhibit* (2007)